LA-3831-MS

C. 3

LOS ALAMOS SCIENTIFIC LABORATORY
of the
University of California

LOS ALAMOS • NEW MEXICO

Status Report of the LASL Controlled Thermonuclear Research Program for 12-Month Period Ending October 31, 1967

UNITED STATES
ATOMIC ENERGY COMMISSION
CONTRACT W-7405-ENG. 36

This LA...MS report presents the status of the LASL Controlled Thermonuclear Research Program. The previous annual status report in this series, unclassified, is:

LA-3628-MS

This report, like other special-purpose documents in the LA...MS series, has not been reviewed or verified for accuracy in the interest of prompt distribution.

Printed in the United States of America. Available from
Clearinghouse for Federal Scientific and Technical Information
National Bureau of Standards, U. S. Department of Commerce
Springfield, Virginia 22151
Price: Printed Copy $3.00; Microfiche $0.65

LA-3831-MS
UC-20, CONTROLLED
THERMONUCLEAR PROCESSES
TID-4500

LOS ALAMOS SCIENTIFIC LABORATORY
of the
University of California
LOS ALAMOS • NEW MEXICO

Report compiled: November 1967
Report distributed: December 19, 1967

Status Report of the LASL Controlled Thermonuclear Research Program for 12-Month Period Ending October 31, 1967

INTRODUCTION

(J. L. Tuck)

The Presidential Supplementary Budget (Fiscal Year 1968) designated the Scyllac project for support. The Joint Committee on Atomic Energy has since approved it for construction.

Scyllac support experiments (stabilization) in progress, using Scylla IV, are reported below and are encouraging.

Application of advanced computer techniques to plasma physics seem to be very successful.

One of the major difficulties in controlled thermonuclear research has always been the limited validity of mathematical theory. Real systems are too complicated for accurate representation so that theory has had to occupy itself with very simple systems and, especially, vanishingly low β. This is almost certainly the reason why so much of the specifically Sherwood experimental research in the U.S. and elsewhere has been concerned with very low-density, low-β systems, far removed from the conditions that would be required if thermonuclear power were the dominant consideration.

Since the Los Alamos policy has, for many years, been to study high densities and high temperature, with theory if possible, and without it if necessary, high-β mathematical theory has been a special subject of study. The last two years have seen some progress.

The important new factor, however, is the combination of theory and the computer. It seems certain that these techniques will provide results, by means of this new kind of "experimental theory," for regions of density and for systems of complexity that would virtually never be reached by closed mathematical theory. Such computer plasma simulation is not exact either; the computer is still not large enough to handle plasmas exactly, even with poor statistics. So various approximations have to be made, e.g., electrons smeared out, etc. But these approximations may be more valid than those of mathematical theory and moreover they are subject to experimental (i.e., computer) test.

This annual report contains a computer simulation of a θ-pinch which exhibits a *loss cone* instability and rapidly relaxes to a stable isotropic configuration (p. 95). Already this bids fair to solve a longstanding θ-pinch puzzle, namely, that the plasma is able to stream axially out with full thermal speed a short time after the radial compression which added energy only to the radial velocity, and before enough collisions could have occurred to turn the particles from radial to axial motion.

In another case, not given in detail here but to be published, the Particle In Cell (P.I.C.) method, which has been so successful in two-dimensional hydrodynamics, has been applied to the hydromagnetic case of the sheath moving down a plasma gun and contracting off the end. The agreements between the computation and the sheath pictures is strikingly close (p. 94).

REDUCTION OF PLASMA LOSS FROM OPEN-ENDED MAGNETIC CONFINEMENT SYSTEMS BY MAGNETICALLY ROUGH WALLS

(J. L. Tuck)

Introduction

So far as radial confinement is concerned, the performance of uniform axial magnetic fields in cylindrical geometry has been exemplary for high-β, hot ($\sim$ 5 keV), dense ($\sim 5 \times 10^{16}$ ion cm^{-3}) plasma, up to the rather brief ($\sim$ 5 μsec) confinement time determined by the free-streaming plasma loss from the ends. Plasma such as this is not too remote in terms of density and temperature from that which might be used in a power producing thermonuclear reaction. The currently observed gross thermonuclear power of the Scylla IV plasma is 600 W/liter which extrapolates for D-T to a useful 110 kW/liter. Such a plasma exerts a pressure of 400 atm and has a mean free path of $\sim$ 10 m and so it is not collision dominated.

There have been many proposals and attempts to mitigate the plasma loss from open-ended magnetic confinement systems. The first of these historically is, of course, the magnetic mirror. For modest mirror ratios it works well, but when large loss reduction (e.g., > 10) is required, the strength of the magnetic field becomes a difficulty. Attempts have been made to increase the efficiency of mirrors by a radial electric field to increase $v_{\perp}/v_{\parallel}$, e.g., ixion, homopolar. These have worked to some extent but they are associated with instabilities and wall impurities, and would, in any case, be entirely useless for the dense, high-β plasma which is of main concern. Radiation from cavities has also been tried; cavities exerting 400 atm pressure do not seem to be immediately at hand.

The radical way out is to close the ends on themselves, i.e., the Scyllac toroidal proposal, and abandon cylindrical symmetry. However, once the symmetry of straight magnetic field lines is relinquished, new kinds of problems arise; the plasma must not drift out of the torus and so an equilibrium condition must be satisfied. Conditions for hydromagnetic stability in bumpy magnetic fields must be met, e.g., $|\int d\ell/B|$ etc. Current stability theory in the main is an extrapolation from B = 0. When applied to such complicated boundaries, it usually predicts ballooning at some small β far below that envisaged and ceases to be valid thereafter. Fortunately at high β, hot plasmas behave far better experimentally than low-β theory would predict. Scylla IV stability, for example, is evidence of this.[1] Nevertheless it may be necessary to take a further measure to suppress instability--dynamic stabilization--if required. Dynamic stabilization at high β is even farther removed from theoretical understanding than static high-β stability. Once again, however, there is some surprisingly encouraging experimental evidence for dynamic stabilization at high β.[2]

Thus the Scyllac experiment is daring. If successful, it will bring a factor of 10 advance toward nτ, the energy break-even point (Lawson criterion), where gross thermonuclear energy output of the plasma equals energy put into the plasma as heat. The present Scylla IV plasma falls short of this by a factor of 500. So Scyllac should and apparently will be built.

Without prejudicing Scyllac, but in parallel, it would clearly be most rewarding if some way could be found of extending nτ without sacrificing the cylindrical symmetry of the straight θ-pinch. The loss per unit volume can be decreased by increasing the length, so that the confinement time increases proportionately with the length. Since the power supply and building is by far the main expense in a θ-pinch, once these exist, the expense of the construction of a long, straight θ-pinch is nominal. The Scylla Ad Hoc Committee recommended that such a 10-15 m straight θ-pinch be built as an intermediate step in the large Scyllac θ-pinch program.

Beyond a factor of 10 or so, the lengthening procedure becomes unwieldy. To reach the Lawson nτ, a θ-pinch length of 500-1000 m is required for end losses only, assuming that radial diffusion is zero. Starting with a 20-m θ-pinch, if the end loss could be reduced by a factor of 25, the nτ would rise to that of a 500-m long θ-pinch, as determined by end losses only; it would be 25 times better than a 500 m θ-pinch in terms of radial diffusion losses. Any saving in the losses from the

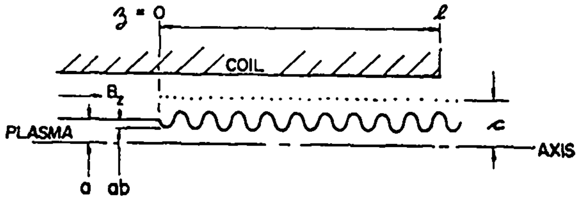

Fig. 1. Plasma in a magnetic field.

ends also goes to compensate for power expended in the stopping process.

In what follows, the objective is to achieve a loss reduction factor of at least 10.

Magnetically Rough Walls

The molecular pump of Gaede[3] easily maintains a density ratio of ~ 10^5 between directly communicating points in a tube containing gas with a long mean free path. It does this by moving the molecularly rough tube walls with near molecular thermal speed toward the high-density end. This prompted the question whether a magnetically rough wall, either fixed or moving, could control hot plasma escaping from the open end of a magnetic system such as a θ-pinch.

Consider a plasma confined (Fig. 1) in a B_z magnetic field from a solenoid extending indefinitely to the left of $z = 0$, and to a distance ℓ to the right. Coaxially inside this extension is a second solenoid system, radius c, which can impose a modulation on the main field B_z such that (1) for low β, the flux tube has the form radius = $a\,[1 - b \cos(2\pi/\lambda)(z + vt)]$ or (2) for high β, the sharp interface has the form radius = $a\,[1 + b \cos(2\pi/\lambda)(z + vt)]$. The perturbation produces bulges of radius $a(1 + b)$ and necks of radius $a(1 - b)$. There is a maximum slope (roughness factor) to the perburbation given by $dr/dz = 2\pi\, ab/\lambda$. The system contains ℓ/λ wavelengths. The concept presented here has its clearest expression for the plasma idealization of $\beta = 1$ and a sharp boundary. Every particle then experiences the full modulation, and takes a straight path to the next wall encounter. For $\beta < 1$, the system is a series of weak magnetic mirrors.

In the following, the effect of adiabatic invariance is considered: (1) Low β: For a particle at a bulge moving with inclination $v_\perp/v$ to the axis, the condition that it will be reflected at the next neck is $v_\perp/v > (1-b)/(1+b)$. For a set of particles released with random directions, the albedo is $[1 - (1-b)^2\ (1+b)^2]^{\frac{1}{2}}$. With invariance, those particles transmitted by the first mirror are also transmitted by the next and so on, until the particles are lost out of the far end. No buildup of stopping power by successive mirrors takes place in an adiabatic system. Giving the mirrors a velocity toward the source merely worsens the situation, by throwing more particles into the loss cone of the mirrors.

To obtain a cumulative effect, the adiabatic invariant must be broken down. To do this, the magnetic field must be changed rapidly, measured in gyro-rotation periods, i.e., maximize $bv_\parallel/\lambda B_z$, ($b \ll 1$). When the ratio gyro-radius/plasma radius is small, situations of some complexity can occur. Particles of appropriate v arrive at mirrors in resonance (or antiresonance) with their gyro-frequency, and classes of particles can be singled out for acceleration or expulsion from the system. In the static case, this becomes the familiar corrugated trap of Fedorchenko[4,5], and its elegant extension, the 'corkscrew' of Wingerson.[6,7] The resultant distribution function will be bumpy, thus promoting some classes of instability. Such instabilities need not be harmful; on the contrary, if they break down invariance they might greatly increase the z confinement. The confinement of low-β plasma in a trap consisting of multiple, fairly strong, mirrors has been computed by Post.[8] Here, collisions played the invariant-breaking role and, as expected, long series of mirrors showed increased confinement.

(2) High β Sharp Boundary: it has been shown--Morse bounce model[9] --that an analogous adiabatic invariant exists for this case also; it is the invariance of the action $\int P_r dr$ for the radial bouncing between slowly contracting walls. The condition for reflection at a neck, by particles starting out with $v_\perp/v$, is $v_\perp/v = \sin\theta > (1-b)/1 +b)$; the albedo of the neck for particles of random direction is $[1 - (1-b)^2/(1+b)^2]^{\frac{1}{2}}$.

(The condition for reflection in a $\beta = 1$ sharp boundary model (specular walls) is seen to be identical to that for a $\beta < 1$ magnetic mirror when the reflecting walls and the magnetic flux tubes in the two cases have the same ratio of contraction.) Once again, adiabaticity gives no cumulative effect, and a wall velocity toward the source reduces the albedo. To break down the adiabatic invariant, the contraction is made rapid, in this case measured in particle crossing times $2a/v_\perp$, and so $abv_\parallel/\lambda v_\perp$ is maximized.

Roughness $2\pi ab/\lambda$ is clearly a favorable factor in both high and low β cases.

Returning to a qualitative picture of the process in a nonadiabatic sharp boundary case, an isotropic Maxwell distribution of ions, most probable velocity $\overline{v}$, is placed at the entrance to Fig. 1. The average drift velocity of the entering distribution is $\overline{v}/4$. A fraction $(a/\ell)^2$ of these entering particles pass right through without touching the sides; this fraction can be made small and will be ignored. Particles incident on a roughness of angularity θ are deflected through an angle 2θ. These deflections can be equally retarding or accelerating to the progress of the particle in the z direction, depending on whether the angularity is θ or $\pi - \theta$, i.e., on whether the impact point is on the left hand or right hand side of a neck. The existence of a drift velocity, however, introduces a bias in the number of particles incident on the two sides (windward or lee side effect) which introduces an average force, always in the sense of retarding the drift. The drift velocity slows asymptotically to zero with respect to the wall. For a stationary wall, if the distance in which the drift velocity is reduced to a negligible fraction of the diffusion velocity (relaxation length) is a fraction α of the tube length, particles subsequently escaping to the entrance and exit will divide according to a diffusion law, ratio $(1 - \alpha)^{\frac{1}{2}}/\alpha^{\frac{1}{2}}$. For a moving wall, the diffused distribution is carried back to the entrance. Particles do not have to reach the wall speed to be returned; they need only be given a v_z toward the entrance.

Quantitatively, v'_x, v'_y, v'_z are the particle velocity components after reflection from a wall, inclination θ to the z direction, and incident with velocities v_x, v_y, v_z. Then

$$v'_z = v_z - v_q \sin\theta, \quad v'_x = v_x + v_q \frac{x}{R} \cos\theta,$$

$$v'_y = v_q + v_q \frac{y}{R} \cos\theta$$

$$v_q = 2[\sin\theta\ (v_z + v) - \cos\theta\ (v_x x + v_y y)]/R$$

$$R = a[\,1 - b \cos \frac{2\pi}{\lambda}\ (z + vt)], \quad \theta = \frac{2\pi ab}{\lambda}\ (z + vt).$$

In a Monte-Carlo computation, 500 particles, having the right-hand half of a Maxwell distribution of most probable velocity $\overline{v}$, are admitted with random directions and at points distributed uniformly over the starting plane, and traces their paths using the equations given above, until most have left the system either by return to the entrance end or by loss at the far end. The computation was done on the Los Alamos CDC 6600 computer and took 2-5 min per set of particles. Some particles can linger for long periods in the system; to follow these is wasteful in computer time since they do not affect the outcome very much. The computation was therefore stopped when their number had declined to a few percent. The fraction so remaining is given in the accompanying table, in which a = wall radius, ℓ = tube length, ab = wave amplitude, $2\pi ab/\lambda$ = roughness, v = wall velocity, $\overline{v}$ most probable velocity in Maxwell distribution. The line called adiabatic is the pure adiabatic albedo calculated for reflection at the first neck to provide a reference level for the magnitude of the cumulative effect.

The results show that the system works essentially as expected and that strong loss reductions can occur. Set I exhibits the completely adiabatic behavior of a low-roughness wall; the albedo for all is no larger than that calculated for the first neck, and it gets smaller as the velocity toward the source is increased. The next two sets, with increased roughness, are slightly nonadiabatic; the albedo is still increasing when the length is extended from 10 to 50 wavelengths and velocity helps.

				$v/\bar{v}$	Returned %	Lost %	Left %
I.	Long wavelength	$\lambda = 8a$	adiabatic	0	42		
	Medium amplitude	$b = 0.1$	fixed	0	38	62	
	Low roughness	0.025π					
	Long length	$20a = 2.5\lambda$	moving	1.0	9	91	
II.	Medium wavelength	$\lambda = 2a$	adiabatic	0	42		
	Medium amplitude	$b = 0.1$	fixed	0	54	42	4
	High roughness	0.1π					
	Short length	$20a = 10\lambda$	moving	0.2	65	33	2
III.	Medium wavelength	$\lambda = 2a$	adiabatic	0	42		
	Medium amplitude	$b = 0.1$	fixed	0	78	19	3
	High roughness	0.1π					
	Long length	$100a = 50\lambda$	moving	0.2	88	12	
IV.	Short wavelength	$\lambda = 2a/3$	adiabatic	0	26		
	Small amplitude	$b = 0.033$	fixed	0	60	34	6
	High roughness	0.1π					
	Short length	$20a = 30\lambda$	moving	0.2	71	26	3
V.	Short wavelength	$\lambda = 2a/3$	adiabatic	0	42		
	Medium amplitude	$b = 0.1$	fixed	0	92	0.4	8
	Very high roughness	0.3π					
	Long length	$100a = 150\lambda$	moving	0.2	100	0	0

Sets IV and II have the same roughness and the same length, but IV proves superior to II; the reduced neck ratio of IV is more than offset by the greater number of necks.

Set V is an extreme case to see how high the albedo might go. Even the static case gives a very acceptable degree of loss reduction.

Caution must be exercised in applying these examples to reality; the model used is simple and includes no plasma effects such as waves, shocks, and instabilities. At this stage, it is uncertain whether reality will be less or more favorable. But some simple points can be made: high roughness and high velocity both act favorably in the computation. There are limits to these quantities in reality, however; plasmas do not have infinitely sharp boundaries, and this sets an obvious limit to the roughness. If λ is made much less than, say, the sheath thickness, the perturbation will not penetrate deeply into the plasma. But the effect of this is not obviously fatal either; for example, if the outer layers only of the plasma were the ones retarded, the plasma would be progressively pared away. The limitation in velocity arises from the increasing voltage per turn of the traveling wave system, which is given by $2\pi^2 a^2 bvB/\lambda$. Taking the parameters of Set V, the largest albedo, but the highest voltage, and substituting $\bar{v}$ appropriate to a 10-keV plasma temperature, 1-cm plasma radius, and B_z of 100 kG, it is found that V/turn ~ 60 kV, frequency 15 MHz.

In magnitude, this is close to that required for the traveling wave stabilizing system of Haas and Wesson.[10] The data in the table given above can be used to check their results for wave entrainment effects which they did not include and might be harmful. It turns out that that system (long wave length but large amplitude) is adiabatic and therefore immune.

In conclusion, it would be idle to discuss further the stability and application of these apparently novel (to plasma physics) effects until more refined studies have been made, especially by computer plasma simulation and experiment.

The writer expresses his gratitude to C. Nielson for his skilled handling of the computation and to R. L. Morse for illuminating discussions.

References

1. W. E. Quinn, E. M. Little, F. L. Ribe, G.A. Sawyer, Plasma Physics and Controlled Nuclear Fusion Research, Int. Atomic Energy Agency, Vienna, 1966, Vol. I, p. 237.
2. D. V. Orlinskii, S.M. Osovets, V.I. Sinitsin, 1965 Culham Conference, Paper No. CN-21/136.
3. W. Gaede, Ann. Physik, 41, 337 (1913).
4. V.D. Fedorchenko, B.N. Rutkevich, B. M. Cherni, Zh. Tech. Fiz., 29, 1212 (1959).
5. K.D. Sinelnikov, B.N. Rutkevich, V.D. Federochenko, Zh. Tech. Fiz., 30, 249 (1960).
6. R.C. Wingerson, Phys. Rev. Letters 6, 446 (1961).
7. H. Dreicer, H.J. Karr, E.A. Knapp, J.A. Phillips, E.J. Stovall, J.L. Tuck, Nuclear Fusion 1962 Supp. I 299 (1962).
8. R.F. Post, Phys. Rev. Letters 18, 229 (1967).
9. R. L. Morse, Phys. Fluids 10, 1017 (1967).
10. F.A. Haas and J.A. Wesson, Phys. Rev. Letters 19 833 (1967).

SUMMARY OF FUNDAMENTAL PLASMA GROUP ACTIVITIES

(H. Dreicer)

During its first year of operation the Fundamental Plasma Physics group of the LASL Sherwood project has been largely engaged in the task of laying a firm foundation for future experimental activities. A major effort has been devoted to the design and construction of an alkali Q-machine. Although some component development is being continued, the major parts have been received, and they are now being assembled. All technical considerations which seem important in Q-machine operation have been scrutinized, and this has led to very definite ideas about cooling requirements, nozzle design, and design of electron bombardment systems for control of hot-plate temperature profiles. In the same connection, a photomicrographic study of crystal growth in hot plates has been started to determine if there is a relation between hot-plate surface inhomogeneity and the behavior of the contact ionized plasma. In the course of calculating the cooling requirements for a Q-machine tank, a study was made of the ion-neutral collisional effect on crossed-field diffusion with somewhat surprising results.

A second major effort has been directed toward the design of an electron cyclotron heated (ECH) Q-machine facility for producing steady-state quiescent plasma columns with any ion species and at electron temperatures far in excess of those possible in conventional alkali Q-machines. Parts for this device have been designed. A theoretical study has been carried out to determine the gas density and microwave power requirements as well as to understand the electron velocity distribution function produced. It has been found that it is possible for this function to be highly isotropic with respect to the angular distribution of electron velocities and it appears to be monotonic with respect to particle energies. This result is important for the stability of the device.

Successful operation of both of these facilities will depend upon the ability to produce desired magnetic field configurations accurately and to maintain them stably in time. For this reason an advanced computing code for designing magnets, developed at UCRL (Berkeley), has been placed into operation and a program has been initiated for adequately stabilizing all of the dc magnet supplies.

Two experiments inherited by the group have been discontinued. The first, an attempt by J. McLeod to develop a large-cross-section, large-current, low-voltage electron gun for beam plasma studies gave discouraging results. The second, a Ph.D. thesis problem started by D. Michael, involved an attempt to measure excited cesium atom cross sections by photoionization with laser light. This work was defeated by low signal-to-noise ratio.

Work has also proceeded on several theoretical problems. Although a general solution of the boundary-value Fokker-Planck problem has not been achieved, a class of special solutions has been obtained that can be constructed from the eigenfunctions for the problem. These should be useful in testing the accuracy of any future numerical solution obtained to the general case; they already indicate that any deviation from isotropy in the distribution function influences the space charge problem. During a visit here this summer, I. Bernstein (Yale University) suggested a new approach to the problem which will be tested during the coming months. The study of induced radiative recombination as it affects the interaction of intense laser light with plasmas has been continued. Although the work is not complete it appears to be of interest for the case of plasma formation by laser ionization of small solid drops. Inglis-Teller broadening and depression of the atom's series limit enters into these considerations in an important way.

It is a pleasure to acknowledge the expert help of N. Gardner and A. Mondragon in all phases of the group's experimental work.

NUMERICAL COMPUTATION OF TEMPERATURE AND DENSITY PROFILES IN AN ALKALI-METAL PLASMA DEVICE

(D. Henderson)

Introduction

Several numerical calculations have been undertaken to help in the design of the alkali-metal plasma device (Q-machine). One of these, aimed at optimization of the magnetic field geometry, is discussed later in this report. The others give the hot-plate temperature distribution, the injected neutral flux distribution, and the plasma density distribution for an axisymmetric device. Once the completed device is in operation, these numerical programs will be useful in planning experiments and interpreting data.

Temperature Profiles

In general, hot (ionizer) plates have been considered which are heated from behind by electron bombardment and which are welded to a concentric support disk. This design tends to provide complete axial symmetry and also to prevent any bombardment electrons (or secondaries thereof) from entering the plasma region. Such a hot-plate system, however, has a significant conduction loss of heat from the edge of the hot plate.

To calculate the temperature within the hot plate (in both the radial and axial directions) use has been made of a pre-existing machine program called MAÑANA.[1] MAÑANA breaks up the material (plate plus support disk) into discrete mass points (nodes) and evaluates the conductance between adjacent nodes. Applying boundary conditions, i.e., the input power at the back of the plate, the fixed temperature at the edge of the support, and radiation losses, it relaxes from some preassigned initial temperature distribution to a self-consistent one such as shown in Fig. 2. This shows isotherms obtained at 50° intervals. The input power is in a single ring at two-thirds radius. The arrows at the top of the figure indicate the temperatures derived from a one-dimensional program. The program is useful for the detail attained, but requires a good deal of computer time (1 h for Fig. 2) on the IBM 7030.

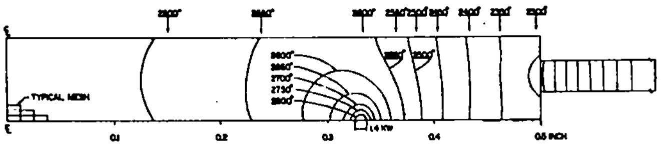

Fig. 2. Results of MAÑANA calculation.

If the axial temperature variations are neglected, the problem reduces to an ordinary differential equation

$$\frac{1}{r}\frac{d}{dr}\left(r\kappa t\frac{dT}{dr}\right) = 2\epsilon\sigma T^4 - S(r), \tag{1}$$

where r is the radial station, t the thickness, κ the thermal conductivity, T the absolute temperature, ε the emissivity, σ the Stefan-Boltzmann constant, and S(r) the applied power in (say) kW/cm^2. The factor "2" comes from allowing radiation from both sides of the hot plate. As a two-point boundary value problem (dT/dr = 0 in the center and T = const. at the outer edge) Eq. (1) may be easily solved by iteration of a Runge-Kutta routine. This scheme has been used as a general design aid in studying the effect of changing κ and t as well as S(r). In doing these calculations, it is learned which temperature profiles (monotonic increasing, monotonic decreasing, single maximum, two maxima, etc.) are reasonable and how to achieve them. These solutions are also useful for providing the initial temperature distribution for MAÑANA since doing so reduces the number of iterations required.

Alternatively, following a suggestion of Dreicer, the problem has been inverted to find the power distribution, S(r), required for a desired temperature distribution. Eq. (1) is applied directly over the ionizer plate and then a concentrated annular source is added as is required for the conduction loss through and radiation loss on the disk (on which S(r) = 0). This loss is computed by solution of Eq. (1) as a two-point boundary value problem over the concentric support disk alone. This has been applied to the design of an isothermal hot-plate system, now under construction, for which the temperature distribution is shown in Fig. 3. The upper portion, calculated with the

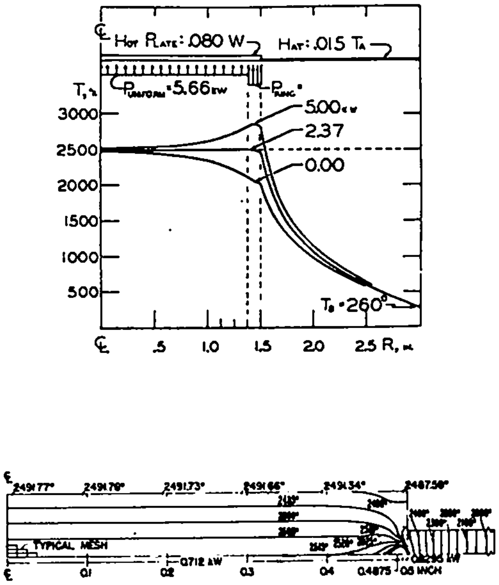

Fig. 3. Temperature distributions in hot-plate system designed to give an isothermal surface.

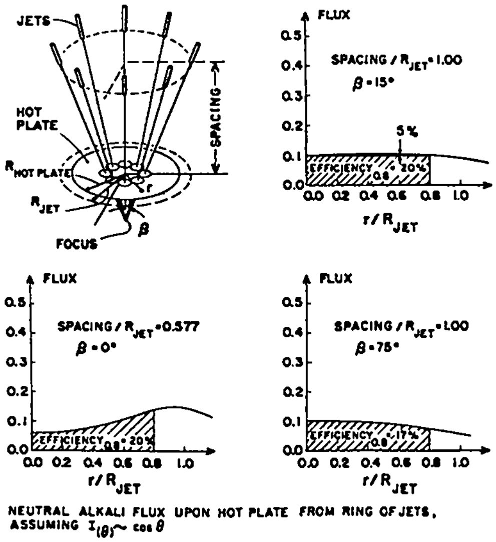

Fig. 4. Neutral alkali-metal flux distributions on the hot plate (and support disk) from a ring of jets.

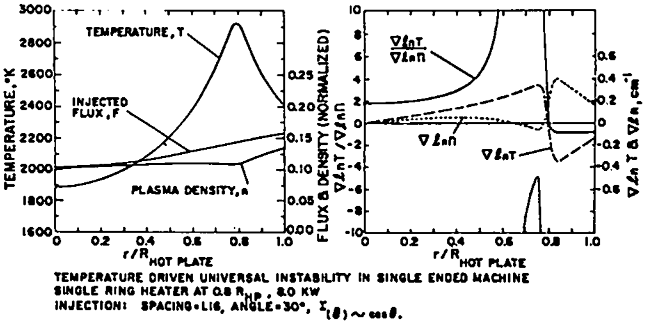

Fig. 5. Parameters calculated for a single ring heater (Fig. 2) and a ring of alkali metal jets (Fig. 4).

one-dimensional program, shows the effect of varying the annular ring power for a system now under construction, whereas the lower portion gives 5°-isotherms and surface temperatures obtained with the MAÑANA program for a smaller system. The hot-plate system being constructed is described later in this report.

Neutral Flux Profiles

Plans are being made to supply the neutral alkali-metal flux to the hot plate in a number of beams supplied from many jets in a manifold as indicated in Fig. 4. The flux is normalized so that the area under each curve is the fraction of alkali-metal vapor striking the plate within a given radius. Given the angular distribution function, $I(\theta)$, for a single jet, the values are summed over the many jets in a straightforward manner. The objectives are to achieve a desired profile and to maximize the fraction of alkali-metal vapor input which falls on the useful portion of the hot plate. Three cases are shown in Fig. 4. Unfortunately the function $I(\theta)$ is not accurately known, and so simple forms (e.g., $\cos\theta$, $\cos^2\theta$) are assumed in these calculations. An experiment is being assembled to measure $I(\theta)$.

Plasma Density Profiles

Once the hot-plate temperature and neutral flux profiles are known, the plasma density, plasma potential, etc., can be calculated through solution of the detail balance equations. These are useful for the design of experiments for which it is necessary to know what $T(r)$ and flux distributions are required to bring out some expected effect, and for the interpretation of data. As an example, Fig. 5 shows the conditions chosen to give a large value for the quantity $d(\log T)/d(\log n)$ which enters into the criterion for stability against temperature and density gradient universal instabilities. In this example calculation the product of the probability of ionization times the neutral injection flux has been balanced with the product of the plasma density times the streaming velocity. For the streaming velocity the ion thermal speed has been used, neglecting the sheath effect. In particular cases, these sheaths will be important, as pointed out privately by Righetti (Frascati).

Reference

1. R. F. Thomas, Jr. and M. D. J. MacRoberts, LA-3264-MS.

Fig. 6. Main tank of Q-Machine.

DEVELOPMENT OF ALKALI-METAL Q-MACHINE COMPONENTS

(H. Dreicer, D. Henderson, F. Wittman)

Main Tank

Components of the alkali-metal Q-machine vacuum tank, designed with the help of J. McLeod, R. Dike, and C. Charlton, have been received and are being tested prior to their installation in the magnet. The main stainless steel tank has an $15\frac{5}{8}$-in. internal diam and is 84 in. long (Fig. 6). Stainless steel cross arms, provided with five access ports each, are attached to the main tank at each end. All seals are made with metal gaskets. Hot-plate power absorbed by the main tank wall is to be removed by pumping coolant through a double-walled jacket. Calculations indicate this design to be considerably more efficient than the usual method of conducting heat to a coolant passing through tubing welded to the chamber wall.

To maintain a highly ionized plasma, i.e., to avoid major interactions between electrons, ions, and alkali-metal neutrals, it is considered necessary to control the vapor pressure of the alkali metal condensed on the chamber wall. The wall temperature necessary for this cannot be predicted precisely, because the relevant ion-neutral collision cross sections are generally not available or are known only with large uncertainty. An interesting ion-neutral interaction which may affect the operation of an alkali-metal Q-machine is discussed in a separate section below.

Preliminary engineering estimates indicate that a refrigeration unit, pumping coolant with a wide temperature range available below 0°C, is feasible, but costly. For this reason future operating wall temperature cannot yet be firmly predicted.

Hot Plates

During the past summer the first prototype hot-plate assembly, based upon the computations made by D. Henderson, was completed. This assembly incorporates two thin tungsten foil filaments and an auxiliary tungsten hot plate to produce a controlled temperature distribution on the main hot plate by programming three separate electron beam bombardment systems. The two bombardment beams which heat the final hot plate take the form of a coaxial system in which a solid cylindrical electron beam is surrounded by a hollow cylindrical beam. The former supplies the $\epsilon\sigma T^4$ power radiated by the hot plate, whereas the latter provides the heat conducted off the hot plate by the thin annular plate which supports it. It is hoped that, by varying the bombardment voltage of the two beams independently, various radial temperature gradients, as well as the highly isothermal case, can be programmed. The electrical connections are shown in Fig. 7 and assembly views in Figs. 8 and 9. Initial tests of this system have been limited by mechanical problems encountered at 2000-3000°K, and considerable development remains to be carried out.

Following a suggestion of L. Agnew an attempt has been made to construct isothermal hot plates based upon the Grover heat pipe principle.[1] This technique involves the use of a hollow tungsten pill-box shaped cavity in which liquid silver and its vapor coexist at a temperature in the neighborhood of 2300°K. Such a heat pipe transfers heat by mass flow of the silver utilizing its latent heat. Heat addition into one end of the cavity is distributed throughout by evaporation of the liquid and condensation of the vapor. Of seven pill boxes formed by tungsten vapor deposition onto copper mandrels, one survived the last electron beam welding operation, and is ready to be tested.

Electron Bombardment Power Supplies

Orders for two highly regulated electron bombardment supplies, 5 kV at 8 A and 5 kV at 5 A, have been awarded to a vendor. Delivery is expected in December 1967.

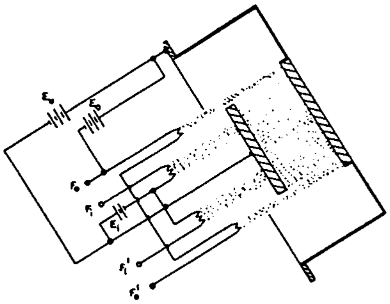

Fig. 7. Electrical connections of three-stage (electron bombardment) hot plate.

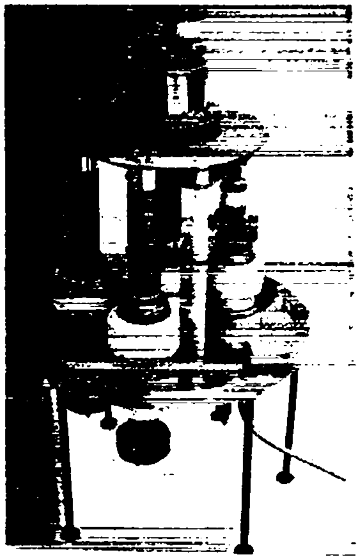

Fig. 8. Partial assembly of hot-plate bombardment system.

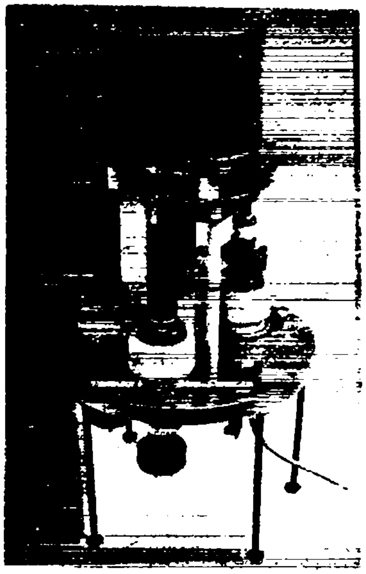

Fig. 9. Complete assembly of hot-plate bombardment system; hot plate is welded into "top-hat" support structure.

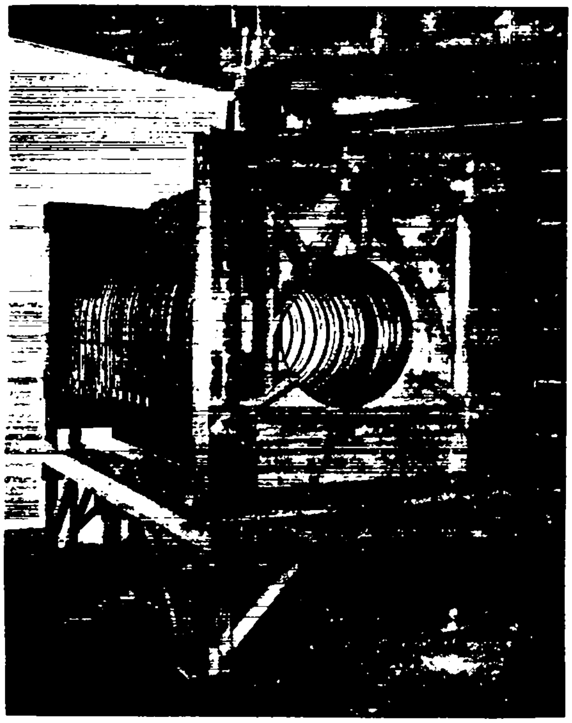

Fig. 10. Magnet and support stand.

Alkali-Metal Nozzle Design

Optimum design of the atomic beam source which sprays the hot plate with alkali-metal atoms requires a knowledge of efflux from a single atomic beam nozzle as a function of direction. An apparatus to measure this quantity is nearly assembled.

Atomic Beam Oven

A resetability of ± 0.1% in the vapor pressure in the chamber feeding the atomic beam nozzle requires a resetability of at least ± 0.1°C in the temperature of the oven supplying alkali-metal atoms. To accomplish this, the oven has been placed in an oil bath whose temperature is to be stabilized with a proportional-type of temperature controller. In order to remove the non-condensible impurities in the alkali metal, the oven will be loaded through a vacuum distillation apparatus which has been constructed as part of the source.

Magnet

The magnet support stand has been received and the 20-in. i.d. pancake coils have been assembled on it (Fig. 10). Magnetic field design and stabilization of magnet power supplies are discussed in separate sections below.

Reference

1. J. E. Deverall and J. E. Kemme, High Thermal Conductance Devices Utilizing the Boiling of Lithium or Silver, LASL, LA-3211 (1965).

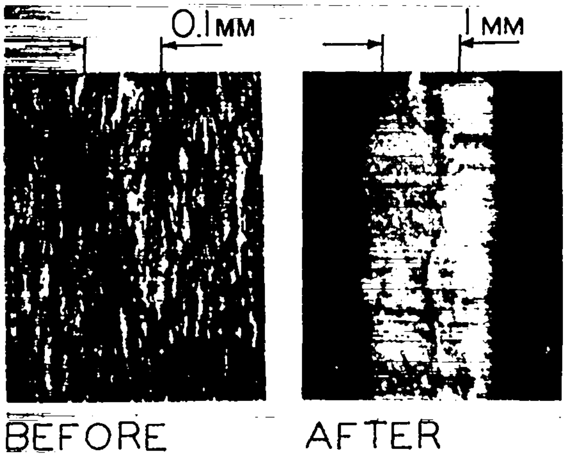

BEFORE AFTER

Fig. 11. Photomicrographs of 0.8-in. thick tungsten hot plate before and after heating at $\sim 2500^{\circ}$K for several hours.

PHOTOMICROGRAPHS OF HOT PLATES

(H. Dreicer, D. Henderson)

In the various calculations on heat transfer and plasma profiles (see, for example, the section by D. Henderson above), the assumption was implicit that the material properties of the hot plate were uniform to all scale lengths of interest including the ion gyration radius (~ 1 mm to 1 cm). To investigate the truth of this assumption, photomicrographs have been taken (with the help of T. Jones and C. Javorsky, LASL CMB Division) of hot-plate surfaces which have been subjected for various lengths of time to high temperature.

An edge-on view of a sliced sample of an 0.080-in. thick tungsten hot plate before and after it was heated at $\sim 2500^{\circ}$K for several hours is given in Fig. 11. As a result of this heating, the individual grains have grown until their dimension perpendicular to the hot-plate surface is of the order of the hot-plate thickness, with some smaller crystals retained along the grain boundary. It is noteworthy (although not apparent from Fig. 11) that the grain dimension parallel to the hot plate surface is about 1 in. Thus grain dimensions when viewed from the larger front surface might be even larger; a preliminary investigation of the front surface bears this out.

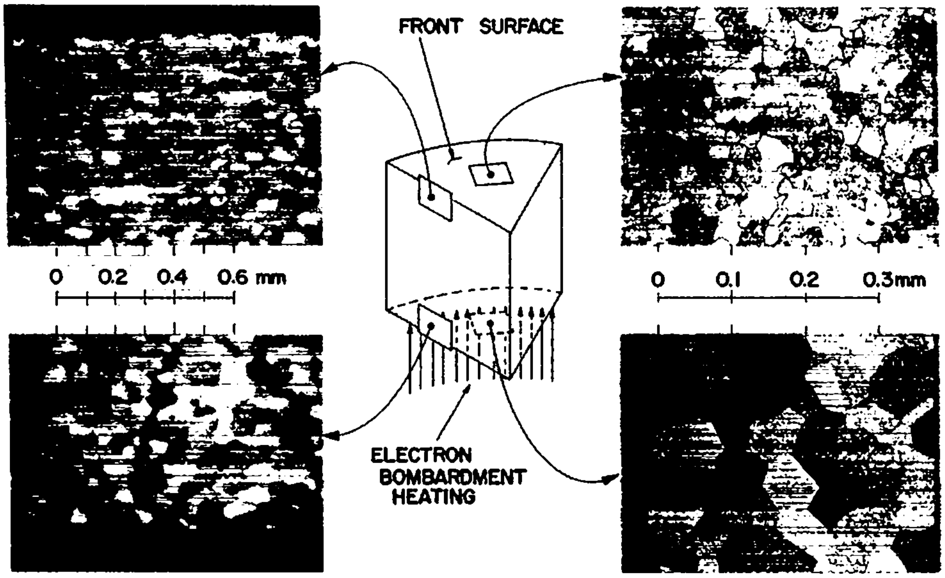

Fig. 12. Photomicrographs of 0.25-in. thick tungsten hot-plate heated at 2300°K for half an hour.

Figure 12 shows photomicrographs of a 0.250-in. thick tungsten hot plate which was heated to 2300°K for about half an hour. The grains have grown from the initial size (Fig. 11), but have not yet reached dimensions comparable to the plate thickness. It will be noticed, in particular, that the grains have grown more quickly at the back of the plate which was hotter.

Since tungsten has a body-centered cubic lattice, its thermal conductivity is probably not anisotropic with respect to crystal orientation, but this is not certain. The thermal emissivity and electron work function, however, vary with the crystal face. For example, the work function of tungsten is known to vary by 0.4-1.0 eV between the 100 and 110 crystal planes.[1] Different grains might therefore be expected to have different surface temperatures and electron emission properties. The actual variation of these properties on the surface of a hot plate is probably not as large and as sharply bounded by grain boundaries as indicated by this argument since the surface is uneven, with mountains and valleys distributed over each grain. Magnetic lines will intersect various crystal planes even over a single grain, leading to a range of values of the emissivity and work function over a single grain. There is consequently uncertainty about the scale length L over which uniformity exists. It will be assumed, however, that there is such a value for L.

If the ion gyration radius is large compared to L, then these effects may be averaged out in the plasma in contact with the hot plate; however, this is not certain since the inhomogeneities in electron emission may be the controlling factor. On the other hand, if the ion gyration radius is small compared with L then different plasma properties may be expected along magnetic field lines which intersect the regions of different surface properties. Since the grains were found to grow to the order of the plate thickness and larger, the latter case will perhaps apply. These results imply a different limitation on Q-machine operation than is usually considered. In particular, the inherent surface inhomogeneities discussed here may be an important source of transverse electric fields which drive E x B diffusion; for this reason the subject must be pursued further.

Reference

1. M. Kaplit, Proceedings of the IEEE Thermionic Conversion Specialist Conf. Houston, Texas (1966). p. 387.

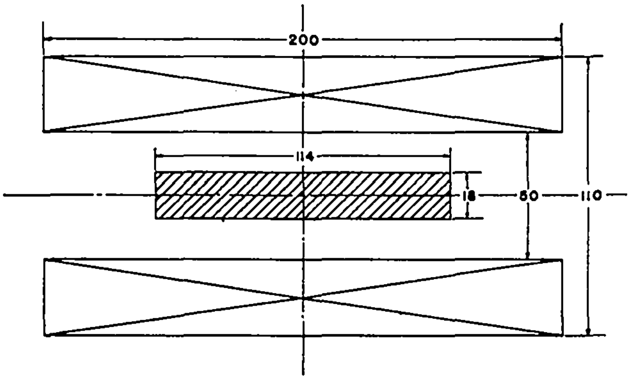

Fig. 13. A magnet configuration for producing a uniform field over a large (shaded) volume (dimensions in cm).

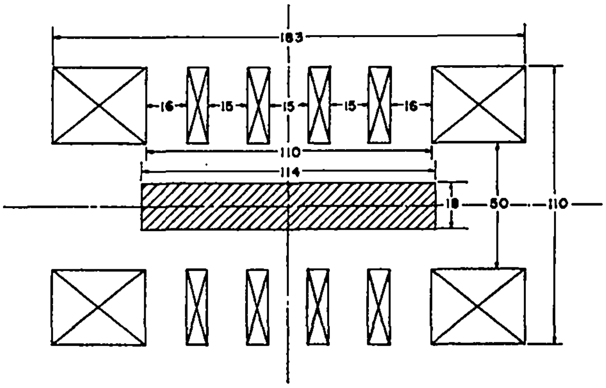

Fig. 14. A magnet configuration with gaps for producing a uniform field over a large (shaded) volume (dimensions in cm).

MAGNETIC FIELD DESIGN

(J. McLeod)

A digital computer code (CSYD) capable of automatically designing an air-core electromagnet to produce any specified field, proposed by K. Halbach[1] and developed by R. Holsinger (UCRL, Berkeley).has been put into use. (The writer is indebted to R. Lewis for assistance in the initial establishment of this code at LASL.) It has proved to be a powerful new tool capable of remarkable design feats with relatively little effort on the part of the user.

The CSYD code has been used to determine the best uniformity available in each of a variety of different configurations of the existing 20-in. bore electromagnet which consists of 50 separate sections and will be used to provide the magnetic field for the alkali-metal Q-machine. Quite remarkable uniformity appears to be possible in very short magnets by judicious location of a few small gaps, and by doubling the current for a short distance at each end. The length of the magnet shown in Fig. 13 is only 2.5 times its average winding diameter, but it produces a field which is uniform, in principle, to 1 part in 10^6 (rms deviation) throughout the shaded region. This theoretical uniformity is probably not realizable in practice, because of unavoidable errors in fabricating a high-current (3500 A) electromagnet, but the power of the calculating technique is interesting nonetheless.

Even magnets with several large gaps can have reasonably high uniformity if the gaps are located correctly. The magnet shown in Fig. 14 produces a field which is uniform over the shaded region to 0.1% (rms deviation) in spite of five major gaps providing radial access to the shaded region. In order to study the limitations on field homogeneity imposed by magnet winding errors and imperfections, 36 of the 20-in. bore pancake windings were set up in a configuration which was predicted by CSYD to have a uniformity sufficient for narrow line width operation of a nuclear magnetometer. No evidence of broadening of the nuclear resonance line by field inhomogeneity was observed even at full generator power (7200 G). For conventional pancake spacings it had previously not been possible to operate the nuclear magnetometer at high fields because of this line broadening. The accuracy of the magnetometer measurements was limited to 0.03% by hunting in the generator regulator. Within this accuracy, no discrepancies were found between the observed and predicted fields when both were normalized to a single point. Fields were measured along a 4-ft section on the axis of the solenoid. Although the limitation on field homogeneity imposed by magnet winding errors and imperfections has not been found, this measurement nevertheless indicates an obvious improvement in field homogeneity over what has been observed with conventional pancake configurations in the past.

CSYD has also been applied to the 11-in. i.d. pancake magnet to predict configurations which will give magnetic fields uniform enough to be suitable for precision cyclotron measurements. Again extremely uniform fields are found to be possible in principle, but regulation of the Sherwood power supplies will be necessary before their actual feasibility can be verified.

Reference

1. K. Halbach, "A Program for Inversion of System Analysis and its Application to the Design of Magnets," UCRL-17436 (July 1967).

ION-NEUTRAL COLLISION EFFECTS ON CROSS-FIELD DIFFUSION OF ALKALI-METAL Q-MACHINE PLASMAS

(H. Dreicer, D. Henderson)

Measurements of diffusion of alkali-metal plasmas across magnetic field lines have been interpreted on the basis of (1) electron-ion encounters, (2) end plate recombination and reionization, and (3) numerous instability and plasma wave mechanisms. A fourth mechanism which should be added to this list may become important if the density of alkali-metal neutrals becomes significant.

Consider an alkali plasma column of radius R, density n_e, and temperature $T_e = T_i$, which is immersed in a static magnetic field B and a background neutral alkali-metal gas at density n_g. The diffusion of a charged particle across the magnetic field occurs roughly at the rate

$$\nu = \frac{D}{R^2} \simeq \frac{\ell^2}{R^2\tau} .$$

This quantity is the inverse of the average particle's lifetime when it is lost by diffusion. The diffusion coefficient D may be approximated by the square of the relevant gyration radius ℓ over the mean free time τ for collision. For electron-ion encounters this diffusion rate becomes

$$\nu_{ei} = \ell_e^2/(R^2\tau_{ei}),$$

where $\ell_e = v_e/\omega_{ce}$, $v_e = \sqrt{2kT_e/m_e}$, $\omega_{ce} = eB/m_e$, and $\tau_{ei} = 0.266\, T_e^{\frac{3}{2}}/(n_e \ln\Lambda)$sec.[1] In the mean free time formula for τ_{ei} the temperature T_e is given in °K and n_e in cm^{-3}; $\ln\Lambda$, the Coulomb logarithm, is approximately 5. For ion-neutral encounters

$$\nu_{ni} = \ell_i^2\, n_g\, \overline{\sigma v}/R^2,$$

where $\ell_i = v_i/\omega_{ci}$, $v_i = \sqrt{2kT_e/M_i}$, $\omega_{ci} = eB/M_i$, σ = cross section for both elastic and resonant charge exchange collisions, and $\overline{\sigma v} \approx \sigma v_i$. These collision processes may be compared by a ratio Q defined as

$$Q = \frac{\nu_{ni}}{\nu_{ei}} = \frac{1}{4}\,\frac{M_i}{m_e}\,\frac{n_g}{n_e}\,\frac{\sigma v_i T_e^{\frac{3}{2}}}{\ln\Lambda} .$$

For cesium, $M_i = 133$ and for potassium, $M_i = 40$; consequently, at 2500°K

$$Q \approx 5 \times 10^{13}\, \sigma \frac{n_g}{n_e}$$

for both cesium and potassium. There are few data on σ, but a commonly quoted[2] measurement on cesium ion-atom collisions provides a σ which varies from 1.6×10^{-13} cm^2 at $kT_e = 4$ eV to 6.8×10^{-13} cm^2 at $kT_e = 0.12$ eV. If σ is taken as 2×10^{-13} cm^2, then, for the case of interest, $kT_e = 0.22$ eV, $Q = 1$ for $n_g \approx 0.1\, n_e$, i.e., for an ionization degree $n_e/(n_e + n_g)$ of 0.91.

One source of alkali-metal neutrals in Q-machines is the vapor pressure of the alkali metal condensed on the wall at the temperature T_w. Table 1 gives cesium plasma densities and the corresponding maximum wall temperatures permitted to maintain n_g such that $Q \leq 1$, for two values of σ.

Table 1

	T_{wall}	
n_e (cm^{-3})	$\sigma = 2 \times 10^{-13}$ cm^2	$\sigma = 2 \times 10^{-14}$ cm^2
10^{12}	33°C	60°C
10^{11}	11	33
10^{10}	-9	11
10^{9}	-26	-9
10^{8}	-41	-26

The calculation assumes an equilibrium between evaporation and condensation of alkali-metal atoms at the wall. If local hot spots exist, as might occur in a Q-machine with white-hot end plates, then the neutral gas pressure might be unpredictably larger, because the pumping speed to cold surfaces is reduced. Excess neutrals injected from the atomic beam source which do not impinge on a portion of the end plate hot enough to ionize will also cause n_g to exceed the equilibrium vapor pressure value.

The diffusion analysis presented here is admittedly rough. When ions step across the magnetic field due to interaction with neutrals, ambipolar fields will develop unless efficient short circuiting of potentials along neighboring field lines is possible. In conventional Q-machines this is achieved by the flow of electrons along field lines and their flow across the field lines by conduction through the hot plates. In the collisionless limit this mechanism operates efficiently. It is clear from the results presented in Table I that considerable caution must be exercised to keep the neutral alkali-metal gas pressure low by careful nozzle design and by insuring that the tank wall is uniformly at low temperature.

References

1. L. Spitzer, "Physics of Fully Ionized Gases," Interscience Publishers, Inc.

2. J. M. Houston, Proceeding of the IEEE Thermionic Conversion Specialist Conf., Cleveland, Ohio (1964), p. 304.

REGULATION AND SPLITTING OF D.C. MAGNET POWER SUPPLIES TO BE USED FOR FUNDAMENTAL PLASMA EXPERIMENTS

(H. Dreicer, E. Kemp, M. Talcott)

During the past year a study was made on ways and means of improving the LASL dc power supplies available for plasma physics experiments. The goal was to transform the present 500-kW motor generator set with 1% stability to 0.01% long-term stability and the 2.5-MW rectifier supply with 15% stability to two 1.25-MW supplies with 0.01% long-term stability, with provision, when necessary, for reconnecting the two 1.25-MW systems into a single 2.5-MW supply with the same stability. These modifications will permit the utilization of several existing magnets simultaneously, at high fields, with the stability necessary for many resonant absorption, radiation, and wave propagation experiments.

After considerable study it was decided to use a power series transistor regulator system. At this time a prototype system consisting of four 30-transistor heat sinks has been tested under open loop conditions. Two prototype transistor heat sinks passing 200 A have been operated under closed loop conditions with a 30-min stability of about 1:5000. All components necessary for splitting the 2.5-MW system have been ordered. Spring 1968 is scheduled as the completion date for this work.

VELOCITY DISTRIBUTIONS ASSOCIATED WITH BOUNDED QUIESCENT PLASMAS

(H. Dreicer, W. Riesenfeld)

The general problem, to which no solution is offered, may be posed with the help of the following mental picture. Consider the distribution of electrostatic potential between two hot plane-parallel thermionically emitting walls containing a plasma of electrons and positive ions, and carrying an electrical current by virtue of an externally applied potential. Two sheaths are seen several Debye lengths in thickness, one near each wall, with a different potential drop across each, joined by a region of uniform potential. This central region, depending upon circumstances, may for example be a potential well for most ions. A complete description of the problem involves Boltzmann equations with collision terms for each species and the Poisson equation which couples these terms, as well as suitable boundary conditions. In order to understand the problem it is necessary to study various effects separately.

An attempt was made to solve a small facet of this problem by making the following assumptions:

(1) The electric potential is independent of spatial position.

(2) Positive ions are randomly distributed between the two walls and are infinitely massive.

(3) Electron-electron encounters are ignored.

(4) Applied potential and thus electric current vanish.

Electron-ion encounters and the spatial gradient term in the Boltzmann equation which together yield the time independent equation

$$\frac{\partial f(x,\mu;v)}{\partial x} = \frac{1}{\mu}\frac{\partial}{\partial \mu}\left[(1-\mu^2)\frac{\partial f}{\partial \mu}\right], \qquad (1)$$

must, however, not be overlooked. Here the position x of the electron normal to the walls is measured in terms of the mean free path

$$\ell = v^4/\Gamma$$

where

$$\Gamma = \frac{4\pi ne^2}{m^2} \log \frac{\lambda D}{P_o}$$

in familiar terminology. The equation is thus parametric in the particle speed v. The scattering angle θ is measured with respect to the normal to the walls.

Assumption (1) allows Poisson's equation to be ignored and, roughly speaking, is equivalent to prescribing the boundary conditions upon f several Debye lengths away from the true wall in the region where the potential is constant. Assumption (2) permits the ion-ion encounters, as well as the equation for ions, to be ignored. Assumption (3) linearizes the electron equation, and probably results in a distribution function which exhibits the worst anisotropies that are apt to be encountered. Assumption (4) permits a solution of the problem by separation of variables. It should be emphasized, however, that these assumptions are not necessarily consistent with each other. In particular.assumptions (1) and (2) are generally not consistent, as a direct consequence of electron-ion encounters.

The solution to Eq. (1) may be written in the form

$$f(x,\mu;v) = \sum_{\lambda_n} C_{\lambda_n} e^{-\lambda_n x} S_{\lambda_n}(\mu), \qquad (2)$$

where the $S_{\lambda_n}(\mu)$ form an orthogonal set of eigenfunctions, and the λ_n are the corresponding eigenvalues. Approximate analytic solutions and more exact numerical solutions for the S_{λ_n} and λ_n have been obtained, (the latter in collaboration with I. Cherry of T Division at LASL). The first few λ_n are

$\lambda_o = 0$

$\lambda_1 \simeq 14.5;\ \lambda_{-1} \simeq -14.5$

$\lambda_2 \simeq 42.0;\ \lambda_{-2} \simeq -42.0$

$\lambda_3 \simeq 83.3\ \ \lambda_{-3} \simeq -83.3.$

The corresponding S_{λ_n} are $S_{\lambda_o} = 1$, and other oscillating functions which exhibit standard eigenfunction behavior in that they possess a number of zero crossings equal to $|n|$. S_{λ_1} and S_{λ_3} are shown in Figs. 15 and 16.

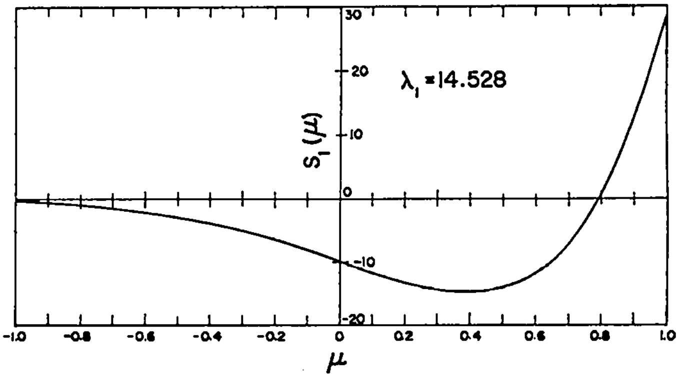

Fig. 15. $S_{\lambda_1}(\mu)$ versus μ = cos θ.

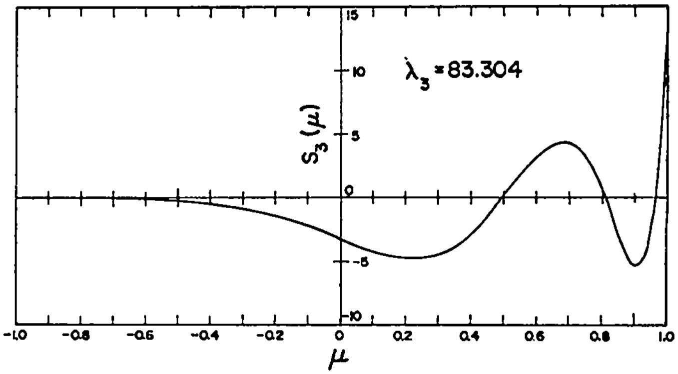

Fig. 16. $S_{\lambda_3}(\mu)$ versus μ = cos θ.

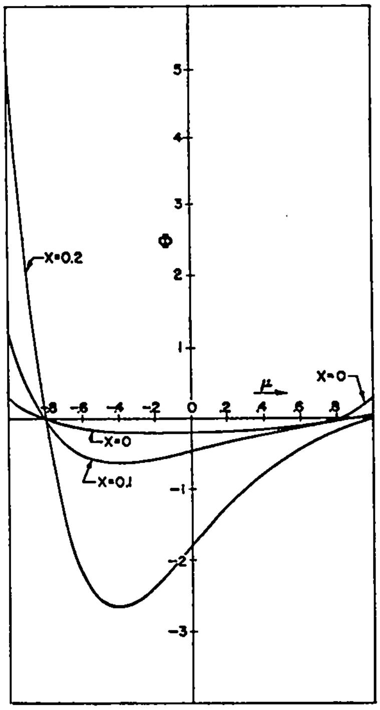

Fig. 17. The anisotropy parameter Φ (for n = 1) vs μ with the position x as parameter.

To obtain the C_{λ_n} it is necessary to prescribe boundary conditions partly on each wall at $x = \pm a$, i.e., $f(-a,\mu;v)$ and $f(a,\mu;v)$ are provided for $0 < \mu < 1$ and $-1 < \mu < 0$, respectively. This results in an infinite set of linear equations for the C_{λ_n}. A truncation procedure for obtaining approximate coefficients was tried, but was found to converge too slowly to be of any value. Fortunately two cases may be handled more simply:

(a) $f(\pm a,\mu;v)$ = constant. In this trivial case $f(x,\mu;v)$ = constant everywhere. This corresponds to thermal equilibrium.

$$\text{(b)}\ f(x,\mu;v) = C_o + C_{\lambda_n}\left[e^{-\lambda_n x}S_{\lambda_n}(\mu) + e^{\lambda_n x}S_{\lambda_n}(\mu)\right] = C_o + C_{\lambda_n}\Phi.$$

In this more interesting case the boundary condition involves only a single eigenfunction in addition to S_{λ_o}, and thus $f(\pm a,\mu;v)$ is not really an arbitrary function. Nevertheless, this case illustrates the role played by the eigenvalue λ_n in the relaxation of f in real space, and provides an exact solution to a special case. This is useful, because other solution techniques must reproduce the result.

The anisotropy factor Φ is shown in Fig. 17 for n = 1. If the walls are located at $x = \pm a = \pm 0.2$ then the curve marked $x = 0.2$ gives the boundary condition for $a = 0.2$, and the curves marked $x = 0.1$ and $x = 0$ illustrate the relaxation of the anisotropy with position moving away from the wall toward the central plan $x = 0$.

Eq. (2) shows that the electron density

$$\int_{-1}^{+1} f(x,\mu;v)\,d\mu$$

is usually a function of x. If it is chosen equal to the ion density at the plates it will deviate from it in the interior of the plasma. This result indicates that, in general, the degree of anisotropy of the velocity distributions must affect the distribution of charge density and potential.

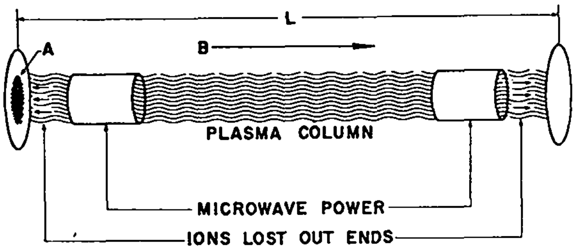

Fig. 18. Electron cyclotron heating system.

ELECTRON CYCLOTRON HEATING (ECH) Q-MACHINE

(H. Dreicer, J. McLeod)

Design and component testing is under way on an electron cyclotron heating (ECH) facility (Fig. 18) for producing a plasma column in a magnetic field, similar to that reported by Lisitano.[1] The motivation behind this work is the development of another quiescent plasma source for fundamental studies which utilizes any ion species and operates at average electron energies far in excess of those possible in conventional thermally heated alkali-metal Q-machines. In anticipation of experimenting with such a device, an analysis has been started of the conditions under which a plasma column can be maintained in a steady quiescent state by electron cyclotron heating and ionization.

Among the numerous effects which may enter such an analysis are line-tying of interchange instabilities, universal drift instabilities driven by temperature or density gradients, and microinstabilities due to anisotropies and double-humped velocity distributions. Whereas low-frequency interchange instabilities and universal drift instabilties might be controlled by techniques applicable to open-ended magnetic systems, the method of dealing with the microinstabilities driven by peculiar properties of the velocity distribution f is less obvious, especially since the plasma is maintained by microwave ECH fields. For this reason the first efforts are being made to the study of the properties of f and the average plasma parameters required for steady state operation.

A plasma column of the type pictured in Fig. 18 is maintained against continuous loss of particles to the container end wall (or out of a magnetic mirror) by electron ionization of neutrals. Even if the average electron travels many times the length of the column before making such an ionizing collision with a neutral, it must make exactly one during its lifetime in the machine to maintain steady state. This fact determines the neutral gas density required. For if the principal loss is collisionless ambipolar streaming along the magnetic lines to the end wall intersecting the column, then

$$n_e \bar{\nu}_i V = \text{ion end-wall current,} \qquad (1)$$

where n_e = electron density, V = plasma volume over which ionization can occur, and $\bar{\nu}_i$ = average ionization frequency.

The ion end-wall current along the magnetic field can be determined approximately from the argument that most of the electrons must be reflected by a sheath which accelerates the ions and retards those electrons which reach the wall. Such a sheath is usually characterized by a potential drop of several times kT_e, where $\frac{3}{2}kT_e$ equals the average electron energy.[2] Thus the ions gain energy $\frac{1}{2} M\bar{v}_i^2 \approx 5kT_e$ by the time they strike the wall. The electric field of such a sheath extends deep into the plasma and accelerates the ions toward the end wall so that the ion velocities are not really random.

A rough approximation, suitable to the present purpose, for the ion end wall current can be obtained by employing the expression for the net flow in one hemisphere of an isotropic velocity distribution and using the electron temperature to calculate the average ion speed.[2] Consequently,

$$n_e \bar{\nu}_i V = 2\left(\frac{n_e \bar{v}_i}{4}\right) A, \qquad (2)$$

where $\bar{v}_i = (2kT_e/M)^{\frac{1}{2}}$ = average ion speed, A = cross-sectional area of plasma column, and the factor of 2 arises because the column has two ends. The average ionization rate depends upon f. Assuming a Maxwellian distribution and an ionization rate given by[3]

$$\nu_i(u) = \nu_e h_i (u - u_i)$$

with ν_e = electron-neutral elastic collision rate, h_i = constant determined empirically[3] and by best fit to data of Phelps, et al.[4], u = electron energy in eV, and u_i = ionization potential of the neutral atom then

$$\bar{\nu}_i = \nu_e h_i \left\{ \frac{3}{\sqrt{\pi}} \left(u_i T_e\right)^{\frac{1}{2}} \exp\left(-u_i/T_e\right) + \left(\frac{3}{2} T_e - u_i\right)\left[1 - \mathrm{Erf}\left(\sqrt{u_i/T_e}\right)\right] \right\} \qquad (3)$$

$$\mathrm{Erf}(x) = \frac{2}{\sqrt{\pi}} \int_0^x e^{-t^2} dt,$$

where in this equation and henceforth kT_e/e is abbreviated by T_e. Barred quantities have been averaged over the distribution function. Since ν_e is linearly proportional to the neutral gas pressure, p, $\bar{\nu}_i$ is also proportional to p and hence to the neutral gas density n_g. Table 2 lists $\bar{\nu}_i/\nu_e$ as a function of the average electron energy, $\bar{u}$, for the case of molecular hydrogen for which $h_i = 7.8 \times 10^{-3}$, $u_i = 16.2$ eV, $\nu_e = 6 \times 10^9$ p sec^{-1} with p in torr.

Table 2

$\bar{u}$ (eV)	$\bar{\nu}_i/\nu_e$	u* (eV)
4	1.6×10^{-4}	330
6	1.5×10^{-3}	100
10	1.1×10^{-2}	65
16	3.8×10^{-2}	80
25	9×10^{-2}	110
40	0.20	170
60	0.35	250

By combining Eqs. (2) and (3) and setting V/A = L, the required neutral gas pressure is found to be

$$p \simeq \frac{10^{-4}\sqrt{T_e}}{\left(\bar{\nu}_i/\nu_e\right) L} \quad . \qquad (4)$$

Thus for L = 40 cm, $\frac{3}{2}T_e = 25$ eV, $\bar{\nu}_i/\nu_e = 9 \times 10^{-2}$, it is found that $p \simeq 10^{-4}$ torr. Figure 19 shows n_g as a function of $\bar{u}$.

The evaluation of $\bar{\nu}_i/\nu_e$ immediately clarifies another facet of the problem. Since $\bar{\nu}_i/\nu_e < 1$

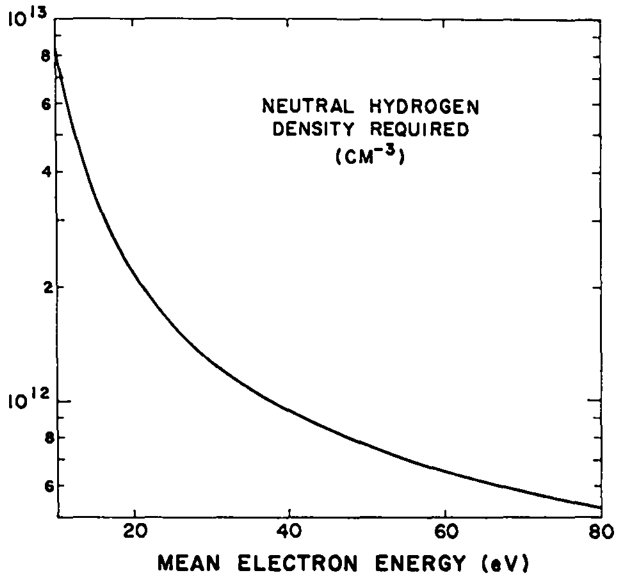

Fig. 19. Neutral gas density vs mean electron energy.

over the entire energy range considered in Table 2, it follows that, for these cases, the average electron will make at least a few and, depending on $\bar{u}$, possibly a large number of elastic collisions with neutrals during its lifetime. Qualitatively speaking it is clear then that such elastic collisions occur frequently enough to insure the high degree of isotropy in f required to avoid instabilities of the anisotropy and loss-cone type even though the electron mean free path may exceed the machine length.

The foregoing arguments have been based upon an ionization rate calculated for a Maxwellian distribution. However, the conclusion about isotropy in f will not be altered by more exact distributions. This is true at low average electron energies, because only the few electrons in the tail of f can ionize, whereas all electrons in the distribution make elastic encounters. For higher average electron energies, such that $\bar{u} \geq u_i$, $\bar{\nu}_i$ should become relatively insensitive to the exact form for f since in this case most electrons in the distribution can ionize. The maintaining pressure given in Eq. (4), on the other hand, can be expected to depend quite sensitively on an exact knowledge of f for low average electron energies.

The energy input u* required to replace an electron lost from the plasma includes the energy required to produce a new ionization and the kinetic energy carried off by the electron. The latter is much more than the average electron kinetic energy since only very energetic electrons can penetrate the sheaths at the ends of the column. If, as indicated above, the sheath reduces the electron current by a factor of the square root of the ratio of electron to ion mass, then the threshold energy for escape is $5.12\ T_e$ in hydrogen where this reduction is a factor of 60.

The average energy of electrons capable of escaping is

$$\int_{5.12\, T_e}^{\infty} u f(u)\, du = 5.50\ T_e. \qquad (5)$$

Therefore

$$u^* = \frac{P_x}{n_e e \bar{\nu}_i} + 5.50\ T_e, \qquad (6)$$

where the power dissipated in inelastic collisions is given by

$$P_x = \int_0^{\infty} e u\, \nu_x(u) f(u)\, du, \qquad (7)$$

assuming that inelastic collisions absorb all of the energy of the incident electron. The form $\nu_x = h_x \nu_e u$ for the excitation rate, with the constant h_x determined empirically,[4] permits integration of Eq. (7) for a Maxwellian distribution. The result is

$$P_x = \frac{5}{4} n_e e h_x \nu_e T_e^2 . \qquad (8)$$

In molecular hydrogen h_x is found to be 5.7×10^{-3}. It includes the effects of vibrational, rotational, and electronic excitation as well as electron ionization. When Eq. (8) is substituted into Eq. (6) the values for u* given in Table 2 and Fig. 20 are obtained. For low $\bar{u}$ inelastic losses dominate u*. For large $\bar{u}$ the contribution to u* is mainly the kinetic energy lost with the electron.

The power required to maintain the plasma in steady state is the product of the electron loss rate and the energy u* lost with each electron. In

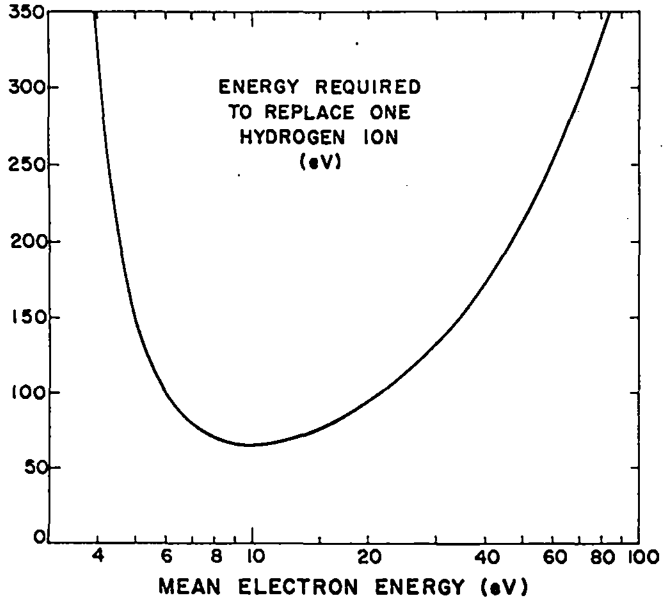

Fig. 20. Energy input required to replace an electron (or hydrogen ion) vs mean electron energy.

hydrogen the latter has a minimum of 66 eV at an average electron energy of about 20 eV (Fig. 20). If the loss rate is dominated by ambipolar streaming out at the ends, then the minimum power requirement is

$$P = \frac{1}{2} n_e \bar{v}_i \, A u^* = (1.7 \times 10^{-11})\, nA \text{ watts},$$

where

$$P \sim \frac{n_e e^2}{m \nu_e} E^2 V.$$

Thus for $\bar{u} = 10$ eV, $n = 10^{12}$ cm^{-3}, and $A = 10$ cm^2, it is expected that ~ 170 W will be required.

As indicated above, these calculations are based upon the use of a Maxwellian distribution function, an assumption which may only be correct when the electron density or ionization degree is large enough for mutual electron encounters to thermalize the distribution. In hydrogen, calculations of f as a function of n_e/n_g are available[5] for average electron energies below about 6 eV with inelastic collisions taken into account. These indicate, as expected, that for a given externally applied electric field and gas pressure (i.e., a given E/p) f tends toward Maxwellian as n_e/n_g is increased.

To investigate the possibility of double-peaked distributions for $\bar{u} \geq 6$ eV, Coulomb encounters have been ignored in the kinetic equations and a solution for f was obtained which is asymptotic in u, but is valid down to $u = \bar{u}$. Its form is

$$f(u) = u^{-\frac{1}{4}} \exp\left[-\left(\frac{h_x}{u_c}\right)^{\frac{1}{2}} u\right] \left\{1 - \frac{3u_c}{32 h_x u^2} + \frac{105 u_c^2}{2048 h_x^2 u^4} + \dots\right\}$$

for $u \geq \bar{u}$, where

$$u_c = \frac{2e}{3m} \left(\frac{E}{\nu_e}\right)^2$$

is the average energy gained by an electron during one mean free time. This asymptotic solution is monotonic in u and leads to the suspicion that the distribution function over the entire energy range is also monotonic since otherwise some evidence of a double peak might reasonably be expected to occur in the range $\bar{u} \leq u \leq \infty$.

It should be noted that this result has been obtained by assuming that inelastic collisions absorb all of the incident energy and that inelastic collision rates increase linearly with electron energy. The inclusion of Coulomb encounters is expected to reduce any tendency to produce second peaks.

In summary, an analysis has been made of the plasma parameters and ECH power required to maintain a plasma column in steady state against end losses. It has been found that the electron velocity distribution will be isotropic in direction and monotonically decreasing with speed in velocity space provided the average electron energy is not too large. Approximate calculations in hydrogen indicate that the upper limit on $\bar{u}$ for these conditions to hold is at least 25 eV, and probably a good deal larger. Numerical computations are necessary to obtain a more precise upper limit.

References

1. G. Lisitano, Proc. Seventh Int. Conf. on Ionization Phenomena in Gases, 1, 464 (1966). ECH experiments utilizing cavity resonators and

very large microwave powers have been carried out for some time by T. Consoli, et al., at Saclay and by R. Dandl, et al., at ORNL.

2. L. Tonks and I. Langmuir, Phys. Rev., 34, 876 (1919).

3. W. P. Allis and S. C. Brown, ibid., 87, 419 (1952).

4. L. S. Frost and A. V. Phelps, ibid., 127, 1621 (1962), A. G. Engelehardt and A. V. Phelps, ibid., 131, 2115 (1963).

5. H. Dreicer, ibid., 117, 343 (1960).

INDUCED RECOMBINATION IN VERY HIGH DENSITY PLASMAS

(H. Dreicer)

Work was recently resumed on the radiative recombination induced by an intense laser beam traversing a very dense plasma.[1] The objective is to determine whether or not this effect influences the formation of plasma by the laser ionization of small solid drops.[2] In the formation of such plasmas, the dielectric and partly transparent drop (density $\approx 5 \times 10^{22}$ cm^{-3}) absorbs some laser light, is heated, and begins to be ionized. As soon as the electron density reaches 2.4×10^{21} cm^{-3} the index of refraction for the laser light becomes imaginary and the laser light fails to penetrate. A short time later, after a small amount of expansion, the density falls below this value, the light penetrates again, more heating takes place and the plasma is fully ionized.

In the standard treatment of the foregoing process[3] the possibility of induced recombination is not recognized. As has been pointed out before, this can lead to a partial deionization of a fully ionized plasma with attendant electron energy losses due to the possibility of ionization. The effect is not easy to calculate, because the induced recombination results in excited atoms whose energy states lie in a region in which the energy levels are completely smeared and merged by Inglis-Teller Stark broadening. The density of states, wave functions, statistical weights, etc., in this range are unknown. Moreover, unless a maximum finite quantum number exists all sums over states diverge. Thus it is necessary to take the depression of the series limit for a hydrogen atom in a plasma into account. Table 3 illustrates the situation for hydrogen by listing the quantum number n_{IT} which gives the start of the Inglis-Teller region, as well as the quantum number n^* which gives the depressed series limit as a function of plasma density. Induced recombination with ruby laser light can occur to all hydrogen energy levels with $n \geq 3$. Thus Table 3 shows that for high densities the Inglis-Teller region plays an important role.

Table 3

N (cm^{-3})	n_{IT}	n*	β(at $\frac{3}{2}$ kT= 144 eV)
10^{16}	9	92	~ 0.010
10^{17}	~ 7	51	0.019
10^{18}	~ 5	29	0.034
10^{19}	~ 4	16	0.063
10^{20}	~ 3	9	0.12
10^{21}	~ 2	5	0.21
10^{22}	1-2	2-3	----

An estimate has been made of the degree of de-ionization β(= excited atom density/electron density) by assuming that the energy levels are unperturbed even in the Inglis-Teller region (see Table 3), but cut off at the depressed series limit. Reionization by electron collision, an important effect, has so far been ignored in the evaluation of β since essentially nothing is known about the validity of using the statistical weights of unperturbed hydrogen energy levels in the Inglis-Teller region.

References

1. H. Dreicer, LA-3628-MS, Status Report of the LASL CTR Program for Period ending Oct. 31, 1966, also H. Dreicer, Bull. Am. Phys. Soc., Ser. II, 12, 761 (1967)(Abstract).

2. Ascoli-Bartoli (Frascati) has produced hydrogen drops, personal communication (1965). A.F. Haught and D.H. Polk, Paper CN-21-110 Proc. II Int. Atomic Energy Conf. Culham (1966). This experiment is performed on lithium hydride particles.

3. J. M. Dawson, Phys. Fluids 7, 981 (1964).

COLUMBA--A HIGH TEMPERATURE Z-PINCH EXPERIMENT

(J.A. Phillips, A.E. Schofield, J.L. Tuck)

Introduction

The purpose of the Columba experiment is to produce for study a z-pinch having a temperature in the thermonuclear (~ 5 keV) region. For reasons not yet clear, these high temperatures have probably not been produced in simple z-pinches although in certain high E_θ θ-pinches[1,2], the achievement of such temperatures is well established. (The plasma concentration phenomenon[2,3] may turn out in fact to be a z-pinch and have a high temperature, but this has yet to be confirmed.) It is further known that θ-pinches at keV temperatures are better behaved and less unstable than at lower temperatures (< 1 keV); this may be due to the effects of (1) high β, (2) finite Larmor radius effects, and (3) suppression of finite resistivity effects. It would be of interest to determine if such favorable effects take place for the more hydromagnetically unstable z-pinch.

In the Columba experiment, the high temperature plasma from a θ-pinch is used as the starting point for a z-pinch. At predetermined times in the θ-pinch cycle the z-pinch is initiated on this plasma and, it is hoped, will confine and further compress the hot plasma. Of immediate concern is the question if the z-pinch will form on the dense hot-plasma core or on low-density plasma outside the central region or remain trapped on the discharge tube wall. This report presents evidence that the z-pinch does not form on the wall but appears to compress the plasma column.

Experimental Apparatus

The θ-pinch is of conventional Scylla design with coil length 28 cm, inside diam 8 cm, and ~ 56 kG peak magnetic field with rise time of 2 μsec. The coil is fed at two diametrically opposite points. The z-pinch, 56-cm spacing between electrodes, is centered along the θ-pinch axis and is energized by two low-inductance capacitor banks in series. Peak currents of 400 kA with a half-period of 16 μsec are obtained. The z-pinch ground return consists of eight insulated

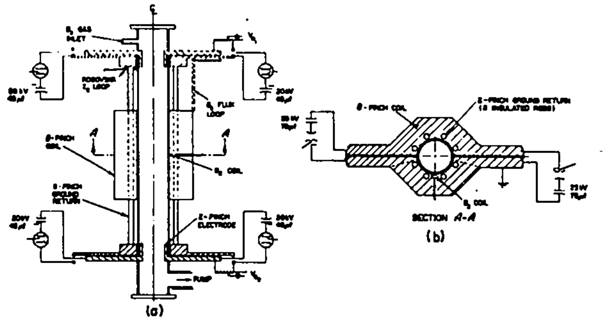

Fig. 21. Schematic of Columba experiment showing θ-pinch coil in z-pinch discharge.

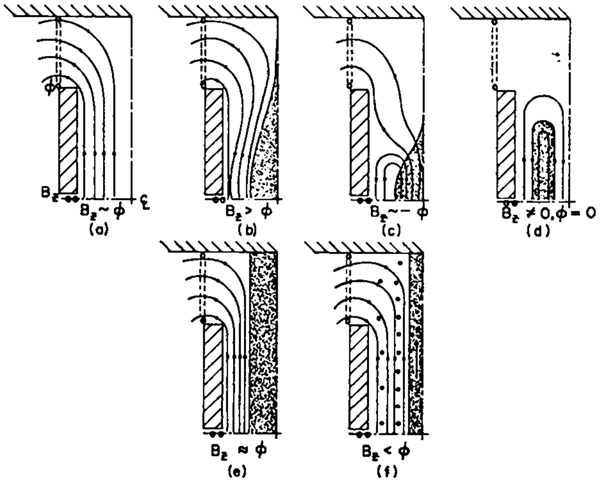

Fig. 22. Idealized B_z magnetic field at midplane and flux (ϕ) escaping from θ-pinch coil. (One quadrant only of the coil is shown.)

1.25-cm copper rods which allow the B_z flux to pass around the θ-pinch coil. (Fig. 21).

Diagnostics on the θ-pinch include two pick-up loops; one of these measures the B_z field at the midplane of the θ-pinch coil and the other measures the flux, ϕ, passing through the coil. The ratio of the signals from these loops, B_z to ϕ, gives a measure of plasma radius as shown in Fig. 22. In Fig. 22a, the ratio of the signals from the two loops is normalized to unity with no plasma. With plasma (Fig. 22b), the B_z field lines at the midplane are compressed in the space between the plasma and the coil and the B_z field is increased so that the ratio B_z/ϕ is > 1. If B_z flux lines are trapped in the plasma and the I_θ current is falling, the B_z field at the midplane may reverse (Fig. 22c), with the flux still positive. Further, the condition can arise that no flux escapes out of the coil with large negative B_z fields at the midplane (Fig. 22d).

Perhaps the case of greatest interest occurs when the z-pinch is applied to the θ-pinch plasma (Figs. 22e and 22f). In Fig. 22e, the B_z/ϕ ratio is again normalized to unity with plasma along the axis. If the B_θ magnetic field from the z-pinch further compresses the plasma, the B_z lines expand, decreasing the B_z field adjacent to the coil for the same flux (Fig. 22f). The ratio B_z/ϕ can therefore be used, with the assumption of azimuthal symmetry, to obtain information on the compression of the plasma column.

From the voltage V_z across the z-pinch and z-current, I_z, together with the assumption of zero resistance, the inductance L of the discharge is given by

$$\frac{\int_0^t V_z dt}{I_z(t)} = L(t) + L_o .$$

With the added assumption of uniform pinch radius between the electrodes, a pinch radius can be calculated.

The total neutron yield is monitored with a standard silver counter, and a fast phosphor-photomultiplier detector gives the time behavior of penetrating radiation.

Results

The behavior of the pinched plasma in Columba when operated at low z-currents (< 100 kA) and with both small and high θ-pinch fields has been reported elsewhere[2] and will only be summarized here.

The z-pinch discharge initially flows along those B_z lines which pass close to the z-pinch electrode. Subsequently the pinch radius expands and contracts due to variations in the magnetic pressure of the θ-pinch field, i.e., the plasma is compressed when the θ-pinch field is a maximum and expands as the B_z field passes through zero.

The results at high θ-pinch fields (~ 50 kG) and peak I_z currents of > 300 kA are shown in

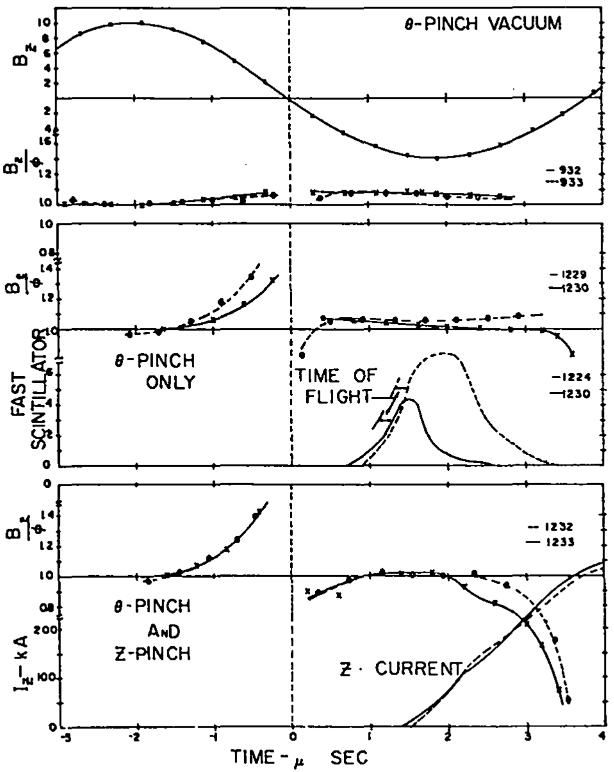

Fig. 23. Characteristics of three types of pinch systems.

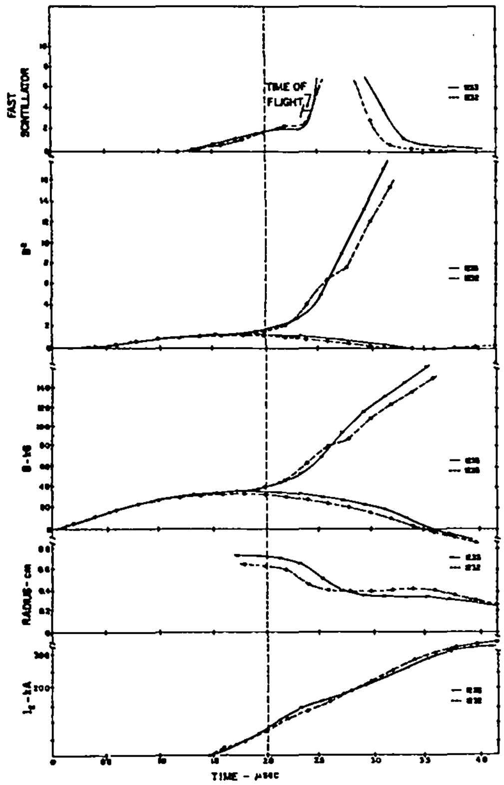

Fig. 24. Behavior of high current z-pinch fired in second half-cycle of a θ-pinch.

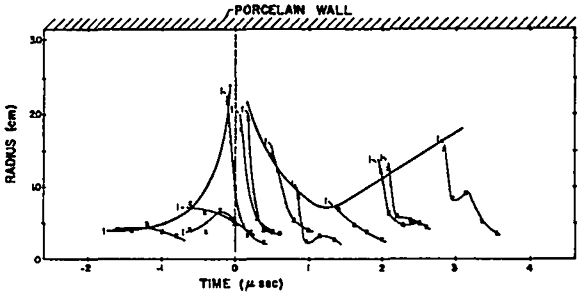

Fig. 25. Calculated initial radius of z-pinch a function of time started in the θ-pinch cycle.

Figs. 23 and 24. The bottom part of Fig. 23 refers to z-pinches fired ~ 1.4 μsec after the start of the second cycle of the θ-pinch. With a θ-pinch in the absence of plasma (Fig. 23 top), the ratio of the B_z field at the midplane to the flux in the coil is constant with time. The ratio B_z/ϕ is subject to exaggerated errors in the vicinity of t ± 0.4 μsec and should be disregarded.

With a θ-pinch and plasma (Fig. 23, center), the B_z/ϕ ratio increases near the end of the first half-cycle, presumably due to plasma heating. (The expanding plasma compresses the B_z field between it and the wall.) The ratio remains fairly constant over the second half-cycle. Two typical neutron pulses are also shown. The times of these signals must be corrected for neutron time of flight to the detector (3.6 m distant).

When z-pinches are fired, 1.2 - 1.4 μsec after the start of the θ-pinch second half-cycle (Fig. 23 bottom), the B_z/ϕ ratio drops as the z-current rises. This is interpreted as a compression of the plasma by the added B_θ-pressure allowing the B_z-field lines between the plasma and θ-pinch coil to expand.

The calculated values of the pinch radius are shown in Fig. 24. The initial radius, ~0.7 cm, is that expected for the θ-pinch plasma and becomes smaller as the z-pinch pressure increases. The calculated total B field and magnetic pressure ($\propto B^2$) at the plasma surface are also given; they are based on the radii assuming B = 1. The efficiency of the z-pinch for producing high magnetic pressures shows up strongly.

The initial radius of the z-pinch is shown in Fig. 25 as a function of the time the z-pinch is initiated in the θ-pinch cycle; time zero is assigned to the end of the first half-cycle of the θ-pinch. The envelope of the initial radii is about that expected for the θ-pinch plasma. Near the end of the first half-cycle the plasma expands to the wall where it contracts to the axis as the θ-pinch field increases in the second half-cycle and is a minimum just before peak field (2 μsec). It is tentatively concluded from these data that the z-pinch forms about the hot θ-pinch plasma.

On some discharges the signals from the fast scintillator detector show a marked increase when the z-pinch current is applied (Fig. 24). This is expected if the z-pinch further compresse the plasma. At the present time, however, two other possibilities have not been ruled out. The z-pinch alone produces neutrons up to ten times that of a θ-pinch and the observed increase may be neutrons produced by z-pinches near the electrodes. Also, on ~ 25% of the discharges, short bursts (≤ 0.2 μsec duration) of hard x-rays have been observed. The fraction of the increase in signal due to these two sources has not yet been determined.

Conclusions

From the data obtained with magnetic loops it appears that a z-pinch applied to the hot plasma from a θ-pinch behaves as expected. Use of a Mach-Zehnder interferometer (see below) should provide further information on this matter.

Mach-Zehnder Interferometer (P. R. Forman, H. J. Karr, J. A. Phillips, A. E. Schofield)

First measurements with the Mach-Zehnder interferometer have been made on the Columba experiment. At full energy the glass end-plates (90 cm from midplane) were found to become opaque on one discharge. This difficulty has been minimized by installing off axis large (36 cm diam) polished plate glass disks immediately in front of the two glass end-plates. The large plates can be rotated and ~ 18 clear surfaces can be successively exposed to the discharge.

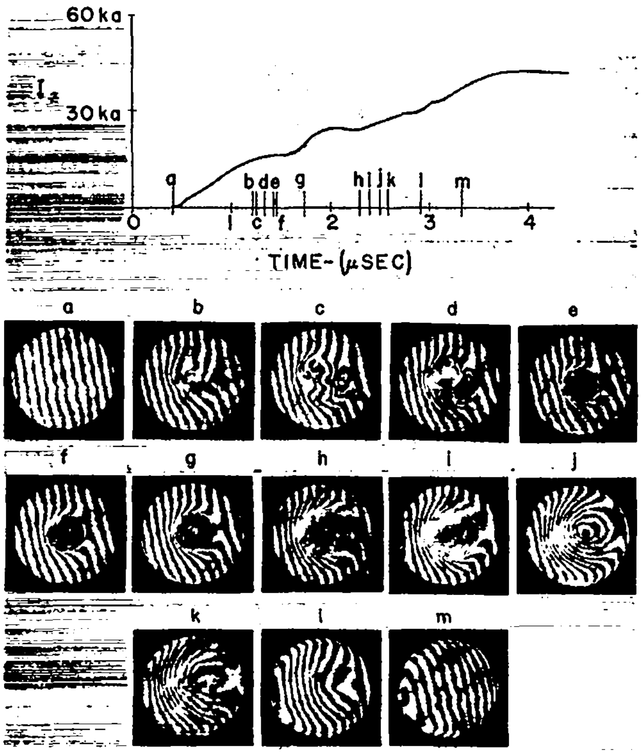

Fig. 26. Mach-Zehnder interferograms from low-energy z-pinch.

A preliminary series of interferograms has been taken on a simple low-energy (10 keV) 200-μ initial D_2 pressure, z-pinch. As this series is perhaps the first axial interferometer pictures ever taken on a z-pinch it is reproduced here (Fig. 26). The times at which the laser was fired in the z-pinch cycle are shown at the top. It will be noted that the discharge current is low, I_z peak ~ 60 kA, with an initial gas filling of 200 μ D_2.

The following rather unexpected observations were made:

1) At early times there is no clear evidence for a current sheath which moves radially inward. Instead, the high-density pinch quickly appears on axis.

2) The fully formed z-pinch has a surprisingly large number of fringes (≤ 20) and has a relatively sharp boundary; there is little evidence for plasma outside of the pinch. Preliminary calculations show that ≥ 90% of the initial gas filling has been swept up.

3) The radius of the pinch increases with time although the z-current is still rising. This is ascribed to fine-grain turbulence or a twisting of the discharge about the tube axis. After ~ 2.5 μsec the effect became so severe as to smear out any significant structure.

At higher z-pinch voltages and currents the time scale is reduced and the duration of a clearly defined z-pinch is less.

References

1. K. Boyer, W. C. Elmore, E. M. Little, W. E. Quinn, and J. L. Tuck, Phys. Rev. 119, 831 (1960).

2. F. C. Jahoda, E. M. Little, W. E. Quinn, F. L. Ribe, and G. A. Sawyer, J. Appl. Phys., 35, 2351 (1964).

3. N. V. Filippov, T. I. Filippova, and V. P. Vinogradov, Nucl. Fusion Suppl. Pt 2, 577 (1962).

4. "Proc. APS Topical Conference on Pulsed High-Density Plasmas," LA-3770, G3-1.

CAULKED STUFFED CUSP EXPERIMENT

(L. C. Burkhardt, J. N. DiMarco, H. J. Karr)

Introduction

The caulked stuffed cusp experiment has developed[1,2] from the earlier cusp and picket fence work carried out at this laboratory. Rapid particle losses with the cusp geometry led to the addition of an azimuthal current at the midplane (caulker), to reduce the losses at the ring cusp by forming a magnetic bridge at this region,and an axial current (stuffer),to minimize the nonadiabatic loss effects caused by the null field region in the simple cusp geometry.

The resulting caulked stuffed cusp is an axisymmetric device designed to study the stabilizing effects of either a minimum-B open system or a minimum average-B closed toroidal system on plasma confinement. The stabilizing effects of the strong magnetic shear contributed by the stuffer component can also be examined. A sectional drawing of the system is shown in Fig. 27. The magnetic field has three components (1) a dc axial field produced by a 180-turn solenoidal winding around the cylindrical vacuum tank, (2) a pulsed field (4×10^{-3} sec half-period) from a four-turn ring or caulking coil at the midplane of the system, and (3) a pulsed stuffer field (4×10^{-3} sec half-period) produced by conductors through the axis of the assembly. The relative amplitudes of the three field components can be varied independently. In this experiment the caulking coil is not levitated. Instead, the mechanical supports for the caulking coil have been magnetically shielded.

Field Configurations in the Caulked Stuffed Cusp System

The first field configuration (Fig. 28) forms a magnetic well that satisfies the minimum-B field stability criteria of J. B. Taylor[3]: (a) the field is nowhere zero so that adiabatic containment is possible, and (b) the magnetic field increases outward from the containment region so that the surfaces of constant $|B|$ form a set of closed nested surfaces about the minimum. Particles

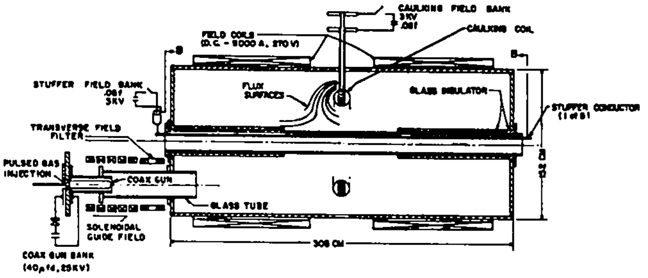

Fig. 27. Schematic section of caulked stuffed cusp system.

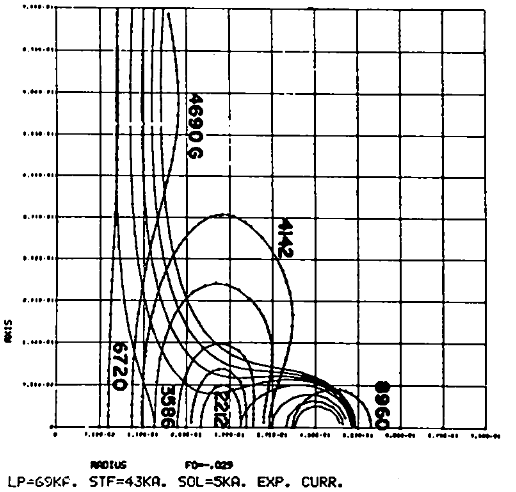

Fig. 28. Quarter section plot of caulked stuffed cusp field configuration satisfying minimum-B requirements. (Solid lines are intercepts of flux surfaces; crossed lines are contours of constant |B|.)

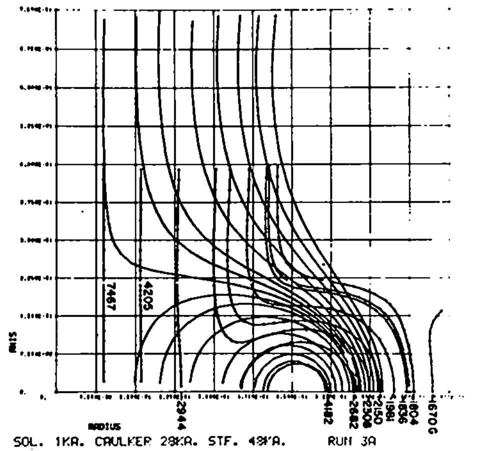

Fig. 29. Same as Fig. 28 but for minimum average-B requirements.

leaving the minimum region encounter a magnetic mirror ratio of 3 in the axial direction and a ratio of 6 along the field lines encircling the caulker. This is an open ended configuration, however, rather than a closed toroidal geometry. The field magnitude in Fig. 28 was obtained for 900 kA-turns solenoid, 276 kA-turns caulker, and 30 kA-turns stuffer.

A closed toroidal field configuration as shown in Fig. 29 is obtained by decreasing the external solenoid field component relative to that of the caulker loop until the stagnation points are moved axially ~ 30 cm from the midplane. This field configuration is similar to that described by Yoshikawa in the proposed "Spherator" device. The field magnitude in Fig. 29 was obtained for 180 kA-turns solenoid, 112 kA-turns caulker, and 301 kA-turns stuffer.

The minimum average-B interchange stability according to the criterion of J. M. Greene and J. L. Johnson[4] is

$$V^{**} = \left(\int \frac{d\ell}{B_p}\right)' - \left(\int \frac{d\ell}{r^2 B_p}\right)' \frac{\displaystyle\int \frac{d\ell}{B_p}}{\displaystyle\int \frac{d\ell}{r^2 B_p} + \frac{1}{R^2 B_\theta^2(R)} \int B_p d\ell} < 0,$$

where r = the distance from the axis, R = radius of the caulker loop, B_p = poloidal field in the r-z plane, and the primed brackets are derivatives with respect to the flux surface $\Psi = 2\pi r A\varphi$. If $V^{**} < 0$, the system is stable against interchange for an infinite wavelength perturbation parallel to B. Without stuffer current, the system is unstable. By increasing the axial current the critical minimum average-B surface can be made coincident with any chosen magnetic surface within the closed field region. Numerical calculations with the CDC 6600 computer give the critical minimum average-B surfaces indicated by the dashed lines in Fig. 30 for axial currents of 48 kA and 32 kA through the seven-turn stuffer toroid. The total stuffer currents are 224 and 346 kA-turns. The resulting closed field containment volume is large ($> 10^5$ cm^3) and combines minimum average-B and magnetic shear stabilization.

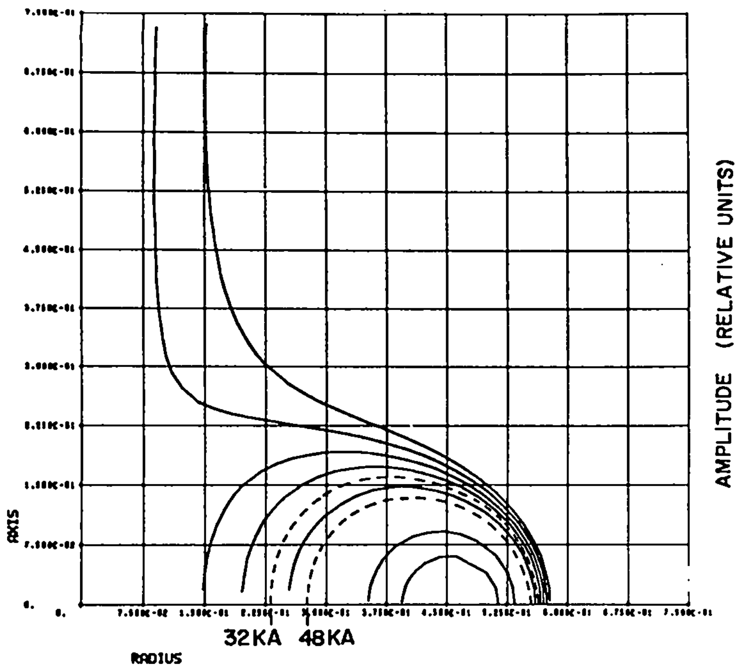

Fig. 30. Quarter section plot of critical flux surfaces of the Greene-Johnson stability criterion.

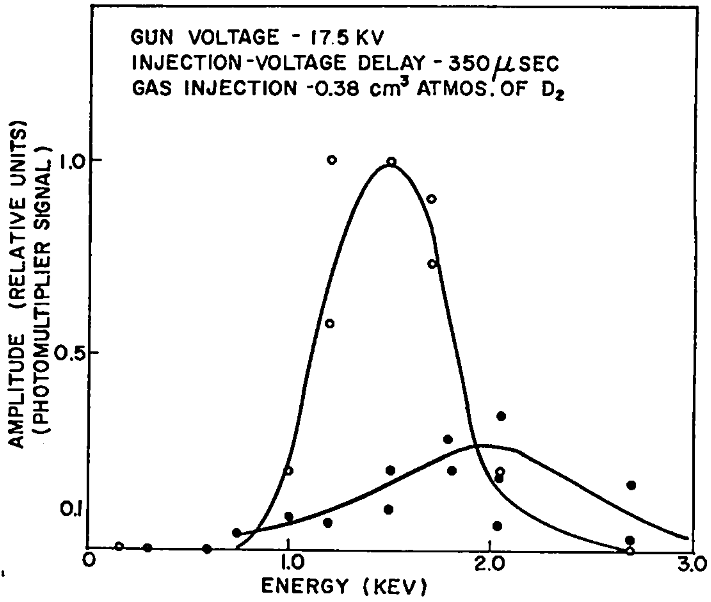

Fig. 31. Energy distribution of "fast" component from coaxial gun. (Upper curve: D energy spectrum; lower curve: impurity spectrum.)

Plasma Generation and Heating

The initial attempts to fill the caulked stuffed cusp device with plasma involved the use of E x B plasma heating using the stuffer and caulker loop as electrodes in the crossed field discharge. This method has the potential advantages of generating the plasma in situ and of controlling plasma energy and density.

There are, however, three apparent limitations: (1) considerable impurities were released from electrodes during the crossed field discharge, (2) experimental observations suggested energy losses due to contact of the plasma with the electrodes and the glass insulators at ends of the system, and (3) breakdown to the supports of the caulker loop occurred despite efforts to shield them magnetically because of the large electric fields required in E xB heating. In view of these limitations, a different approach to filling the system with plasma was used, namely, plasma injection from a coaxial gun. The gun plasma is injected into the closed field region of the confinement volume, where it is expected to be decelerated by the self-depolarization process that has been tested successfully by others. The magnetic shielding of the caulker loop supports against plasma bombardment has been demonstrated by J. E. Hammel and R. M. Henson at LASL to be effective against plasma injected from a coaxial gun.

Experimental Results with Coaxial Gun

The initial experiments have been made with the field geometry of Fig. 29. The objective is to trap the plasma in the closed toroidal field. In these tests, the gun was positioned at one end of the vacuum tank as shown in Fig. 27 and the plasma was injected axially at 36 cm radius (~ 6 cm less than the caulker loop inner radius).

The gun parameters of voltage, amount of gas injection, and delay between gas injection and high voltage application were adjusted to obtain a maximum plasma output at ~ 1.5 keV. The distribution of ion energy as measured with an electrostatic energy analyzer is shown in Fig. 31. This energy is compatible with the magnetic field available for plasma confinement estimated on the basis of ~ 5 ion Larmor orbits in the confinement region. The plasma was observed (with microwaves and Langmuir probes) to propagate from the gun through the peripheral helical field to the closed field region at the midplane of the system where part of it (~ 50%) was trapped and confined.

Plasma Density Measurements

The initial density of the trapped plasma has been determined to be $\sim 5 \times 10^{11}$ cm^{-3} within an order of magnitude from measurements of 3-cm microwave transmission, diamagnetic field changes, saturation ion current to a biased Langmuir probe, current collected with a biased shielded Faraday cup, and the amplitude of the signal obtained with a neutral particle detector. An initial reduction in the amplitude of the microwave transmission signal was produced by the fast plasma component ($\sim$ 1.5 keV) but the density was not quite sufficient to produce cutoff. This gave an order of magnitude estimate of the plasma density of $< 10^{12}$ cm^{-3}. The plasma energy was determined from the plasma transit time over the distance of $\sim$ 350 cm from the coaxial gun to the position of the microwave horns and by comparison with the onset time of signals observed with the neutral particle analyzer which views the same plasma region as the microwave horns. The cold, slower ($<$ 100 eV) plasma from the gun reached the position of the microwave horns $\sim$ 50 μsec after the onset of the fast component. The density of the slower component was sufficient to produce cutoff of the microwaves.

Field changes produced by the diamagnetism of the plasma were measured with a magnetic field probe inserted in the mirror field regions near the caulker and also near the axial stuffer tube. Assuming pressure balance, the average energy density of the plasma can be equated to the change in magnetic field energy density ($2B \times \Delta B \approx \overline{nkT}$). An order of magnitude density was then determined using a value of 1.5 keV for the average energy, which was approximately the peak of the energy distribution of the plasma output from the coaxial gun. This method gave a density of 2×10^{11} cm^{-3}. Order of magnitude agreement ($\sim 5 \times 10^{11}$ cm^{-3}) was also obtained with the probes and the neutral particle detector.

A radial scan through the confinement region was made with a Langmuir probe, biased to collect saturated positive ion current and so provide a measure of the plasma density. The density was found to peak in the vicinity of the minimum of the V** stable well with the maximum occurring in the stable region between the caulker and the stuffer. A small shielded Faraday cup was used to explore the current and density distribution in the confinement region. Probing of the plasma outside the separatrix bounding the confinement volume showed the presence of plasma during injection. As expected, the ion density decayed rapidly in time as compared with that observed within the confinement region inside the separatrix.

Neutral Particle Lifetime

Particle lifetime in the system was studied with the neutral particle detector shown schematically in Fig. 32. In the operation of this device neutral particles formed by charge exchange of ions in the system with the neutral background gas (base pressure $\approx 5 \times 10^{-7}$ mm), pass through collimating slits into the analyzer. A pair of deflection plates remove any charged particles scattered into the detector. The neutral particles enter a gas converter cell (filled with ~ 1 μ of D_2) and are reconverted into ions for energy determination with the 127° electrostatic analyzer. The conversion efficiency is $\sim$ 10% for 1-keV deuterons. Differential pumping maintains a pressure of $\sim 7 \times 10^{-6}$ mm in the collimating tube and analyzer chamber. A Daly detector consisting of an Al block secondary electron emitter and Al coated scintillator and photomultiplier follows the electrostatic analyzer. Ions leaving the analyzer are accelerated by a -20 kV potential applied to the Al block and the secondary electrons are then reflected to the grounded scintillator. The apertures in the electrostatic analyzer are $\sim$ 2.5 cm in width to gain sensitivity at some sacrifice of energy resolution $\sim \pm$ 15%.

Precautions were taken to insure that the signals obtained were not erroneous. With gas removed from the gas converter cell, the signal vanished. This gave assurance that the signals were due to neutral particles rather than to scattered ions or x rays. As a check of the contribution of photomultiplier after-pulses and scintillator after-glow to the observed signals, the analyzer deflection plates were gated with a square wave pulse at selected intervals after the large initial burst and the change in the signal decay time was observed. This technique gave a value

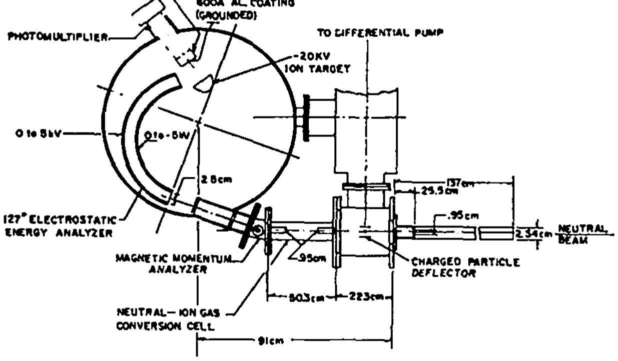

Fig. 32. Neutral particle detector

UPPER TRACE: Neutral particle signal 0.01V/DIV
(4 μsec RC filter in signal line)
LOWER TRACE: Plasma gun current 4 x 10^3A/DIV
OPERATING CONDITIONS: 1.5KA solenoid, 1.5KV caulker,
1.25KV stuffer, 900 eV deuteron,
sweep speed 20 μsec/DIV

Fig. 33. Neutral particle signal. (Solenoid, 370; caulker, 216; stuffer, 115 kA-turns.)

for the scintillator after-glow of 0.5% of the initial amplitude of-the signal and decay times for the scintillator of ~ 50 μsec. Since the amplitude is such a small percentage of the peak signal, after-glow correction to the decay times were not required.

The neutral particle detector incorporates a magnetic moment analyzer in tandem with the 127° electrostatic energy analyzer to eliminate the possible contribution of impurity particles to the observed signals. Tests of the device made by filling the coaxial gun with different gases for plasma injection have shown that hydrogen, deuterium, and nitrogen atoms can be separated and identified.

The neutral particle analyzer was located at a side port of the vacuum tank and the input collimating tube extended through the tank wall to the separatrix. In this position, the analyzer receives neutral particles from a cylindrical section of 2-cm diam along a major radius through the toroidal confinement region extending from the separatrix to the axial caulker tube. The neutral particle detector was placed on the other side of the tank from the coaxial gun.

A typical neutral particle signal is shown in Fig. 33 with the analyzer set to detect 900 ± 135 eV deuterons. (A 4-μsec RC filter was inserted in the signal line to smooth the signal and facilitate lifetime measurements.) The signal decays are shown in the semilogarithmic plots of signal amplitude in Figs. 34 and 35. Figure 34 shows the decay of 900-eV neutral deuterium flux with time for field amplitudes obtained with 180 kA-turns solenoid, 120 kA-turns caulker, and 45 kA-turns stuffer. The e-folding time is ~ 25 μsec. It is of interest to note that the lifetime is independent of density over a range from ~ 10^{11} to 10^9 cm^{-3}. With the higher field magnitudes indicated in Fig. 35, an e-folding time of ~ 110 μsec was observed for the 900-eV deuterium atoms. The results obtained for the dependence of the decay time on field magnitudes are summarized in Fig. 36. In general, the e-folding time increases with the magnitude of the shear field provided by the stuffer.

The neutral particle flux decay time was found to be independent of the neutral particle velocity for low (< 45 kA-turns) values of the stuffer field. At the higher values of stuffer field (> 140 kA-turns) the neutral particle flux decay time had a velocity dependence that was close to 1/v.

Loss Mechanisms

The deuterium lifetime was found to increase with the magnitude of the stuffer and reached a maximum of 110 μsec. This is ~ 1/10 the value predicted on the basis of Bohm diffusion. Since the amount of plasma in the confinement region diminished with increasing stuffer field (and became too tenuous to produce a useful signal in the neutral particle detector), it was not possible to

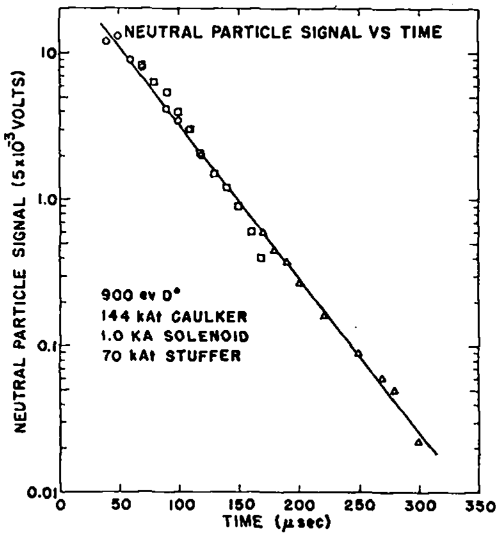

Fig. 34. Neutral particle signal vs time for indicated conditions (kAt = kA-turns).

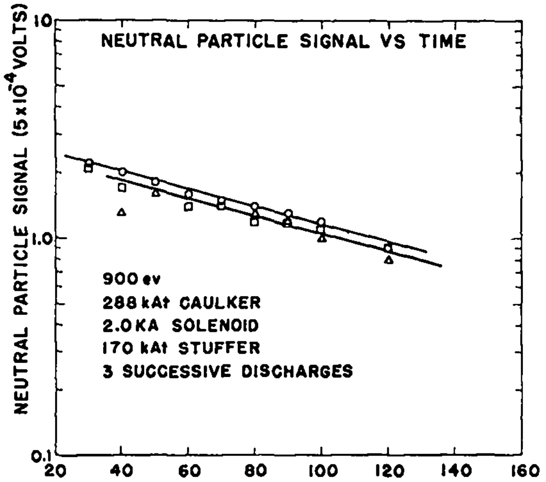

Fig. 35. Neutral particle signal vs time for indicated conditions.

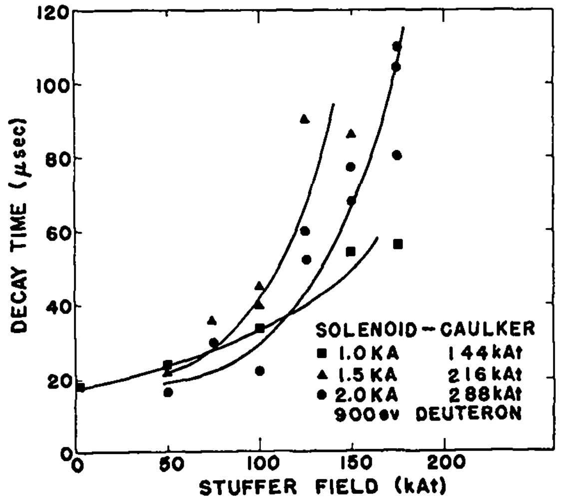

Fig. 36. Decay time of 900-eV neutral deuterium vs stuffer field.

determine if lifetimes > 110 μsec would have been observed with higher stuffer fields. An attempt was made to increase the plasma density in the confinement region by moving the gun in closer; however, the density in the confinement region did not increase enough to permit extending the range of measurements. Modifications in the injection system would be necessary to obtain higher densities at higher magnetic fields. The difficulty is believed to be due to shorting of the plasma polarization field across the insulator at the gun muzzle.

Magnetic shielding of the dipole supports produced no significant change in the lifetime. This result can be interpreted in two ways: (1) The supports are not the primary loss mechanism; therefore, shielding them would not change the lifetime. (2) The magnetic shielding was not effective against particle bombardment. In an attempt to resolve this problem, the effective cross section of the dipoles was increased by a factor of 3.5 with the addition of a barrier around the outer surface of the caulking coil. The barrier did not reduce the lifetime by a factor of 3.5 as would be expected if bombardment of the supports were the primary loss mechanism. Using the value of the observed change in lifetime and assuming that this loss mechanism scales as the area of the bombarded surface, the lifetime for particle bombardment of the dipole surfaces was calculated to be ~ 300 μsec. Therefore, support loss is not the dominant loss mechanism, and this test could not determine the effectiveness of magnetic shielding.

It is not too surprising that the rough calculation of lifetime is off by a factor of three since the assumption made that every particle within the volume has equal access to the dipole is invalid. For example, the mirror ratio should act to reflect some of the particles back into the confinement volume thereby reducing the flux of particles to the supports.

A second particle loss mechanism considered was that due to the stuffer tube surface resulting from the finite size of the Larmor orbit and flux leakage into the surface of the stuffer. Accordingly the stuffer tube was biased

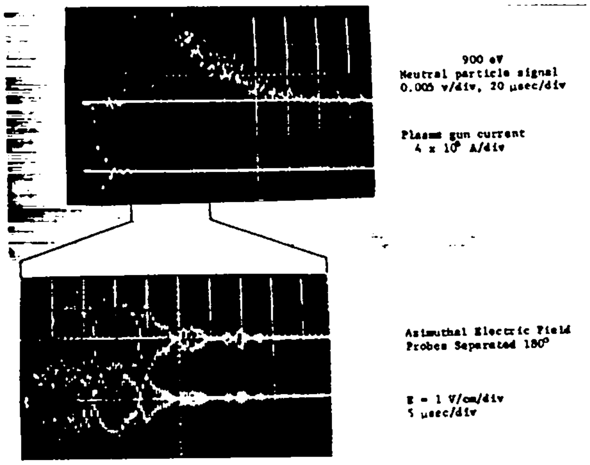

Fig. 37. Time dependence of electric field compared with neutral particle signal.

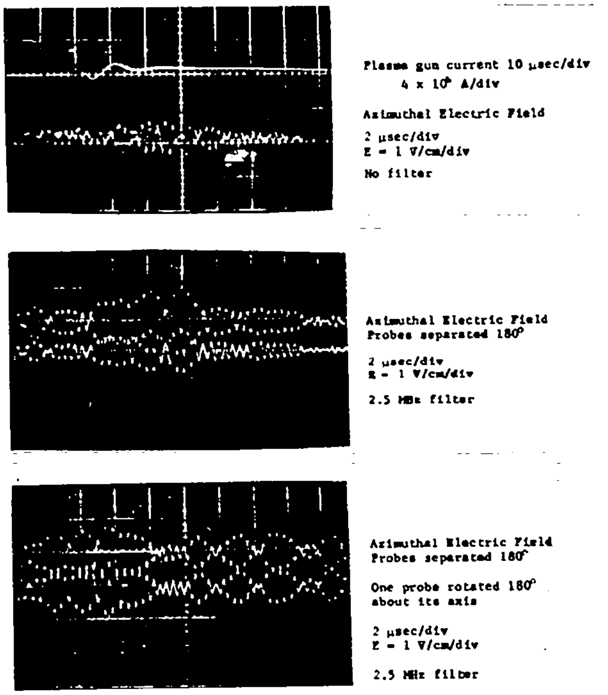

Fig. 38. Electric field signals with and without band pass filter.

to collect saturated positive ion current, and the resulting ion flux into the stuffer surface measured. During the initial plasma injection phase there was a current of 100 mA to 3A, lasting a few μsec, the amplitude depending on the stuffer current. But during the plasma decay period no ion current was observed. The sensitivity of the measurement was limited to a minimum detectable current of a few mA. Ion currents of the order of amperes would be required to account for the observed loss rate.

The confinement region was scanned with electric field probes in an attempt to detect the presence of an instability that might be responsible for the observed loss rate. Large-amplitude electric fields ~ 1 kV/cm were observed furing the initial phase of the injection process. Figure 37 shows the smaller 2.5-MHz oscillations that were observed later during the filling process. The frequency of the oscillation changed only by 5% when the magnetic field was doubled and, therefore, is not a linear function of the ion cyclotron frequency. As one probe was moved in azimuth the fluctuations remained in phase with the signal from a fixed probe indicating an infinite wave length. The amplitude of the electric field decreased rapidly to values too low to account for the observed loss rate, assuming that correlated electric field and density fluctuations resulting in E x B drift losses out of the confinement volume. The electric field signal without the bandpass filter in place is shown in Fig. 38. The 2.5-MHz oscillation is clearly the major frequency component.

Conclusion

On the basis of the foregoing results, it can be stated that high energy (of the order of 1 keV) deuterium plasma has been trapped and confined in the caulked stuffed cusp experiment with lifetimes up to 110 μsec. The loss mechanisms had been postulated to be: (1) loss on the support surfaces of the caulking coil, (2) loss on the surface of the stuffer due to finite Larmor orbit effects, (3) lack of equilibrium due to collective plasma effects, (4) the presence of an instability in the plasma. The experimental evidence eliminated (1) and (2) as the primary loss mechanisms. The observed electric field fluctuations cannot distinguish the loss mechanism as being due to either (3) or (4).

This experiment was terminated as of Sep. 1, 1967.

References

1. C. L. Longmire and J. L. Tuck, Registration of Inventions, Los Alamos, February 1957 (unpublished).

2. J. L. Tuck, Nature 187 863 (1960).

3. J. B. Taylor, Plasma Physics (Trieste Conference 1964) pp. 449, 462.

4. J. L. Johnson and J. M. Greene, MATT-489, Dec. 1966.

PULSED PLASMA GUN PROGRAM

(J. Henins, J. Marshall)

Introduction

The objective of this program is to discover how to build pulsed coaxial plasma guns of greatly increased output. The fundamental difficulty is that, although a coaxial gun is a simple device to construct, it is very complicated in its detailed behavior and is poorly understood. The scaling of guns to higher energy will be very difficult unless there is a much better understanding of the physical processes involved. As dimensions and plasma energies are increased, the mostly empirical development process which is open at present becomes prohibitively expensive and time consuming. It is necessary, therefore, to study and hopefully to understand much better the physical processes taking place in a gun.

During the year covered by this report some rather drastic modifications of the standard gun geometry have been investigated. This was done partly in the hope of finding modifications which would lead to improved performance, and partly with the objective of inducing behavior which through its differences whould shed light on standard gun behavior.

Mushroom IV and V

Two months were spent in completing studies of the "Mushroom" series of experiments (LA-3628-MS, p. 74). Mushroom V, the latest of the series, is shown in Fig. 39. A mushroom hat electrode, fed through a stem surrounded by a cylindrical insulator, takes the place of the usual cylindrical center electrode of the coaxial gun. Gas is injected between the hat and the wall electrode by a fast valve and the capacitor bank is switched across the terminals after an appropriate time for gas distribution. Initial breakdown is along the outside surface of the insulator between the hat and the wall electrode. Thereafter the discharge is driven outward in inverse pinch configuration until it spills over the edge of the hat. Spillover provides an opportunity for the

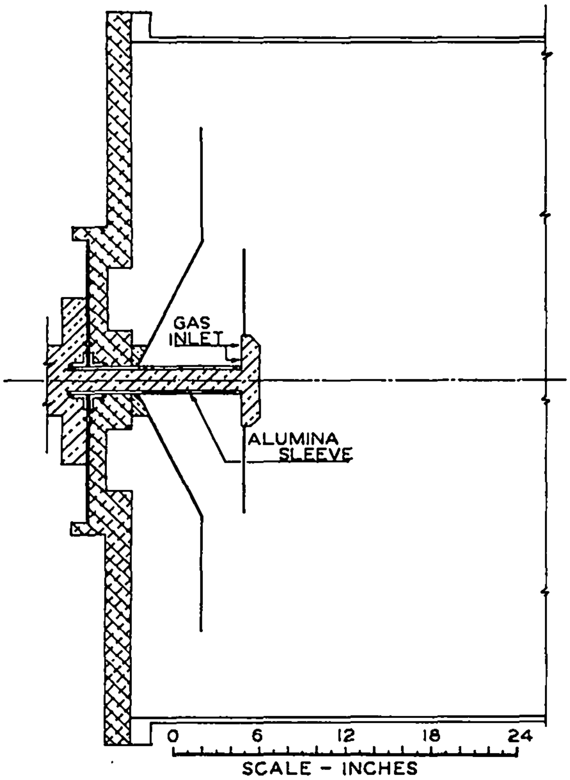

Fig. 39. Cross Section of Mushroom V.

magnetic field trapped between the hat and the wall electrode to expand into the relatively evacuated space beyond the hat. The plasma bounding the field involves only a small mass and the part of it which spills over is greatly expanded in the process. The result is a rapid acceleration of a small amount of plasma with the transfer to it of a large part of the stored field energy.

The inverse pinch geometry is an excellent one for magnetic energy storage, chiefly because it is a poor geometry for accelerating plasma. The plasma is accelerated by the weakest part of a field which falls off as 1/r. It is exceptionally stable in a hydromagnetic sense so that the current sheath would be expected to arrive more or less simultaneously at all points on the periphery. As a gun it suffers from the fault of providing an unpleasantly extended source of fast plasma and of being difficult to fill with gas from a fast valve. The gas escapes rapidly from behind the hat and tends to contaminate the region in front.

Mushroom V represents one of several attempts to limit the escape of injected gas without interfering too seriously with the spillover plasma acceleration process. The conical shape of the wall electrode was arranged to narrow the gap at the edge without extending the hat unduly in the axial direction. Previous modifications of the shape of the more easily variable hat had seemed to indicate trouble in the uniformity of the spillover process, which might have been associated with the hat shape. Mushroom V showed no improvement in behavior over its predecessors, and it appeared that better performance would be achieved only by going to even larger hat diameters and thus more extended source size.

At the time of the previous report there was difficulty in accounting for the neutron yield observed in the region in front of the hat into which plasma was accelerated by the spillover. Measurements made with a fast ion gauge on Mushroom IV indicate much higher gas densities in this region than had been believed previously. It appears now that most of the discrepancy was due to the presence of this background deuterium which contributes to the neutron yield as a target for the fast deuterons of the energetic plasma without increasing the pressure; it thus shows up in magnetic pressure balance computations.

Some attempt was made to improve measurements of the magnetic fields involved in the acceleration of the fast plasma following spillover. The results were hard to interpret because of irreproducibility and it was decided that worthwhile results would require more time and effort than seemed justifiable.

At this point it was decided that.although the Mushroom experiments were interesting in themselves, and had led to a useful plasma source for certain applications, they were probably a side line for the primary purpose of developing a much improved gun for loading thermonuclear plasma machines. One important technical result had been achieved,however. The inverse pinch insulator configuration had turned out to be exceptionally well behaved under high voltage gradients and high gas densities. It was decided to return to a cylindrical inner electrode and to investigate the reasons for the widely different behavior observed in such systems by different workers.

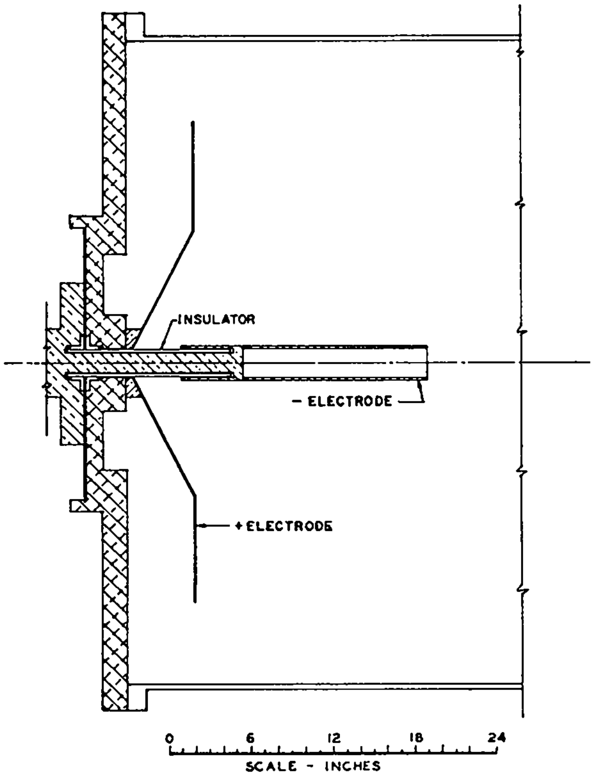

Fig. 40. Cross section of arrangement for Snowplow experiment.

Snowplow Experiments

This series of experiments was motivated by two main considerations: first, that it would provide a means of studying in a clean way the type of current front observed by Mather, et al. in the dense plasma focus device, and second, that it might conceivably provide a superior method of storing energy magnetically beyond the terminals of a gun.

The dense plasma focus had been reported to have a "snowplow" discharge, since B_θ probes inserted along the barrel showed the same fields independent of axial position once the current front had passed. Such behavior was radically different from standard gun mode operation in a very similar geometry. The reasons for this were obscure, but the really major differences between the machines were an inverse pinch insulator (initial breakdown) configuration both in Mather's machine and in the earlier machine of Filippov, et al., and much higher gas density in the plasma focus machines.

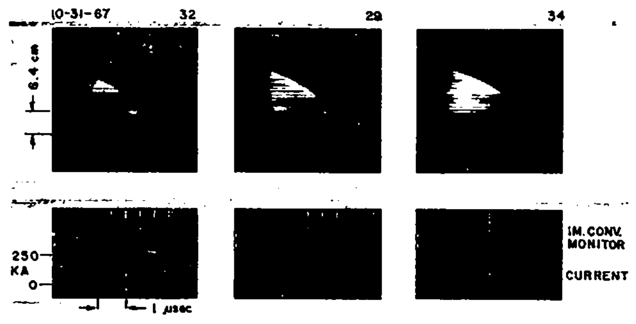

Fig. 41. Image-converter photographs and B_θ-probe signals of Snowplow.

Mushroom V had an inverse pinch insulator configuration at its terminals which was particularly easy to adapt to a plasma focus-type machine. All that was necessary was to replace the mushroom hat with a cylindrical copper electrode and connect whatever outer electrode was desired to the tank wall. It was elected in this case not to install an outer electrode, as shown in Fig. 40, but to use the tank wall for that purpose. This allowed photography and probing experiments without interference by the outer electrode, either in the measurements or in the phenomena being measured. Measurements were made in static fillings of a number of gases over a wide range of pressures.

R. Morse and D. Butler have been investigating theoretically the problem of the plasma dynamics of the dense plasma focus (p. 89). The experiments were designed to check experimentally the shape of the interface between magnetic field and snowplowed plasma, to compare experimental and theoretical velocities, and to measure the current distribution bounding the magnetic field. Shapes were obtained by image converter photography, and velocities by two spaced photomultiplier telescopes. The sharp outer boundary visible in Fig. 41 is not the current front but is a shock wave. The shocked gas behind it is field free for some distance behind the front, and the current layer bounding the bubble of magnetic field is nonluminous as seen through the shocked gas layer. This information comes from measurements with a small B_θ-probe correlated with image converter pictures. There is very little if

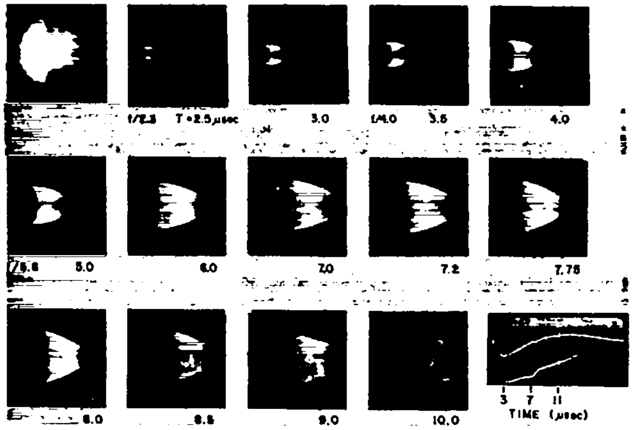

Fig. 42. Image converter photographs of Snowplow in deuterium.

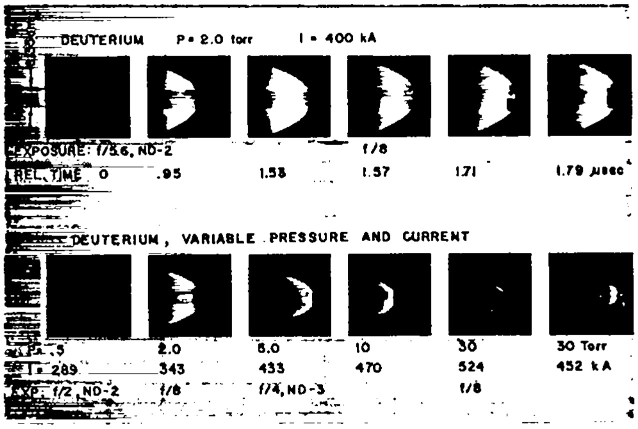

Fig. 43. Image converter photographs of Snowplow in deuterium. (Top: development of pinch; bottom: effects of pressure and current.)

any plasma mixed with the magnetic field inside the current front. When the discharge spills over the end of the electrode to produce a dynamic pinch, as in the dense plasma focus experiment, the rapidly increasing inductance puts a kink in the current as observed with a B_θ-probe or at the terminals of the machine. These two kinks are simultaneous within the accuracy of the measurement; consequently, a very large Alfvén velocity in between and, hence, a very low plasma density must be assumed.

The absence of an outer electrode probably introduces behavior in these experiments which is considerably different from that with an outer electrode. The plasma snowplowed by the bullet-nosed bubble of magnetic field is pushed primarily aside rather than axially. With a solid outer electrode it has no place to go and is simply left stagnated against the wall. This gives it a chance to mix with the magnetic field, apparently a desirable type of behavior in a gun but not in a plasma focus machine. It is noteworthy that Mather, et al., find a perforated outer electrode, or one made of parallel rods, to be superior in a plasma focus machine to a solid electrode.

The end of the electrode has been left open in most of the present studies instead of being closed as in the dense plasma focus experiments. This reduces markedly the amount of electrode light during and after implosion and has allowed photography of an expanding bubble phenomenon following the pinch as seen in Fig. 42. (The photographs were obtained with 10-msec exposures in deuterium; the maximum current was ~ 360 kA.) The calculations of Morse and Butler predict a very similar phenomenon. No probing of the pinch or bubble phases has yet been carried out although plans are being made for measurements of this type.

The simplest description of the behavior of the Snowplow experiment is that it agrees very well with theory; the front moves at a velocity satisfying the stagnation relation, $\rho v^2 = B^2/8\pi$, over a wide range of gas densities and velocities. In detail, however, there are departures from simple behavior. For example, at high gas pressures in H_2 and D_2 (30 to 50 torr) a shredding of the surface parallel to the direction of the current occurs, as shown in Fig. 43. At similar densities, and therefore much lower pressures, in Ar a rippling of the surface at right angles to the current streamlines is observed. Neither of these effects is understood. At quite low pressures in deuterium (the lower left frame in Fig. 43) the front appears to drag behind on the cylindrical electrode (the cathode). This is not understood either but seems to be similar to behavior observed in gun probing reported below.

Some attempt was made to turn the Snowplow experiment into a coaxial gun with improved magnetic energy storage. The idea was to inject gas into a drum-shaped bulge in the outer electrode at the terminal end, allow enough time for a filling gas distribution to be established along the rest of the gun barrel, start operation with a snowplow discharge in the drum, and let the magnetic field energy stored there drive a more-or-less standard gun discharge down the rest of the barrel. No normal gun behavior was obtained with this system, but the reason is not understood. Actually, during the attempt,the fast valve in the system was incapable of injecting as much gas as would have been desirable. Work on the idea may be resumed in the future but for the moment it has been dropped.

Scaled-up Coaxial Gun

In addition to the side-line experiments "Mushroom" and "Snowplow," a considerable amount of work has been done with a coaxial gun. It is fairly obvious that no matter what design changes are made, a gun having greatly increased plasma output will be much larger than the old standard gun.

As a start, the standard gun was scaled up by a factor of two. The resulting gun (Fig. 44) is still of manageable size and its larger dimensions make probing easier and with less perturbation of its performance. The construction is the same as in the standard gun except for the cylindrical inverse pinch insulator arrangement which was retained from the Mushroom and Snowplow experiments. This insulator appears to be capable of operating with higher gas pressures than the pierced disk insulator in the standard gun. The gas load was increased by a factor of eight, and the bank energy was increased to a maximum 48 kJ at 20 kV.

Behavior similar to that of the old gun was indicated by current and voltage waveforms, neutron yield of plasma stagnated against a guide field, and by luminescence of a glass target struck by the fast plasmas shown by time-resolved image converter photography. In addition, some effort was expended with inconclusive results on plasma diamagnetism measurements.

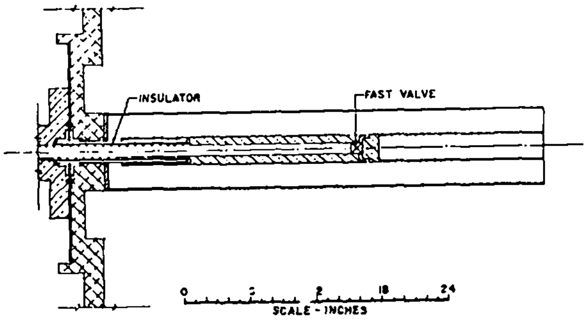

Fig. 44. Cross section of scaled-up gun.

To make these measurements, a 16-in. i.d., 36-in. long, 18-turn bare aluminum solenoid was installed which could be pulsed to produce up to 15-kG axial guide field. The coil was crowbarred at peak field before firing the gun with the solid dielectric metallic contact switch (see p. 43). Then measurements of the coil current changes and of flux changes in two wire loops at two positions inside the coil were attempted with no significant success. Part, at least, of the difficulty results from a flow of energy out through the coil terminals toward the crowbar switch during the measurement. This implies a Poynting vector ($\vec{E} \times \vec{B}$) outward that produced a plasma drift to the terminals and current across the terminals which then obscured the small current variations being measured. These difficulties arose in spite of the very low crowbar switch resistance (< 3.5 μsec at the contact). If the reductance of the crowbarred circuit external to the coil could be increased,so that its L/R time were larger than that of the coil itself, then the plasma drift toward the terminals could be stopped. There are practical problems to this solution, however.

In addition to the foregoing difficulties there may be problems introduced by conduction of electric current from the gun electrodes to the coil through the plasma. Most of these difficulties could have been overcome by the insertion of a glass liner inside the coil but this was not done because it would have amounted to a return to the wall-dominated situation the big vacuum tank was designed to avoid. Instead another problem was taken up, that of probing the discharge inside the gun. To facilitate this the central section of the tank containing the guide field coil was removed.

To study the motion of the discharge down the gun B_θ-probes were placed 90° apart at 10-cm

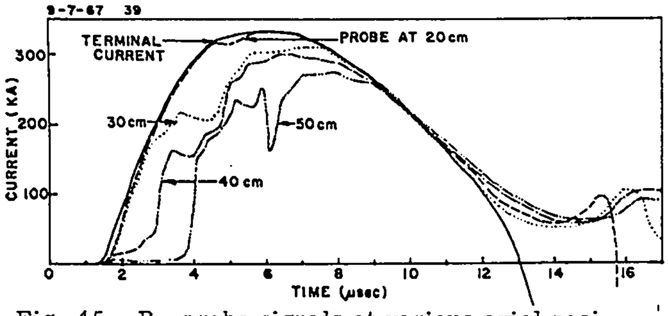

Fig. 45. B_θ-probe signals at various axial positions in gun discharge.

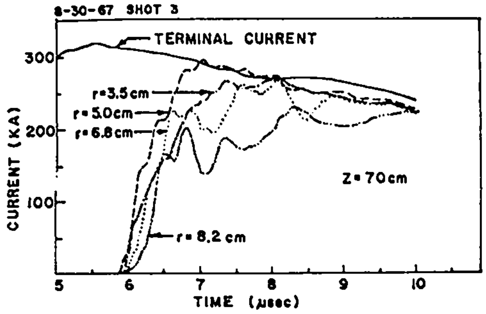

Fig. 46. B_θ-probe signals at various radial positions in gun discharge.

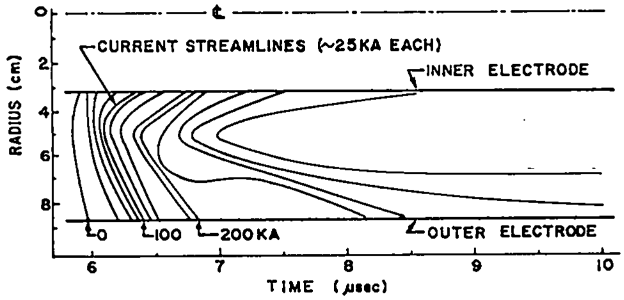

Fig. 47. Smear picture representation of current in gun discharge.
(All data for Figs. 45, 46, and 47 were taken 400 μsec after gas admission.)

intervals along the gun barrel about a third of the way out from the center electrode. Measurements at this radial position were least complicated by the electrode effect as shown by other measurements described below. The probes were calibrated by shorting the gun muzzle and comparing the probe signals to the terminal current.

The probe data in Fig. 45 were obtained with the probes placed 20, 30, 40, and 50 cm from the gun breach (terminal end), and with a 400-μsec firing delay from gas valve opening. It is considered that this delay shows gun behavior most typically. The current plotted is the cylindrically symmetric current inside the probe position which would produce the measured B_θ field. As can be seen, after the initial breakdown the main discharge is immediately localized between 30 and 40 cm and then it progresses both downstream and upstream; it reaches the 30-cm probe at about 3 μsec and later, at ~ 5 μsec, barely touches the 20-cm probe. At still later times the discharge is pushed down the gun barrel and at 9 μsec it is entirely beyond the 50-cm position. This backward motion of the discharge in the early stages may perhaps be responsible for the plasma mixing with the magnetic field, such as is essential for the gun behavior after the plasma reaches the gun muzzle.

In a different type of measurement the probes were placed in the same axial position (70 cm) but at different radial positions. Figure 46 shows data taken with the 400-μsec firing delay. As before, the current plotted is that which, if it were cylindrically symmetrical, would be required to flow inside the radial position of the probe to produce the measured B_θ signal in the probe. A smear picture of current distribution can be obtained by reading the probe signals and placing them at the appropriate radial and temporal positions in a table. With a steady-state system, i.e., a current distribution of constant shape and intensity moving along the system at constant velocity, this would give an accurate spatial representation of the current distribution inside the gun barrel. Current stream lines would be shown by drawing contour lines connecting points of equal current values. In the actual system there is only approximately a steady state. In Fig. 47 contour lines have been drawn for the data of Fig. 46 with a correction for the varying terminal current. The stream lines appear to drag on both electrodes. This indicates that plasma has been pushed aside so as to stagnate against the electrodes, reducing the magnetic field there diamagnetically. At later times, farther back from the front this diamagnetism decreases, perhaps because of mixing of field and plasma. At longer firing delays, or with static gas filling at higher pressures, the dragging (stagnation) on the inner electrode is much reduced while more of it appears against the outer electrode. The drag on the center electrode was also observed at low pressures in the Snowplow experiments.

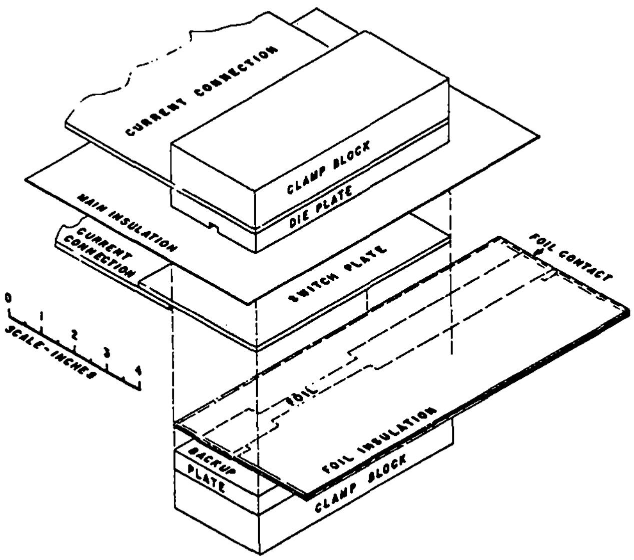

Fig. 48. Isometric view of switch configuration.

The Solid Dielectric Crowbar Switch

The switch used to crowbar the bare B_z field coil is basically the same as reported in LA-3434-MS. Modifications have been made to adapt it to the present application, and further performance tests have been run. The current return is no longer folded around the exploding foil.because at the present lower current values magnetic forces are not necessary to keep the switch closed. Also, ½-in. thick aluminum plates are used for the die plate and a backup plate to absorb the immediate shock of the foil explosion and to keep from damaging the steel clamp blocks. The present switch configuration is shown in Fig. 48.

The switch cartridge is assembled with contact cement to hold the parts in alignment. The cartridge is inserted in a clamp, which in the present case is a 30-ton hydraulic press, to hold the switch together during the explosion. The total applied pressure is usually ~ 20 tons. Automatic closing of the clamp also makes contact to the switch and the foil terminals. The cartridge is disposable and a new one is inserted for each shot. The cost of materials for each cartridge is ~ 85¢, and ~ 10 min of labor per cartridge is necessary to fabricate the parts in quantity and to assemble the switch. In some cases, when jitter is not important, some of the switch parts can be reused, thus reducing the cost slightly.

The width of the 0.002 x 0.375 x 3.0-in. exploding copper foil is slightly larger than the 0.250-in. width of the groove in the die plate. This minimizes the effect on the closing time of slight misalignment of the foil and the groove. Approximately 3 kJ of electrical energy at high voltage and low inductance is necessary to explode the foil satisfactorily. This is provided by a 20-kV, 14-μF capacitor with ignitron switching. The insulation around the foil is one layer of 0.005-in. Mylar plus one layer of 0.010-in. polyethylene. The Mylar is necessary because, at the clamping pressures used, straight polyethylene extrudes slightly, sometimes ripping the foil.

The driven contact plate is 0.125-in. thick annealed 1110 (i.e., nearly pure) aluminum. Without annealing the normally half-hard aluminum does not extrude properly. A thinner plate could be used which would allow the switch to close faster and with less foil energy. This would, however, decrease the energy that the switch could absorb. The main insulation between the switch plates must be of adequate thickness and extend far enough past the edges to withstand the applied voltage prior to switch closing. Polyethylene, 0.030-in. thick extending ~ 1½ in. past the edges, has been used for this purpose.

The die plate is 0.5 x 2.5 x 6.0-in. plate of 6061-T6 aluminum. A longitudinal 0.25-in. wide and 0.140-in. deep contact groove is cut into it. In the bottom of the groove is placed a 0.031-in. thick strip of perforated metal. The punched-out insulation is extruded into the perforations and provides a dissipative mechanism for the energy of the driven aluminum. In tests in which the insulation and aluminum hit the solid bottom of the groove, an apparent bounce occurred, sometimes tending to spoil the switch contact.

The switch described above closes in 10.13 ± 0.31 μsec after the current from the 14-μF capacitor, charged to 21 kV, is first applied to the foil. Figure 49 shows the closing time distribution of 25 carefully controlled shots. The change in closing time with capacitor voltage is given in Fig. 50. Oscillograms of the foil current and the voltage across the switch during operation are shown in Fig. 51; A is the voltage across the switch contacts

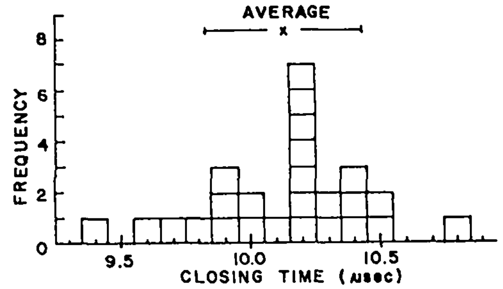

Fig. 49. Histogram of closing times for 25 shots.

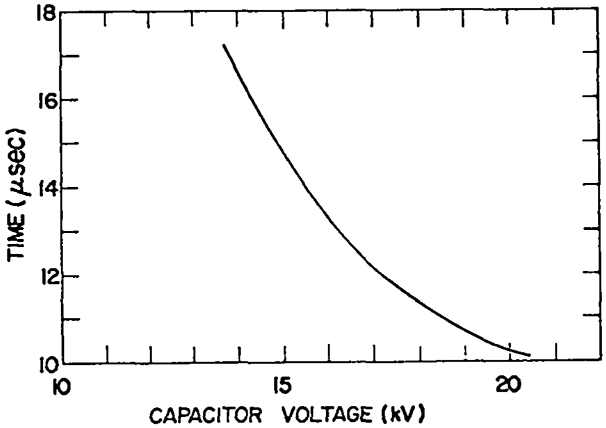

Fig. 50. Switch closing time vs capacitor voltage.

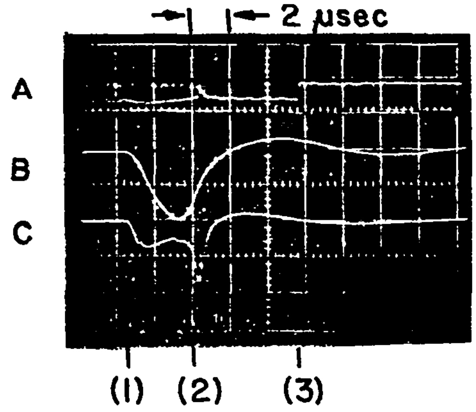

Fig. 51. Oscillograms of switch voltages and current (see text for details).

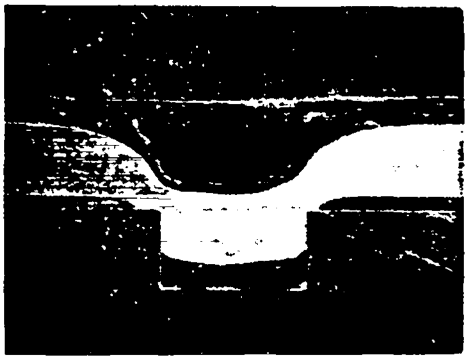

Fig. 52. Cross section of switch after closing.

during closure (1 kV/div.), B is the exploding foil current (83 kA/div.), and C is the voltage across the exploding foil (10 kV/div.). The times indicated are (1) ignitron breakdown, (2) foil explosion, and (3) switch closure. A cross section photograph of the switch contacts after closing is given in Fig. 52.

In the present application the switch crowbars a 50-µH magnetic field coil at the time it carries approximately 40 kA of current. After closing the L/R time is 45 msec. From measurements of voltage across the switch and the current after closing, switch resistance is calculated to be 2 µΩ.

The inductance of the switch is low and therefore difficult to measure. For fast current rise times (2 to 5 µsec) L is estimated to be $< 0.5 \times 10^{-9}$ H. This estimate is based on treating the switch as a coaxial conductor of 0.03-in. length with the inner conductor perimeter approximately the same length as the switch contact perimeter, and the outer conductor perimeter approximately as long as the perimeter of the edge of the switch plates.

The ampere-second load that the switch will withstand before destruction is dependent on the heat capacity of the aluminum in the contact region and on the heat conduction away from this region. The heat input is proportional to I^2R and to the current duration. Particularly if the skin effect is considered, the relationship of the variables is too complicated for simple calculation and experimental tests of the maximum switch capability would be better. Unfortunately, at the present, a convenient means to push the switch to this limit is not available.

DESIGN STUDY OF A QUADRUPOLE DEVICE WITH INNER CURRENT CONDUCTORS FED THROUGH MAGNETICALLY SHIELDED SUPPORTS

(D.A. Baker, J.E. Hammel, L. W. Mann)

In 1964 a design study was undertaken[1,2,3] for a caulked cusp-type confinement of plasma at high energy and temperature. The device was to have two inductively-fed, free-fall inner rings. The quadrupole was chosen so that the forces on the rings could be counteracted by hoop stress alone. The design goal for this machine was a containment time of 50 msec for 10-keV deuterium plasma. A computer study showed that in order to satisfy design constraints either cryogenic cooling of the conducting rings or unsuitably high field energies and large dimensions were required.

The present machine design represents a less ambitious first step in containing high-energy plasma in a toroidal quadrupole device. The construction of the present device is greatly simplified for the following reasons: (1) Free-fall rings have been abandoned in favor of mechanical supports which will be magnetically shielded. (2) The confinement will be studied for a much shorter time, ~ 1 msec. (3) The energy of the plasma to be contained has been lowered a factor of four (2.5-keV deuterons). (4) The number of gyro-radii of stable field has been reduced from ten to the maximum number obtainable subject to the other constraints on the machine. This device will have another advantage over the free-fall inductively-fed machine; the magnetically-guarded current feeds allow ohmic E-fields to be shielded thereby removing associated $\vec{E} \times \vec{B}$ plasma drift.

A sketch of the machine is given in Fig. 53. This figure is shown without the electrostatic shields around the rings. Figure 54 is a sketch of the U-shaped current conductor that will be used to produce the dipole guard field for shielding the coaxial feed conductors and supports. In the actual machine one dipole arrangement will be fastened at the top of each conductor and will feed the current and support the rings. The field configuration (end-on view) produced by a pair of infinitely long line currents inversed in a uniform field B_o

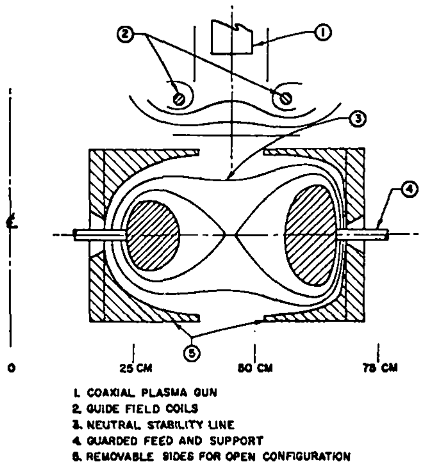

Fig. 53. Schematic of quadrupole device.

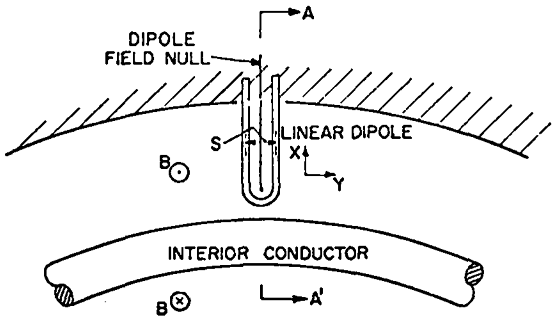

Fig. 54. U-shaped linear dipole guard conductor.

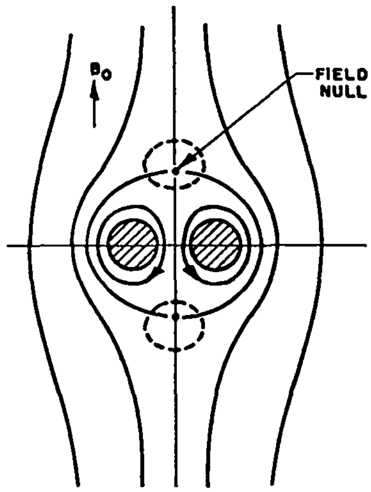

Fig. 55. Field configuration of dipole of infinite length for force-free condition.

is represented in Fig. 55. The location of the line nulls, which run parallel to the currents, are shown for the force-free condition. Previous experiments[4] have shown that the guard currents effectively shield the dipole from an incident plasma stream.

The dipole currents produce two approximate null lines which are parallel to the currents. Plasma will enter this region[4] and move along the null line. If the dipole legs go straight into the inner conductor, the null line will also go to the inner conductor. Plasma will thus be in contact with the inner conductor at these points. To prevent this contact it is essential to have the null line close before it reaches the inner surface. The closing of the null is accomplished by making the dipole a hairpin with the "U" placed just above the inner surface. A study of the dipole shield problem is reported in the next section of this report (p.48).

The geometric configuration of the quadrupole itself was designed using an IBM 7030 computer code. The problem was one of maximizing the number of gyro-radii in a $\int d\ell/B$ stable region by varying the geometry (ring separation and size, torus radius, and outer toroidal boundary location) subject to the following constraints: (1) Field at the injection point ≤ 10 kG. Present plasma guns will not penetrate higher fields. This field value should be as high as possible to allow only the most energetic plasma to enter the machine. (2) Maximum field ≤ 40 kG. This restriction is based on the strength of materials and is particularly critical for the dipole. (3) Single mirror bridges. It seems inadvisable to put multiple mirrors in a bridge which may trap plasma and which would possibly promote instability. (4) Total field energy < 1.7 MJ. This is the energy readily available to the experimental area. (5) Equal current in both conductors allowing series feed, and also equal flux linking each conductor allowing the option of parallel operation. Insulation space limitations in the series operation will require that the capacitor bank be electrically floated. Although the parallel operation does not suffer from this difficulty, the field period is cut in half. This flexibility in design will permit a choice of the optimum method.

The computer code used in the design was prepared with the help of M. MacRoberts (T Division LASL); it is analogous to the one written by R. A. Dory at the University of Wisconsin. The system has rotational symmetry about the z-axis of a cylindrical coordinate system and the currents in the rings have only azimuthal components; these conditions make it convenient to use the vector potential which also has only azimuthal components.

By applying Maxwell's equations to the interior region and assuming infinite conductivity for the boundary, it follows that

$$\nabla^2 \vec{A} = 0,$$

where $\vec{A}$ is the vector potential. By making the substitution

$$\psi = rA_\theta,$$

the result in cylindrical coordinates is

$$\frac{\partial^2\psi}{\partial r^2} - \frac{1}{r}\frac{\partial\psi}{\partial r} + \frac{\partial^2\psi}{\partial z^2} = 0.$$

This substitution has the advantage that it eliminates one term from the differential equation and then the ψ = constant boundary condition can be specified for perfect conductors since $2\pi\psi$ is the flux.

The differential equation is solved numerically using the Extrapolated-Liebmann Method of Successive Over Relaxation. The relaxation parameter is recalculated every 12th iteration by a method developed by Carré.[5] Once the flux value has been found at up to 7000 mesh points, the quantities of interest in the design of the device can be calculated.

The magnetic field B is computed from the definition of $\vec{A}$

$$\vec{B} = \nabla \times \vec{A}$$

giving

$$B_r = -\frac{1}{r}\frac{\partial\psi}{\partial z}$$

$$B_z = \frac{1}{r}\frac{\partial\psi}{\partial r}\ .$$

The current is obtained by computing $\oint B d\ell$ along a line of constant flux. The region of low-β interchange stability is defined by the Longmire-Rosenbluth $\oint d\ell/B$ criterion. Stability is implied if the line integral taken over closed-field lines decreases away from the separatrix. The number of gyro-radii in the device is calculated at the outer bridge where it is a minimum. The gyro-radii are approximated by the amount of stable flux divided by the mean radius of the outer bridge. Values obtained from the computer program are scaled to the 10-kG injection field to yield the design parameters.[6]

Figure 56 shows the geometry designed to meet the criterion on p. 46. The energy in the stable field is 0.5 MJ. If an open geometry is used, so that the vacuum vessel is the outer conductor, the energy requirement becomes ~ 1.1 MJ. The design in Fig. 56 gives 7.0 gyro-radii at the outer bridge. The inner rings shown may be made smaller in cross section for weight and construction purposes; this will also add flux between the separatrix and the rings.

The problem involved nonlinear programming and no way has been found to apply standard techniques; consequently, there is no guarantee that the solution obtained is optimum. It is the best, however, that has been found in about 50 different configurations. The results for a simple case have been checked against an analytical solution obtained by D. A. Baker and J. Freidberg (at LASL) for linear quadrupoles. The problems of strength of materials have not all been solved and it is probable that the design criteria may have to be relaxed somewhat further.

When constructed, this device should give data on the dipole shield effectiveness, on the depolarization trapping of energetic plasma streams in quadrupoles, and, if all goes well, on the validity of the $\int d\ell/B$ stability criterion for plasmas of high density and temperature.

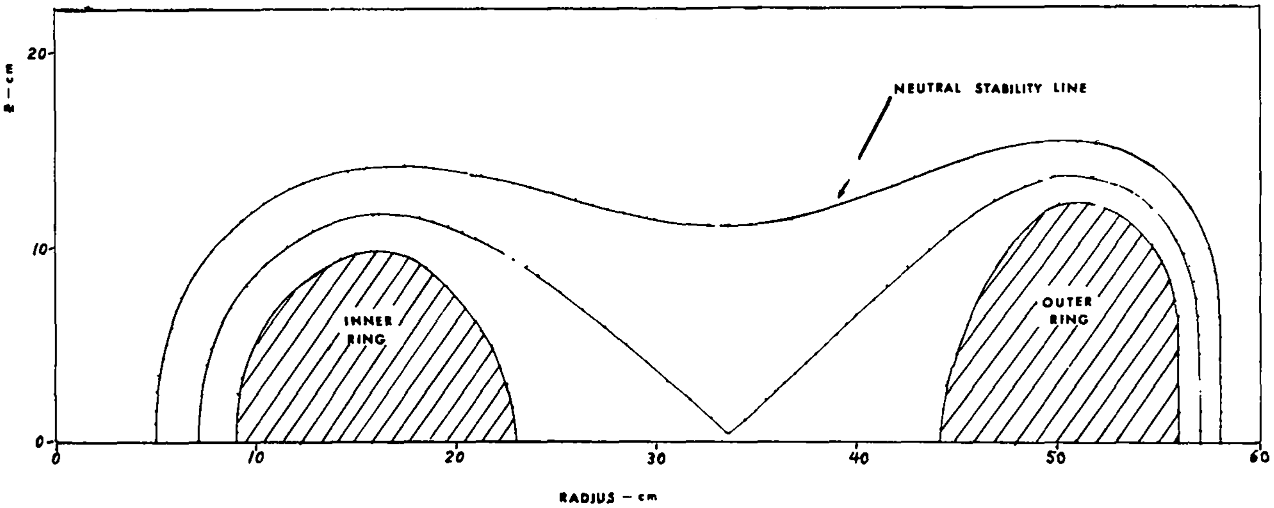

Fig. 56. Geometry of inner conductors and associated flux (for design meeting criterion in text).

References

1. D.A. Baker, L.W. Mann, and J. Marshall, LA-3202-MS, LA-3320-MS, LA-3253-MS, and LA-3628-MS.
2. D. A. Baker and L. W. Mann, Bull. Am. Phys. Soc., Ser. 2, 11 550 (1966) (Abstract).
3. J. Marshall, D. A. Baker, and I. Henins, ibid., Ser. 2, 11 550 (1966)(Abstract).
4. J.E. Hammel and R. M. Henson, ibid., Ser. 2, 12 799 (1967)(Abstract), and LA-3628-MS.
5. B.A. Carré, Computer Journal 4, No. 1, 73 (1961).
6. The scaling laws are described in LA-3320-MS.

DIPOLE FIELD STUDIES

(J.E. Hammel, D.A. Baker,
R.W. Kewish, L.W. Mann)

Introduction

A hairpin guard current is needed at the quadrupole leads of the device described in the preceding section. A study of the field produced by such a hairpin of current has proceeded along two lines: (a) the measurement of the field produced by a mockup, and (b) computer calculations for a thin-wire hairpin.

The experimental approach is required since no computer codes exist which will solve the pulsed field problem for an actual geometry that is needed. Although the computer calculation uses thin current filaments, the results give a useful insight regarding the topology of the field lines and minima.

Computer Calculations

The field plot for a thin-wire hairpin current in a uniform background field B_o is shown in Fig. 57. The parameters were again chosen to approximate the force-free condition

$$B_o = I/10d,$$

where B_o is in gauss, I in amps, and the conductor spacing 2d is in cm. The dipole spacing is 2 cm and the crossfeed is located 1 cm above a perfectly conducting image plane. The loci of the field minima are dotted and field values are spelled out at various locations for the case $B_o = 100$ G and I = 1 kA. The results show the expected closing of the field minimum (null) line as the image plane is approached. The minimum field at the image plane is depressed only a small amount from the value of the background field.

Measured Fields

A mockup of an actual dipole was constructed and located within a large pair of Helmholtz coils and above a conducting sheet to represent the background field of a quadrupole bridge. The system was energized by ac with a frequency (1 kHz) near that expected for the quadrupole experiment. The material of the dipole was thick compared to the skin depth. A representation of the measured magnetic field in the plane of the null lines is shown in Fig. 58. The arrows represent the magnetic field in both relative magnitude and direction. The dipole currents were chosen to give a force-free configuration for a dipole of infinite length.

Model Studies

Further studies of the dipole guard have been made to answer some of the questions concerning field configurations with respect to flux tubes around the dipole and cross-bar for a mechanical design of the dipole, within the constraints of required current and conductor size.

Probe studies in the plane of the nulls show that the dipole designed for the 2-m quadrupole will effectively close the null before the inner ring is reached. Probe measurements off the null plane show field directions which would be indicated by flux surfaces shown in Fig. 59.

Flux Conserver

A copper flux-conserver will cover the two turn coils and conform to the ring shape shown in Fig. 56. A mockup of the two turns and the flux conserver was made for the feed region. It was found that the bumpiness produced by the turns was not detectable when the flux conserver had a thickness greater than one skin depth.

Dipole Design

Dipole Current Source

Two methods of providing current to the dipoles are series connections with the main coil, or independent drive from a transformer. The transformer designed to drive a dipole was tested with a dipole as a load. The test was not encouraging in that the transformer would need considerable mechanical improvement to be reliable in a machine. This difficulty and the advantages of the series drive have dictated a series design for the machine. There is now less freedom for the size and spacing of the dipole legs since the current can no longer be chosen independently.

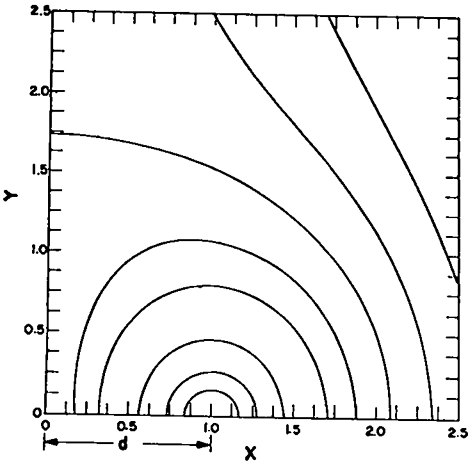

Fig. 57. Field line plots in plane defined by field nulls in Fig. 55.

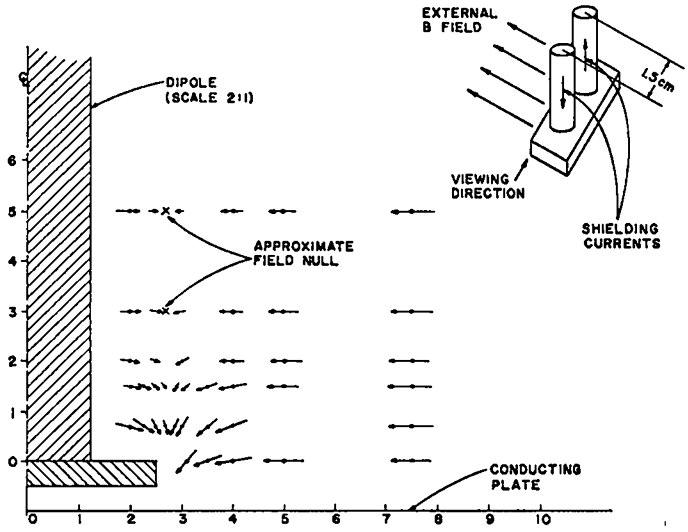

Fig. 58. Observed magnetic field in plane of the null lines.

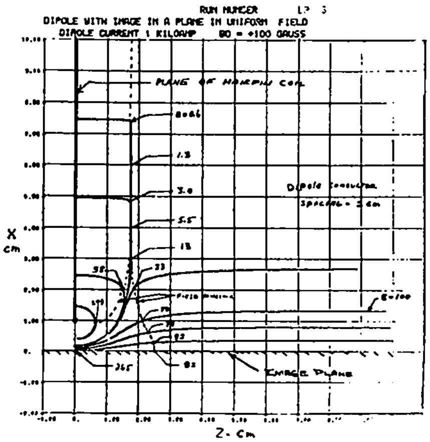

Fig. 59. Flux surfaces from probe measurements off the null plane.

Dipole Size

With the current and magnetic field given by the quadrupole design, the maximum diameter of the dipole legs is limited by the number of gyro-radii needed between the null and the conductor surface. The size and spacing of the dipole legs are found by matching the conductor to flux surfaces (approximately right circular cylinders) given by the vector potential, A_z, for two straight wires in a background field, B_o. With the line currents adjusted to be force-free, the vector potential is

$$A_z = -\frac{\mu_o i}{4\pi d}\, x + \frac{\mu_o i}{2\pi}\, \ln \left[\frac{(d+x)^2+y^2}{(d-x)^2+y^2}\right]^{\frac{1}{2}},$$

where 2d = separation of the line currents.

One quadrant of A is plotted in Fig. 59, with the current at (1,0). A field null is at $(0, \sqrt{3})$. The number of gyro-radii between the null and a flux surface is the same as the number between the origin and the same surface and is given by

$$\lambda = \int_o^x \frac{dx}{\rho(B)} = \frac{1}{2.10^{-4}\sqrt{W}} \int_o^x B(x,0)dx$$

(W = deuteron energy eV).

or

$$\lambda = \frac{1}{2.10^{-4}\sqrt{W}}\, A_z(x,0)$$

and

$$\rho(B) = \frac{mv}{eB}.$$

For W = 2.5-keV deuterons and $i = 500 \times 10^3$ A,

$$\lambda = 5\left(-\frac{x}{d} + 2\ln\frac{1+x/d}{1-x/d}\right).$$

For λ to match the number of gyro-radii across the quadrupole, the maximum leg diameter is ~ 1.3 cm, if the original machine parameters were maintained.

Because of this very small leg diameter, calculations have now been made for a quadrupole which is 2 m across. It is found that with this larger diameter the original machine parameters can be maintained with much lower fields in the bridge. This increases the dipole diameter to 2.85 cm and makes a series dipole feed feasible. The configuration with the larger diameter requires a new tank rather than a reworking of the present tank.

Force on the Dipole

In the dipole field studies it is shown that a large field is present beneath the dipole crossbar. A pulsed high-current model of this region was made with the aim being to measure the magnitude of the force on the crossbar. The force was to be measured with a PZT ferroelectric transducer mounted in a ceramic sonic line. The shielding of the high-impedance transducer, when it is placed on the dipole bridge, was found to be difficult. The measurement was not completed successfully and the force is now being estimated from magnetic field measurements on the 1-kHz model.

TRANSVERSE INJECTION EXPERIMENT FOR LOADING A MAGNETIC FIELD

(J.E. Hammel, R. W. Kewish)

Introduction

Since a Marshall gun produces a deuterium plasma which has the density and energy in the thermonuclear range, it is of importance to determine experimentally if such a plasma can be injected and held in magnetic geometries. The technique of transverse injection into a magnetic field gives two possible means of loading a field. These depend on depolarization of the polarized transverse stream by (a) self-depolarization of one stream along reentrant field lines that cross the stream twice, or (b) by the interaction of one stream on an oppositely-directed stream. In addition to the information on loading of magnetic geometry, these experiments will be useful in observation on the polarization field interactions.

The two opposing streams are a possible technique for loading toroidal geometries with azimuthal fields. The self-depolarization technique requires a geometry with reentrant field lines over a short distance such as multipoles with little or no shear.

Two Opposing Guns

An experiment with two opposing guns is being performed in a geometry shown in Fig. 60. The two guns are not directly opposed but are offset (55 cm) along the field direction. From

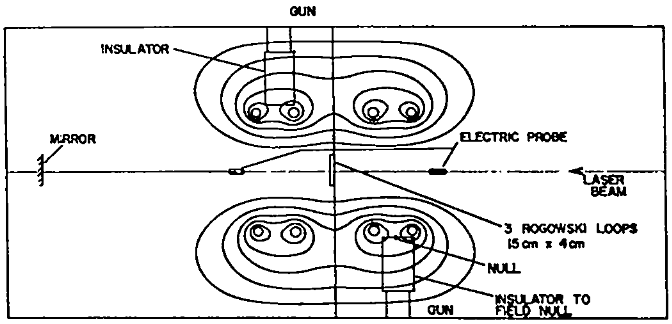

Fig. 60. Field plot in experiment with two opposing guns.

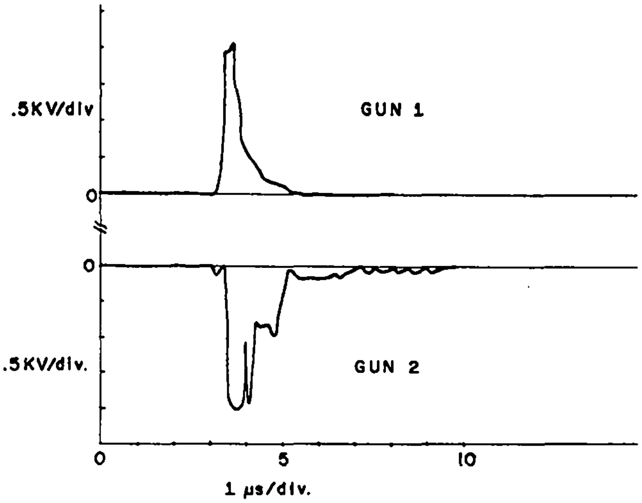

Fig. 61. Electric field signals from single gun.

previous measurements on streams entering a shorted region of a transverse field[1] it can be predicted that two streams directly opposed would interact to give a deflection of one from the other while remaining transverse to B. This direct encounter would not leave an appreciable amount of plasma in the field.

If the streams are offset along the field direction, the depolarization currents will be delayed by inductive effects until the streams pass each other and a more complicated and efficient depolarization and trapping is possible. The characteristic time for this current under very simplifying assumptions is

$$\tau = \rho v w L/B^2 h, \qquad (1)$$

where ρ = density of the streams before the encounter, w = stream dimensions along B, h = height of the stream, and L = inductance of the current path assumed time independent. τ is adjusted through L (function of offset) and B to the same magnitude as the transit time of the stream across a large portion of the diameter of the field. Past experiments indicate that an offset of a few 10's of cm is about right for kilogauss fields.

Density and Electric Field for Single Stream

Three features of the plasma are measured in the experiment by methods which do not place objects directly into the plasma stream. The electric field orthogonal to v and B is measured by probe pairs placed outside the coils as seen in Fig. 60. A usual electric probe signal is shown for each gun fired separately (Fig. 61). The impedance of the electric probe pairs must be $> 1000\ \Omega$ if the far probe signal is not to be noticeably degraded. This value is probably set by the density of the plasma which connects the plasma stream to the probe. An estimate from the required probe impedance gives a density of $\sim 10^{11}$ cm^{-3} for the connecting plasma. The majority of the signal appears on two probe pairs; this gives a stream height of about 5 cm. The peak signal makes an $E/B = 60 \times 10^7$ cm/sec.

The density of the plasma is determined by a laser interferometer[2] operating at 3.39 μ. The peak cross-sectional density for each stream alone is 0.1 to 0.2 fringe (3×10^{15} cm^{-2}).

Density, Electric Field, and Current with Two Streams

Description of Experiment

The experiment requires that both streams intersect the same flux tube near the axis of the magnetic field. The streams are quite narrow (5 cm) at high B values and a small refraction by the transverse field caused the streams to miss. By mounting one gun in a bellows and allowing a movement of the gun direction, the intersection is controlled within the variation in the stream direction. When the two guns are fired, the current flowing between the two streams is measured by three Rogowsky loops placed midway between the streams; their positions relative to the plasma guns are shown in Fig. 60. The currents through the loops and the electric fields are dependent upon the displacement in time and the ratio of the energy density of the two streams.

Streams Simultaneous in Time and Equal Energy Density

When the two streams are simultaneous within the arrival time jitter of $\sim 0.2\ \mu$sec and are of similar denergy density, the electric field probes gave signals which oscillated rapidly between nearly peak field values of the two streams. The two gun E-field shown in Fig. 62 may be compared with that of a single gun in Fig. 61. The currents in the Rogowsky loops are

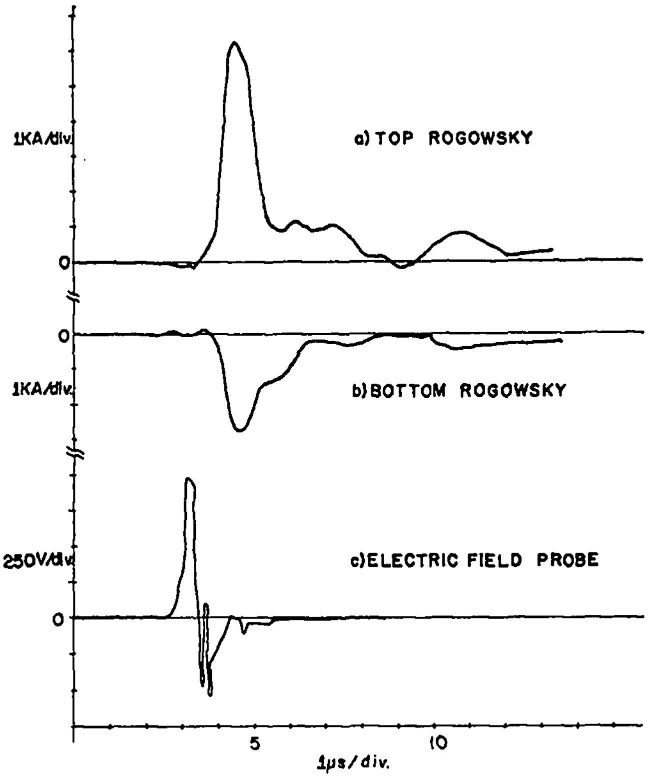

Fig. 62. Rogowsky coil currents and electric field for two-gun system.

given in Fig. 62; the peak currents are seen to be > 6 kA. The top and bottom loop currents are not symmetric since exact placement of the loops with respect to the stream is impossible. The current is of the magnitude which would halt the streams when the known stream parameters are put into the equation of the momentum flow

$$nmv^2 = \frac{I \cdot B}{wk} \, , \qquad (2)$$

where k = 1 is assumed if the streams are halted and not reflected.

An important feature of the current trace is that it is nonoscillatory and appears to be heavily damped. Since classically the collisionless plasma would not cause such a damping, the energy might be dissipated through instability and turbulence. D. A. Baker (of LASL) has suggested that an expansion of the current loop path might have the appearance of damping. However, by Eq. (2), damping even at high B_0, when the depolarization currents are not large, makes this explanation seem less likely. The cross-sectional density measured by the laser interferometer gives a general idea as to density of plasma involved in this experiment. The former is about 0.1 to 0.2 fringe at 3.39 μ (~ 3 x 10^{15} cm^{-2}). The shot-to-shot variation in signal is rather large, primarily due to the angular variation in the direction of the narrow streams. This makes it difficult to measure the increased density caused by the two-stream interaction. Also, the solenoid magnetic field is not a bottle which would contain a large buildup of density. On certain favorable shots the increase in density is many times the density of the single stream. One such example is seen in Fig. 62A.

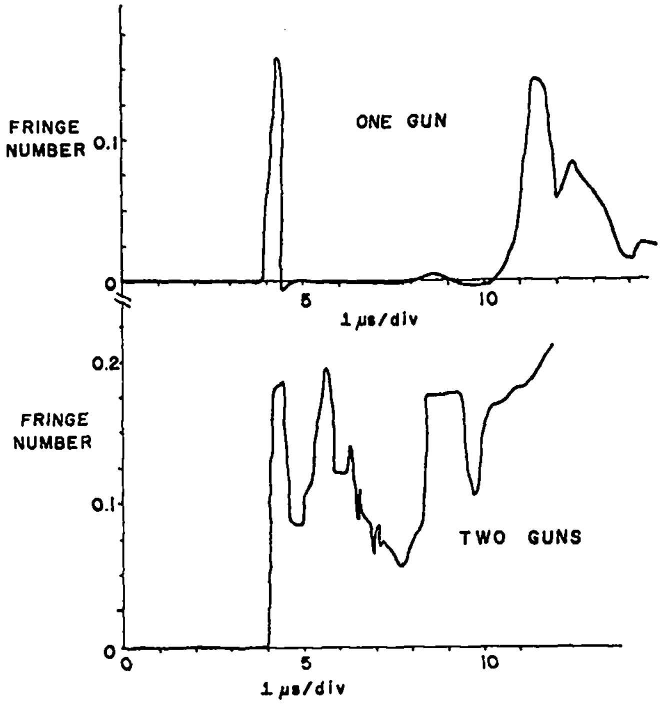

Fig. 62A. Laser interferometer measurements for one and two guns.

Streams Simultaneous in Time but Unequal Density

If both streams arrive at the same time but are greatly unequal (factor of two or more) in density, the high-density stream completely dominates the E-field. The dominant stream sweeps up the low-density stream with it. Current measurements for this case have not yet been made.

Equal Streams Displaced Slightly in Time

When timing of the two guns is not simultaneous but is within 2 μsec, E-field characteristics of both guns are present in sequence. Further investigation will be made of the current and E-field for this case.

Streams Greatly Displaced in Time

A tenuous background plasma was placed in the magnetic field prior to the arrival of one stream by firing one gun at low voltage very early, by > 6 μsec. Even with the density of the background plasma less than 0.02 fringe, the normal density stream will not enter the field to a detectable level. This is most surprising since, from the simple momentum transfer point of view, the dense fast stream should easily pick up the background gas and enter the transverse field. The low-density background must have some large effect as the stream tries to enter the field. It is planned to investigate this point using F. Jahoda's moiré pattern technique (p. 86).

Conclusion

Simultaneous streams of equal energy density show a large interaction, with measured currents being of the right magnitude to stop the streams. A damping mechanism is present which could put a large part of the energy into the plasma (a form of turbulent heating). Further investigation of the currents and electric fields in various combinations of timing and density is needed to clarify the disposition of the plasma and energy after the encounter.

References

1. D.A. Baker and J.E. Hammel, Phys. Fluids, 8, 713 (1965).
2. J. E. Hammel and D.L. Rode, LA-3730.

FARADAY ROTATION MEASUREMENTS ON THE SCYLLA IV THETA-PINCH

(R. F. Gribble, E.M. Little, W.E. Quinn)

Introduction

A measurement of the Faraday rotation of a plane polarized wave propagating through a plasma-magnetic field medium can be used to determine the integral of the product of the magnetic field and plasma density over the length of the medium. Such rotation measurements have been performed on plasmas in small theta-pinch devices, using either the 3.39-μ radiation[1,2] or the 6328 Å emission[3] of a gas laser. At 3.39 μ, the measurement is difficult because of refractive effects ($\propto \lambda^2$) of the plasma, combined with extremely nonuniform sensitivity over the small active surface area of the InAs infrared detectors. The use of 6328 Å radiation reduces this limitation because of the λ^2 dependence of the plasma refractive effects and the much greater area, sensitivity, and uniformity of response of detectors available in the visible region. A disadvantage of the use of the shorter wavelength is reduced sensitivity because of the λ^2 dependence of the Faraday rotation.

Faraday rotation measurements with 6328 Å radiation have been combined with Mach-Zehnder interferometer observations to determine the average magnetic field as a function of radius in the plasma of the Scylla IV θ-pinch.[4] These measurements also give (a) the average plasma β, i.e., the ratio of plasma pressure to external magnetic field pressure, as a function of radius, (b) the plasma density, and (c) with the assumption of a simple pressure balance between plasma and magnetic field, the "perpendicular plasma temperature," $T_{\perp}$.

Method

The Faraday rotation measurement employs the visible radiation (6328 Å) from a He-Ne gas laser as a plasmamagnetic field probe. The plane of polarization of the laser beam, propagating parallel (or antiparallel) to the magnetic field in the plasma region, rotates through an angle

$$\theta_R = 1.5 \times 10^{-15} \lambda^2 \int_0^L B_i n_e d\ell \text{ (degrees)}, \qquad (1)$$

where B_i is the magnetic field (gauss), n_e the plasma electron density (cm^{-3}), L the plasma length (cm), and λ the wavelength of the laser beam (cm). With the direction of propagation parallel (antiparallel) to that of the magnetic field, the plane of polarization rotates clockwise (counterclockwise) as viewed in the direction of propagation. Since the Faraday rotation is proportional to $\int B_i(\ell)n_e(\ell)d\ell$ and the Mach-Zehnder interferometer provides $\int n_e(\ell)d\ell$, the determination of B_i from the combined measurements assumes that

$$\int B_i(\ell)n_e(\ell)d\ell = \bar{B}_i(r)\int n_e(\ell)d\ell, \qquad (2)$$

and that this $\bar{B}_i(r)$ is the magnetic field which exists over the major portion of the plasma length at the radius r. In the long compression coil of Scylla IV, this assumption is reasonably good. At worst, the measurement can give only an apparently higher average value of B_i than exists in the main plasma region. With initial reversed bias magnetic fields, the rotation could conceivably reverse direction if the trapped reversed field persisted into the compression phase of the discharge during which the Faraday rotation measurement is made.

With a laser beam of 1.5-mm diam and with fast detectors and wide band amplifier, θ_R can be measured as a function both of space (radius) and time. A series of interferograms taken on the same discharge provides a time- and space-resolved measurement of $\int n_e d\ell$.

These measurements of B_i can be combined with that of the external magnetic field B_e to determine the average plasma β as a function of radius,

$$\beta = 1 - B_i^2/B_e^2. \qquad (3)$$

The measurements can also be used to obtain the plasma temperature at a given radius, averaged over the length of the plasma, from pressure balance with the magnetic field; thus,

$$k(T_e + T_i)_\perp = \frac{1}{8\pi n}(B_e - B_i) = \frac{\beta}{n}\,\frac{B_e^2}{8\pi}, \qquad (4)$$

where B_e is the external magnetic field and it is assumed that $n_e = n_i = n$.

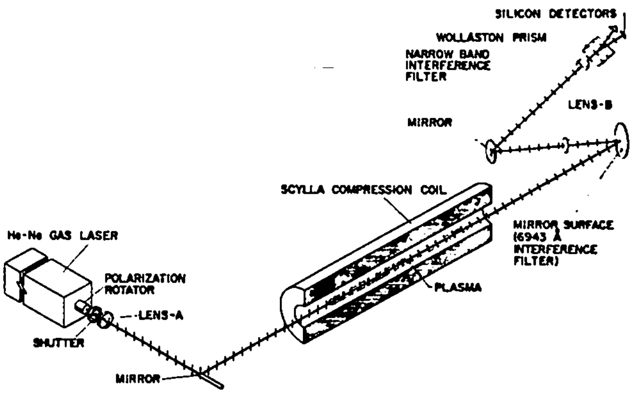

Fig. 63. Schematic diagram of experimental arrangement.

Experimental Arrangement

A schematic diagram of the Faraday-rotation experimental arrangement is shown in Fig. 63. A 70-MW He-Ne gas laser at 6328 Å sends a plane-polarized light beam through the plasma region parallel to the axis of the 1-m length, 10.2-cm diam compression coil, into a polarization analyzer, and onto a pair of silicon detectors. In order to accommodate the Mach-Zehnder interferometer on the machine simultaneously with the Faraday arrangement, the Faraday beam probe is turned through 90° by a small mirror between the Mach-Zehnder mirror and the end of the coil. As the Faraday beam leaves the coil, it is reflected out of the interferometer's path by the tilted Mach-Zehnder filter. Two narrow-band interference filters in series, with transmissions peaked at 6328 Å serve to reject the plasma light as well as the 6943 Å laser light of the interferometer. The polarization analyzer consists of a 13° calcite Wollaston prism which splits the plane-polarized laser beam into two perpendicular components of polarization. The Wollaston prism deviates the components by 13° in opposite directions, giving a 26° separation between them. The prism is positioned so that in the absence of plasma the plane of polarization of the laser beam is 45° with respect to that of the prism components in order that the two will have equal intensity.

The silicon detectors consist of a selected, matched pair of photoconductive detectors with 20-V/W sensitivity, a measured rise time of 0.1 μsec, and a measured variation in sensitivity over the 0.7-cm diam active area of less than 2%. Each detector monitors one component of the laser beam. A wide band, high-common-mode rejection ratio, integrated amplifier provides a difference signal from the two detectors. Two other integrated circuit amplifiers, with the same gain as the differential amplifier, are each connected to a detector to obtain individual detector signals as well as a sum signal. The Faraday rotation is proportional to the ratio of the difference to the equivalent sum of the detector signals after amplification.

The resolution of the Faraday-rotation measurement is determined by the signal-to-noise ratio of the laser-electronic system and by the almost completely unpredictable effects of the beam refraction by transverse electron density gradients in the plasma. The signal-to-noise ratio limitation is determined by the laser power and the 3-mV peak-to-peak noise at the differential amplifier output. Assuming an incident power of 40 mW on the calcite Wollaston prism, this noise results in a minimum resolvable signal, for equal signal and peak-to-peak noise, of 10^{-3} deg. of rotation. With 23-mW incident on the prism, the minimum resolvable rotation is 4×10^{-3} deg., which corresponds to a minimum resolvable product of internal magnetic field B_i in kG and electron density n'_e in number of 6943 Å Mach-Zehnder fringes of 2.3 (kG)(fringes). Each fringe corresponds to an integrated density of 3.2×10^{17} cm^{-2}. With the plasma length and densities in the Scylla IV device, this corresponds to a magnetic field limit of ~ 0.3 kG, which is 0.3% of the maximum compression field.

Radial profile data of B_i and β were obtained by scanning the radial dimension of the plasma shot-by-shot with the 1.5-mm diam laser beam. About six discharges were taken for each radial position of the laser beam, which was moved in 2-mm increments. Since the plasma column moves a few millimeters in the radial direction during a given discharge, the data are analyzed and averaged according to the measured position of the laser beam relative to the axis of the plasma. Optical systems with image-converter cameras record the Mach-Zehnder interferograms with time resolutions of 50 nsec and provide four interferograms at selected times during the discharge.

Results

Faraday-rotation measurements were performed in the low-pressure plasma regime with initial filling pressures of 10, 15, and 25 mtorr and with magnetic bias fields of 0, -1.2, and -2.4 kG. Measurements were made at 1.4, 2.4, 3.4, and 4.4 μsec after the application of the main magnetic field ($T/4 = 3.7$ μsec). Radial profiles of B_i, β, n_e, and $T_\perp$ are shown in Figs. 64 and 65 for an initial filling pressure of 15 mtorr and with initial bias fields of zero and -1.2 kG. The error bars of the plots represent the average deviations from discharge to discharge. The graphs of Fig. 66 compare the radial plasma β profiles at different times during the discharge. In both cases, with and without B_o, the β profiles are relatively flat in the central plasma region during the earlier portion of the discharge (~ 1.4 μsec). Without B_o, the β profile becomes more triangular as time progresses, with the value of β on the axis remaining high. With B_o, the profiles also decrease in radial extent, but possess a more parabolic shape. It is of interest that the radial extent of the β profiles increases slightly after the magnetic field maximum, indicating some radial expansion of the plasma as the magnetic field decreases.

In the low-pressure plasma regime (10-25 mtorr) the β values in the central plasma core (~ 5-mm diam) range between 0.9 and 1.0 with initial reversed bias fields and values between 0.7 and 0.95 without bias fields. In general β increases with increasing filling pressures (10 to 25 mtorr) and with increasing negative bias fields. For example, with 25 mtorr initial deuterium filling pressure and a negative bias of 2.4 kG, β remains greater than 0.95 for 4.4 μsec. There is a good correlation between

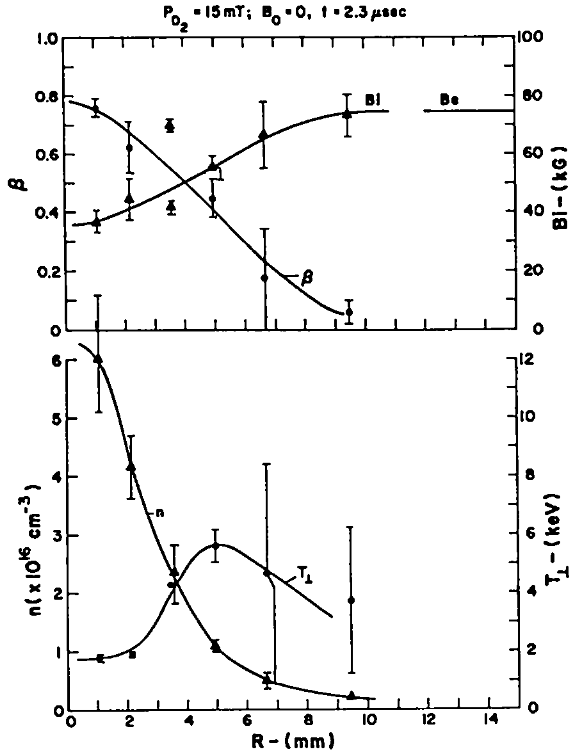

Fig. 64. Radial profile plots of B_i and β (upper) and n and $T_\perp$ (lower) vs radius at 2.3 μsec after beginning of discharge; bias field zero.

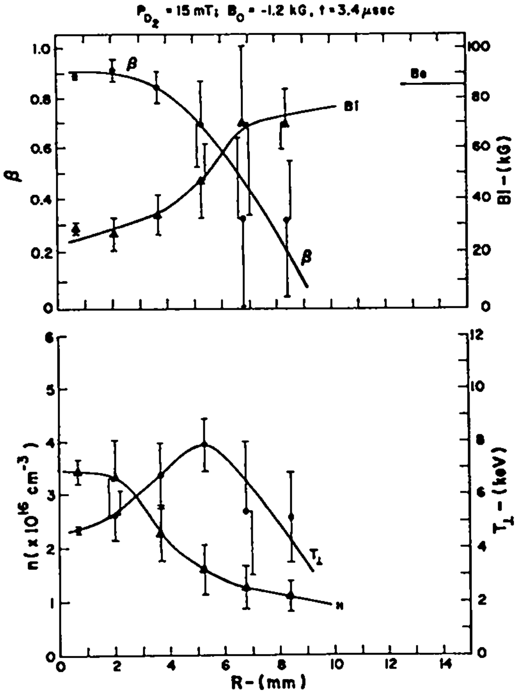

Fig. 65. As for Fig. 64 at 3.4 μsec after beginning of discharge; bias field -1.2 kG.

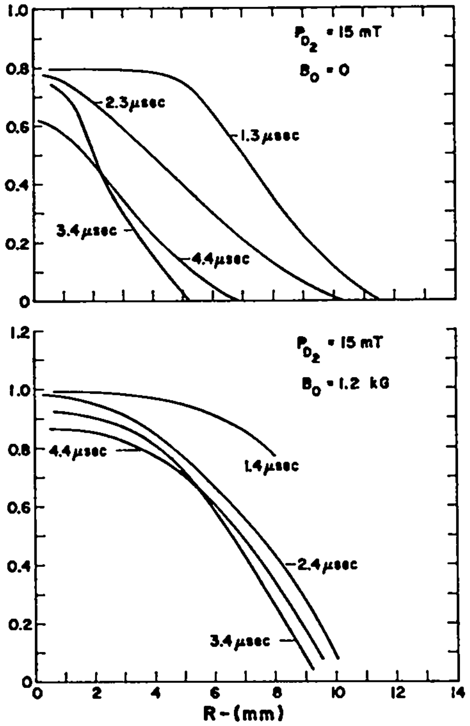

Fig. 66. Radial profiles of β vs radius at various times during discharge.(Upper: Zero bias field; lower: -1.2 kG bias field.)

β and the neutron emissions; the higher the value of β, the greater the neutron yield.

The β values (and the neutron yields) appear to depend on the condition of the discharge tube. In a relatively new tube, conditioned by a few discharges, the β's near the plasma axis were >0.9 with zero bias fields and > 0.95 with bias fields over the 4.4-μsec observation time. The data presented in Figs. 64-66 were taken in the same discharge tube, but after many discharges, and resulted in lower β values.

The graphs of plasma density in Figs. 64 and 65 were obtained from the interferograms with the assumption of a constant plasma length of 70 cm over the plasma radius. An elliptical (or cigar-shaped) plasma would result in larger plasma densities in the outer radial plasma regions than the plots of Figs. 64 and 65 indicate.

Discussion (With R. L. Morse)

The characteristics of the radial β profiles are in qualitative agreement with Morse's theory,[5] which treats the adiabatic relaxation of an initially thin sheath to a thickness of the order of an ion collisionless skin depth $\lambda_i = c/\omega_{pi}$ and allows the external field to penetrate the plasma. This relaxation discharges the radial electrostatic fields necessary to maintain a sheath thickness $< \lambda_i$, and propagates in from the end as an azimuthally symmetric torsional Alfvén wave whose axial velocity varies with radius and has a mean transit time of about 1 μsec.

An ion distribution function which is a function of the constants of particle motion, $\epsilon = M\overline{V}^2/2$ and $P_\theta = Mr(V_\theta + A_\theta)$, represents a stationary solution of the Vlasov equations. Hence an essentially Maxwellian distribution might be postulated in which P_θ (and hence radial) dependence is built into the temperature, "T"(P_θ), in order to explain the observed experimental results. An equally plausible explanation can be based on a type of isothermal distribution function of which the following is a convenient analytic example:

$$f_o(\epsilon, P_\theta) \sim \exp\{-[\epsilon + \omega P_\theta + P_\theta^2/2Mr_o^2]/T\}, \tag{5}$$

where ω and r_o are simple rotation and transverse anisotropy parameters, respectively. This gives a density and mean current velocity

$$n(r) = \frac{n_o}{(1 + r^2/r_o^2)^{\frac{1}{2}}} \exp\{[\omega^2 r^2 - 2\omega r(1 + r^2/r_o^2)A_\theta - r^2 A_\theta^2/r_o^2]/u^2\} \tag{6}$$

$$V_c = -(\omega r + r^2 A_\theta^2/r_o^2)/(1 + r^2/r_o^2). \tag{7}$$

Here $T = Mu^2/2$, $A_\theta(R = 0) = 0$, and $A_\theta(r)$ is given by Maxwell's $\nabla \times \overline{B}$ equation. In the limit ($r_o^2 \to \infty$) it can be shown that

$$\frac{"T"}{T} = a^2 + b^2 e^{-\alpha^2 r^2}, \tag{8}$$

where a^2, b^2, and α^2 are positive constants related to n_o, T, ω, and B_z, owing to the dominance of the centrifugal force term $r^2\omega^2$ in the exponent.

The "T" distribution decreases with increasing r in contradiction to the experimental results. For finite r_o^2, as opposed to the rigid-rotation limit $r_o^2 \to \infty$, the coefficient $(1 + r^2/r_o^2)^{-\frac{1}{2}}$ in front of the exponential in n(r) causes n(r) to decrease with increasing r, which is the desired result. For sufficiently small r_o^2, profiles of "T" resembling the experimental results for $T_\perp$ can be obtained. The mechanism responsible for the decrease of n(r) with radius is the combined effect of cylindrical geometry and a transverse anisotropy in the pressure tensor; when f_o is written out in terms of velocity components it is seen that there are really two transverse temperatures, $T_r = T$ and $T_\theta = T/(1 + r^2/r_o^2)$.

The increase with radius of the plasma temperature $T_\perp$ derived experimentally may also be partially accounted for by an elliptical (or cigar-shaped) plasma. In Eq. (4), which is used to calculate the temperature from pressure balance, $T_\perp$ is inversely proportional to n. As noted above, n was determined from the interferograms under the assumption of a constant plasma length over the plasma radius. If the plasma has an elliptical shape, n will have greater values at the large radii than those obtained from this assumption. Consequently, the temperature $T_\perp$ would be reduced at the larger plasma radii. However, this effect is not sufficient to eliminate the radial dependence of $T_\perp$.

References

1. A. A. Dougal, J.P. Craig and R.F. Gribble, Phys. Rev. Letters 13, 1 (1964).

2. P. Bogen and D. Rusbüldt, Phys. Fluids 9, 2296 (1966).

3. I.S. Falconer and S.A. Ramsden, Bull. Am. Phys. Soc., Ser. 2, 10, 219 (1965)(Abstract).

4. F. C. Jahoda, E.M. Little, W.E. Quinn, F.L. Ribe, and G.A. Sawyer, J. Appl. Phys. 35, 2351 (1964); E.M. Little, W.E. Quinn, and G.A. Sawyer, Phys. Fluids 8, 1168 (1965).

5. R. L. Morse, Phys. Fluids (to be published).

BUMPY PLASMA COLUMN EXPERIMENTS ON SCYLLA IV

(R. F. Gribble, E. M. Little, W. E. Quinn, F. L. Ribe)

Introduction

An equilibrium magnetic field configuration for the toroidal Scyllac device can be provided by the static "M and S" arrangement,[1] produced by a superposition of $\ell = 0$ (periodic mirroring) and $\ell = 1$ (wavy) magnetic fields.[2] In the case of a sharp plasma-magnetic field boundary, the static M and S equilibrium requires the inner magnetic lines to be sufficiently wavy that their lengths are equal to those of the outer lines. This necessarily introduces periodic regions of bad curvature which, in the high-β case, lead to macroscopic ballooning instabilities (flute modes of finite longitudinal wavelength) localized near the regions of bad curvature. The theoretical predictions of ballooning growth rates are strongly dependent on the plasma model. Collisionless (bounce-model) plasmas have ballooning growth rates for $m > 1$ which are one to two orders of magnitude slower than those computed on the collision-dominated, incompressible-fluid model.[3]

Experiments at Culham have shown that a collision-dominated plasma with no line tying gives $m = 1$ gross instability when subjected to an $\ell = 0$ magnetic field bump.[4] (Here the azimuthal dependence of the instability is given by $\cos m\theta$.) The instability growth rates for this collision-dominated case

($\lambda_{ii} = 0.4$ cm, $\lambda_{ii}/2\pi r_L \approx 0.7$, $\lambda_{ii}/2a \approx 0.4$) are in agreement with the incompressible-fluid prediction. Similar experiments are in progress in the collisionless plasma case of Scylla IV for which $\lambda_{ii}/2\pi r_L \approx 300$ ($\lambda_{ii}/2a \approx 300$), using an $\ell = 0$ magnetic field bump. It is planned soon also to excite a single plasma "bend" with an $\ell = 1$ coil like that of Figs. 79 and 84 of the next section. In the 1-m Scylla IV coil, the absence of line tying is not assured, and its presence or absence must be demonstrated. In particular, collision-dominated plasmas are also being generated to see if ballooning similar to that of the Culham experiment is encountered.

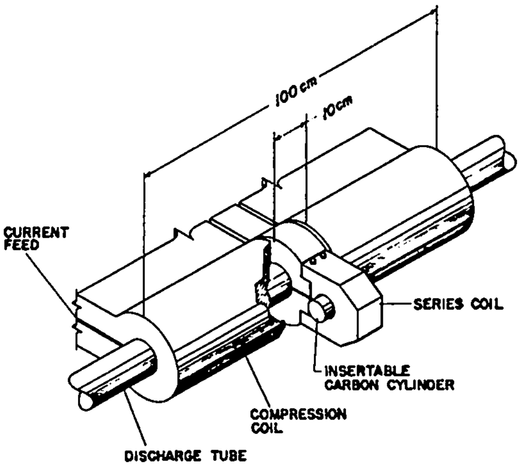

Fig. 67. Apparatus for generating an. adiabatically applied $\ell = 0$ magnetic bump in Scylla IV coil.

Experimental Arrangement

Two methods have been used in attempts to produce an $\ell = 0$ magnetic field bump in the central region of the 1-m length compression coil of Scylla IV. One method involves the independent excitation of an $\ell = 0$ bump through slots in the compression coil. The other method produces spatial changes in the current of the main compression coil in a completely passive way.

Attempted Use of Slot-Excited Ring Coils

The initial attempts to produce an $\ell = 0$ bump involved the insertion of a separate $\ell = 0$ coil into the main coil with an independent current feed through slots in the latter. These $\ell = 0$ coils consist of two half-turn coils with inside diameters of 11.0 cm, which are electrically driven in parallel (compare with the model coil of Fig. 74). The coils and their parallel-plate current feeds were impregnated in vacuum with epoxy resin and fiberglass to obtain mechanical strength and high-voltage insulation. The first coil was energized by 29.4 μF at 40 kV, giving a peak current of 400 kA through the coil sections. An electrical fault developed due to a mechanical separation in the vicinity of the coil feed tabs, and thus provided an electrical shorting path. The second coil with an improved epoxy-fiberglass structure also failed in the same way when energized by 12 μF at 37 kV, which produced a peak current of 280 kA through

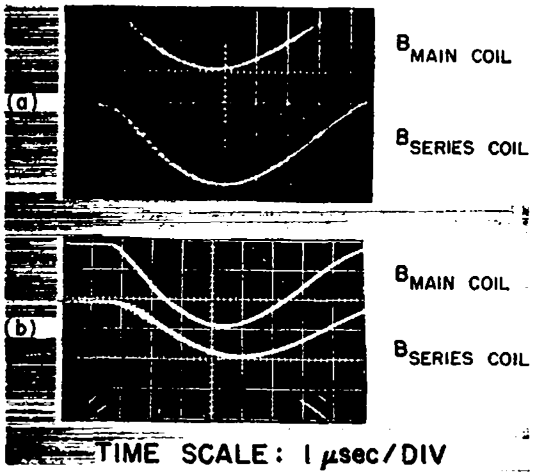

Fig. 68. Magnetic fields vs time; (a) 0.32-cm and (b) 0.95-cm carbon cylinder in series coil.

the coil. These mechanical-electrical difficulties combined with the relatively short extension of the $\ell = 0$ bump in the axial direction of the main compression coil have led to abandonment of this method in favor of the second method for the production of an $\ell = 0$ bump.

Use of a Coil in Series with a Section of the Compression Coil

The second method for the generation of an $\ell = 0$ bump in the magnetic field employs spatial changes in the current of the main compression coil itself. The principle for doing this "adiabatically" is shown in Fig. 67; this scheme gives an isolated perturbation at the center of the Scylla IV coil. An additional coil (series coil) is connected in series with a central section of the main compression coil. The added inductance of the series coil causes a reduction of the current drawn to its compression-coil section from the collector plate. In order to maintain a uniform field configuration in this region during the initial shock implosion phase of the discharge, magnetic flux is excluded from the series coil by means of a hollow carbon cylinder for its flux-penetration and L/R time. With the appropriate selection of the carbon resistivity, the field exclusion time can be in the range of 1-2 μsec.

In the present experiments, a 10-cm length central section of the main compression coil has been replaced by one of 7.6-cm length, with a gap of 1.2-cm on each side of the new section. A 6.35-cm diam coil was connected in series with the new central section. Carbon cylinders with outside diameters of 6.03 cm, lengths of 8.26 cm, wall thicknesses of 0.32 and 0.95 cm, and resistivities of 17.8 mΩ-cm have been used to provide the initial flux exclusion in the present experiments.

Figure 68 shows the magnetic field as a function of time in both the main compression coil and the series coil with the carbon cylinders in place. Measurements of the magnetic field in the central compression-coil section show the $\ell = 0$ bump to have $\Delta B_z/B = -0.10$. The corresponding fractional plasma surface excursion is estimated to be 0.2 for this nonperiodic bump. This series coil configuration has also been probed in a full-scale model which was driven at 50 kHz (cf. p.63). These measurements showed the magnetic field bump to have an axial extent of ~ 18 cm with no asymmetries in the radial and azimuthal directions.

With the series coil arrangement, the bump can readily be eliminated by inserting an aluminum cylinder in the series coil. This allows the experiments to be carried out with and without the $\ell = 0$ bump in a controlled manner.

Results

Plasma instability experiments have been performed in smooth-bore quartz discharge tubes of ~ 9 cm i.d. with the series coil arrangement described above; the primary Scylla IV capacitor bank operated at full energy (560 kJ at 50 kV) and the initial deuterium filling pressures were 15 and 125 mtorr. The Mach-Zehnder interferometer was used to view the plasma in the axial direction, and four interferograms were obtained during each discharge. In addition, STL streak cameras were used to view the plasma "side-on" in the center of the $\ell = 0$ bump section at the coil midplane and 20.3 cm off the midplane in a uniform magnetic field region. In general the data were taken with the hollow carbon and aluminum cylinders inserted into the series coil on alternate pairs of discharges.

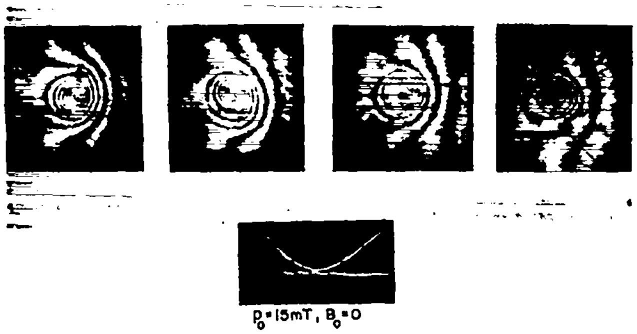

Fig. 69. Interferograms and oscillograms (upper trace: applied magnetic field; lower trace: times of interferograms (1 μsec/div.)) with 0.95-cm C cylinder in series coil. No bias field.

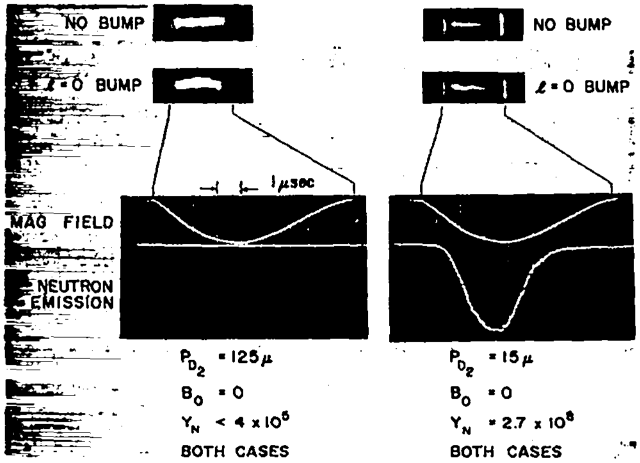

Fig. 70. Streak photographs with Al and 0.32-cm C cylinders in series coil (upper left: Al, 125 mtorr; upper right: Al, 15 mtorr; lower left: C, 125-mtorr; lower right: C, 15 mtorr). Oscillograms (1 μsec/div.) show magnetic field and neutron emission.

Collisionless Plasmas

In the low-pressure regime (15 mtorr) with the full primary capacitor bank (the collisionless plasma case) there were no definite characteristic differences between the discharges with the 0.32 and 0.95-cm carbon cylinders and with the aluminum cylinders in the series coil. Figure 69 shows a time-sequence of four interferograms taken on a single discharge at 15 mtorr with the 0.95-cm carbon cylinder in the series coil. The first two frames indicate some elliptical distortions (which also occur with the Al cylinder), whereas the other two, in the vicinity of the maximum compression field, are quite symmetrical. Examination of several such sets of interferograms taken with the ℓ = 0 bump (carbon cylinder in series coil) shows that there is no evidence of the occurrence of instability induced by the bump. The interferograms show maximum compressed plasma densities of ~ 3 x 10^{16} cm^{-3}.

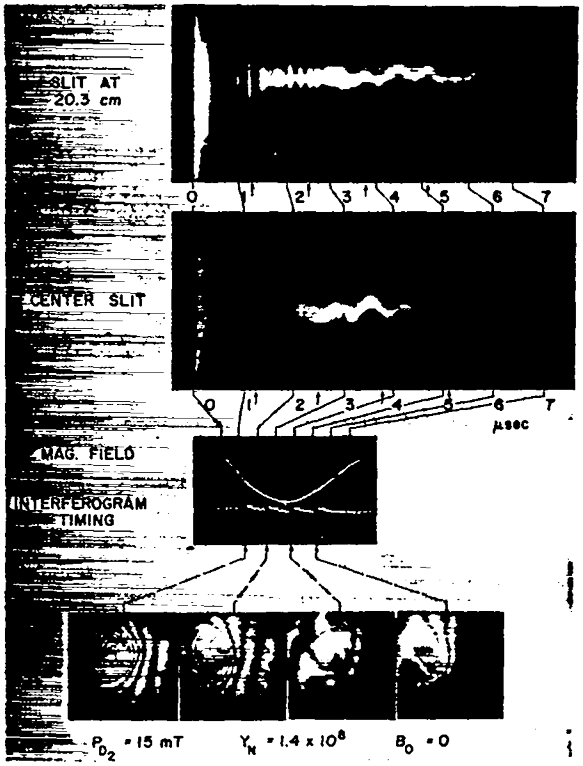

Fig. 71. Streak photographs, interferograms, and oscillograms (1 μsec/div.) on single discharge at 15 mtorr with Al cylinder in series coil.

Side-on streak photographs taken at the center of the ℓ = 0 bump section are shown in Fig. 70; with both the aluminum and carbon cylinders a uniform stable plasma column is produced at 15 mtorr which tends to develop a slow "wobble." Typical neutron yields for these cases are 2 x 10^8 per discharge. The time distribution of the neutron emission is shown in the lower right of the figure. These data show that in the collisionless plasma case, the ℓ = 0 bump ($\Delta B_z/B = -0.10$) does not produce an instability during the 5 μsec in which the plasma exists.

Figure 71 shows data taken on a single discharge in the absence of the ℓ = 0 magnetic bump with the aluminum cylinder in the series coil. The streak photographs show the wobble of the plasma column referred to above which begins at the coil midplane before it appears 20.3 cm off the midplane. The time sequence of interferograms correlates with the streak photographs in that a distorted fringe pattern develops (frames 3 and 4) as the wobble develops in the streaks. These phenomena appear to be related to the plasma production in the quartz discharge tube and in general are not observed in high-alumina discharge tubes.

Collision-Dominated Plasmas

Experiments were also performed with 125-mtorr initial filling pressure with the full bank energy, with and without reversed bias magnetic fields. In this case the compressed plasma density (1 to 2×10^{17} cm^{-3}) is approximately five times greater than in the 15-mtorr case and the neutron yields are less than in the collisionless case by more than two orders of magnitude. If the 15- and 125-mtorr cases have approximately the same β, simple pressure balance indicates the plasma temperature in the high pressure case would be reduced by a factor of five. Assuming a plasma temperature of 400 eV and a density of 2×10^{17} cm^{-3}, the ion-ion mean free path, λ_{ii}, is 1.5 cm which is approximately the plasma diameter. Consequently, with the 125-mtorr initial filling pressure, the plasma is in the collision-dominated regime.

Streak photographs at 125-mtorr pressure taken at the center of the $\ell = 0$ bump section are also shown in Fig. 70 in the absence of magnetic bias fields. With the aluminum cylinder in the series coil (upper left-hand streak) the plasma is uniform and straight with minor surface deformations. This is to be contrasted with the lower left streak photograph taken with the 0.32-cm carbon cylinder in the series coil, which shows the plasma column drifting away from the coil axis. This appears to be the development of an $m = 1$ instability similar to that observed in the Culham experiments[4] with a collision-dominated plasma. These phenomena were quite reproducible from discharge to discharge.

The addition of 1.2-kG reversed bias magnetic field appeared to enhance the $m = 1$ instability. However, good quality streak photographs were not obtained due to arcing in the slit of the wrapped quartz tube. The initial portion of the streak picture before the arcing showed the start of the $m = 1$ instability in a reproducible manner.

Interferograms taken with a 125-mtorr pressure and without bias fields showed slight indications of the $m = 1$ instability with the carbon cylinder but not with the aluminum in the series coil. In both cases there is a high-order surface fluting ($m \approx 6$) at early times which tends to confuse the observations at such times. However, this instability tends to disappear as the plasma is compressed and heated.

The addition of 1.2-kG reversed bias magnetic field causes the $m = 1$ instability to develop, as shown in the interferogram sequence of Fig. 72 taken with the 0.95-cm carbon cylinder in the series coil. In frame 3, at approximately the magnetic field maximum, the instability is well developed and continues to grow as seen in frame 4. These phenomena are quite reproducible from discharge to discharge with the carbon cylinder. The fact that it involves much fewer interference fringes than in the main plasma column indicates that the instability is growing over a small length. Figure 73 shows a corresponding time sequence of interferograms taken with the aluminum cylinder in the series coil. In this case the instability does not develop; it appears, therefore, that in the carbon case the $m = 1$ instability results from the $\ell = 0$ magnetic field bump.

Conclusions

These experiments show that in the collisionless plasma regime ($T \sim 2$ keV; $n \sim 3 \times 10^{16}$ cm^{-3}) of the Scylla IV θ-pinch, an $\ell = 0$ magnetic field bump ($\Delta B_z/B = -0.10$) does not produce an instability during the 5 μsec in which the plasma exists. In a collision-dominated plasma regime ($T_i \leqslant 400$ eV; $n \sim 2 \times 10^{17}$ cm^{-3}), the $\ell = 0$ bump produces an $m = 1$ instability localized near the magnetic bump. The instability is enhanced by the addition of a small reversed bias magnetic field.

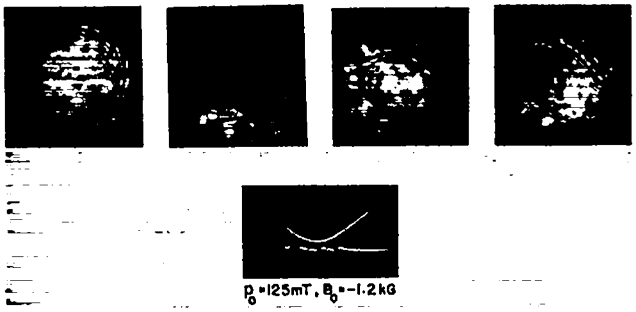

Fig. 72. Same as Fig. 69 but at 125-mtorr pressure and with 1.2 kG reversed bias field.

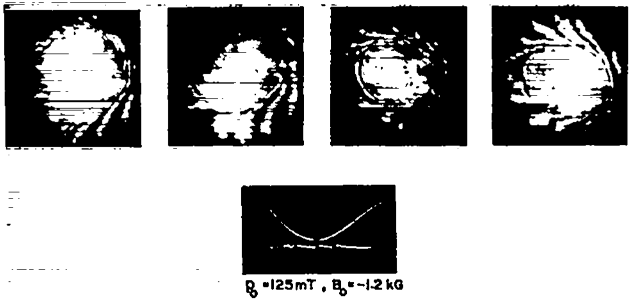

Fig. 73. Same as Fig. 72 but with Al cylinder in series coil.

References

1. F. Meyer and H. V. Schmidt, Z. Naturforsch. 13a, 1005 (1958).
2. J. L. Johnson, R. L. Morse, and W. B. Riesenfeld, Proc. APS Topical Conference on Pulsed High-Density Plasmas, 1967. LA-3770, B2.
3. F. L. Ribe, Nuclear Fusion 7, 81 (1967).
4. H.A.B. Bodin and A.A. Newton, LA-3770, A2.

MODELING OF STABILIZATION COILS OF THE TYPE TO BE USED IN SCYLLAC

(W.E. Quinn, F.L. Ribe, E.L. Zimmermann)

Introduction

In order to provide a toroidal equilibrium in Scyllac it is planned to use multipolar transverse magnetic fields having potentials of the form

$$\chi_\ell = C_\ell I_\ell (kr) \cos \ell\theta \cos kz, \qquad (1)$$

which are periodic along the minor axis z of the torus with wavelength $\lambda = 2\pi/k$ and also in the azimuthal angle θ around the minor axis with period $2\pi/\ell$. The object of the present measurements was to model realistically the fields from both "ring" type and "bar" type multipolar structures to see how nearly pure multipoles with sinusoidal behavior can be achieved. A major problem in the ring type of coil is to achieve a sufficiently long wavelength. It is also desirable to determine the calibration of the coils (multipole strength per unit driving current), as well as their inductances, in order to design the stabilization capacitor banks of Scyllac.

Apparatus

The coils were in all cases connected to parallel copper plates which could be driven in vertical slots in the θ-pinch coil. For this purpose a sectored Scylla IV compression coil of 11-cm i.d. was used as a mount, and the fields inside its bore were measured with small magnetic probes. Both the compression coil and the stabilization coils were driven from 50 kc, 5A amplifiers, developed especially at LASL by A. T. Brousseau. At this frequency the skin-effect conditions of the actual θ-pinch are well approximated without the effects of displacement currents. Driving currents were read peak-to-peak with a Tektronics clip-on current probe. The probes were calibrated for turns-area by insertion into a parallel plate copper line of known dimensions, driven by a measured current from the amplifiers.

Ring Coils in $\ell = 0$ and $\ell = 1$ Modes

A composite coil consisting of two half-turns, soldered to copper plates and driven at their outer edges, is shown in Fig. 74. Changes of the relative polarity of the currents driving the two independent feed-plate pairs allow it to be driven in either $\ell = 0$ or $\ell = 1$ mode. In the former the currents are in the same azimuthal direction; in the latter they are opposed.

A graph of radial field on the coil axis, parallel to the plane of the compression coil feed slot, is shown in Fig. 75 for a single $\ell = 1$ coil. The coil is placed in the external 5-cm slot of the sectored Scylla IV coil and is driven with the two half-turns opposed, i.e., $\ell = 1$. In the scale of mG/A the current in the denominator refers to that flowing in each half ring.

Figure 76 gives the corresponding radial field (but at $r = 3$ cm) for the $\ell = 0$ mode of the same coil. (The coil had an i.d. of 11.55 cm, compared to 10.95 cm for the bore of the compression coil.) Also shown is the radial component of fringing field of the compression-coil gap, as well as the net difference field measured with the $\ell = 0$ coil opposing the main compression coil with its current adjusted to cancel its B_r. From Fig. 76 it is seen that the "range" of the $\ell = 0$ coil is larger, because no net flux need be forced into the compression coil bore.

As a measure of the degree to which pure sinusoidal behavior can be approximated with $\ell = 1$ ring coils, three of them were excited in three (5-cm) central slots of the Scylla IV 1-m compression coil. The variation of B_r with z for a 26.4-cm spacing is shown in Fig. 77, whereas that for a 20.4-cm spacing is given in Fig. 78. The latter shows 24.5% second harmonic in the z direction. A nearly pure sinusoidal variation could be produced at $\lambda \approx 16$ cm. The azimuthal variation of B_z and B_r at $r = 2$ cm at the z position corresponding to peak fields were almost pure first-harmonic sinusoids.

Bar Coil with $\ell = 1$

The $\ell = 1$ bar coil is shown in Fig. 79. It consists essentially of two horizontal bars, driven at their centers by the copper sheets, with split current returns at the ends (in and out of the page) which are curves lying on the cylinder connecting the upper and lower bars. The purpose of the bar coil is to extend the $\ell = 1$ field over a longer range in the z direction than is possible with the ring design. Two of these bar coils were inserted with their tips about 6 mm apart in adjacent 5-cm slots of the Scylla IV compression coil (Fig. 80); the front half of a compression-coil sector has been omitted from the figure. The corresponding graphs of magnetic field over the period between these slots (and somewhat outside) are shown in Fig. 81; the period between adjacent gaps containing the current drive is representative of that of an infinite periodic system. It is seen that a fairly good harmonic variation of B_r is achieved. The irregularity at $z = 56$ cm occurs because of the separation of the tips and can probably be eliminated with more care. Corresponding azimuthal plots of the fields at the z position of peak field and on either side of it are shown in Fig. 82. At peak field there is nearly pure $\ell = 1$ harmonic variation. On either side there are about 20% of $\ell = 3$ contributions of aiding and opposing signs respectively. The current in the scale factor in G/A refers to the total current fed to the plates.

Inductance Measurement of the $\ell = 1$ Bar Coil

For the measurement of inductance, the bar coil was resonated with a parallel capacitor and the frequency of a driving oscillator-amplifier was adjusted over the 100- to 500-kHz range to give a voltage maximum. The capacitance of the G.E. 5-μF, 25-kV capacitor was measured as 5.21 μF. The total inductance in the circuit was 82.9 nH. Of this 32.0 nH were outside the bar coil and 26.7 nH outside the parallel-plate line. Therefore the coil itself had an inductance of 50.9 nH and the parallel-plate line an inductance of 5.3 nH.

High-Current $\ell = 1$ Coil for Test in Scylla IV

A high-current, high-voltage version of the $\ell = 1$ coil model shown in Fig. 79 has been built for testing in Scylla IV under conditions similar to those which will occur in Scyllac. As shown in

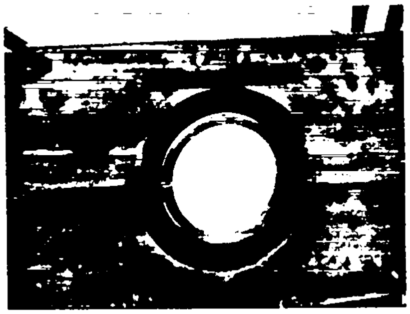

Fig. 74. Ring coils for generating ℓ = 0 or ℓ = 1 fields.

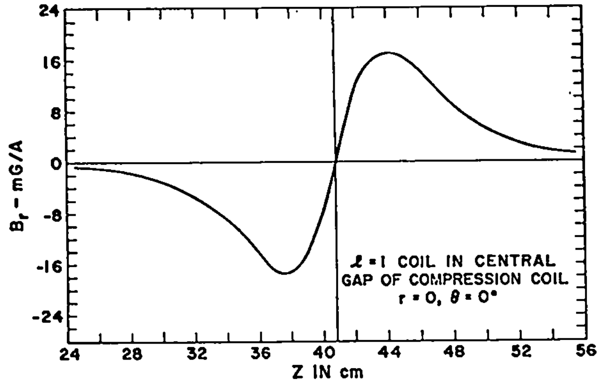

Fig. 75. Radial component of magnetic field (on axis) vs axial distance (z) for ℓ = 1 coil in Scylla IV.

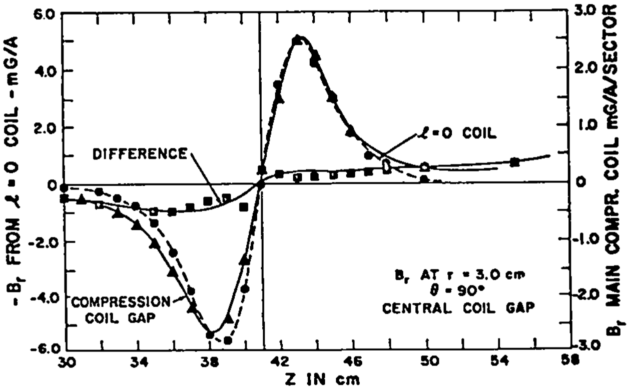

Fig. 76. Magnetic fields vs axial distance for ℓ = 0 coil in Scylla IV.

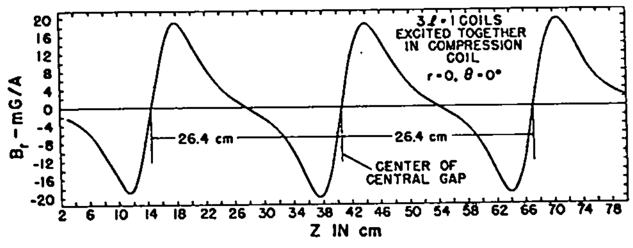

Fig. 77. Radial component of magnetic field vs axial distance for three ℓ = 1 coils;spacing 26.4 cm.

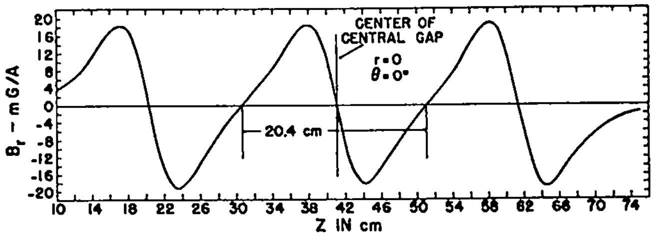

Fig. 78. As for Fig. 77 but with 20.4-cm spacing.

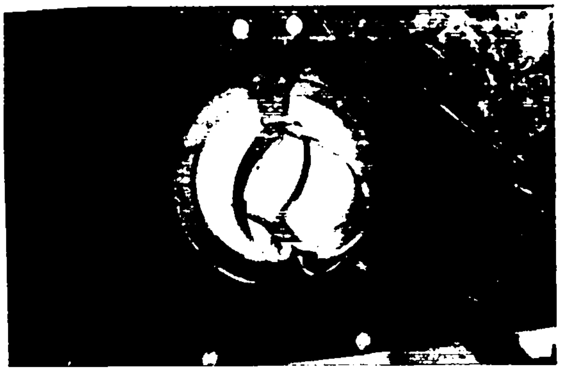

Fig. 79. Bar coil with ℓ = 1.

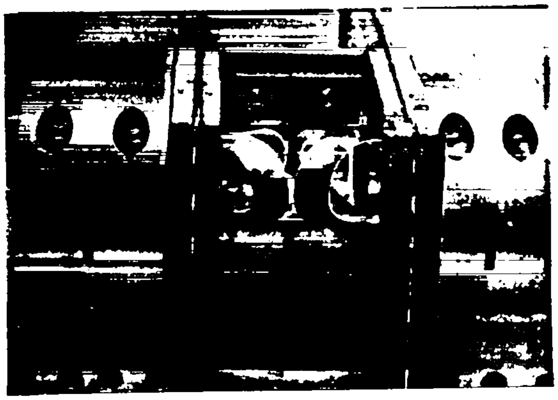

Fig. 80. Two ℓ = 1 bar coils in adjacent slots of Scylla IV compression coil.

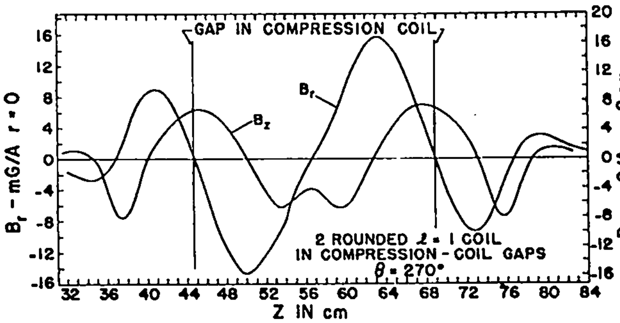

Fig. 81. Magnetic fields vs axial distance for two adjacent ℓ = 1 bar coils.

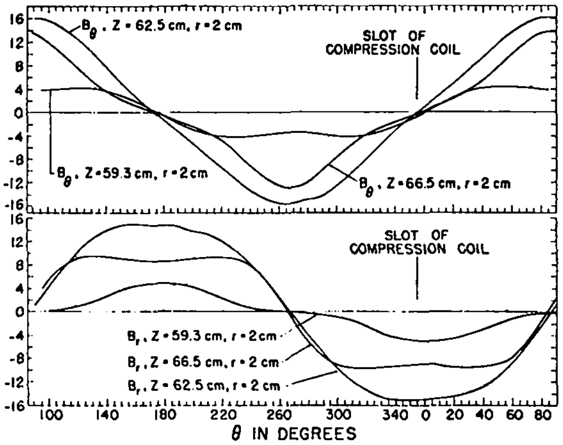

Fig. 82. Magnetic fields vs azimuthal angle (θ) for three z positions of Fig. 81.

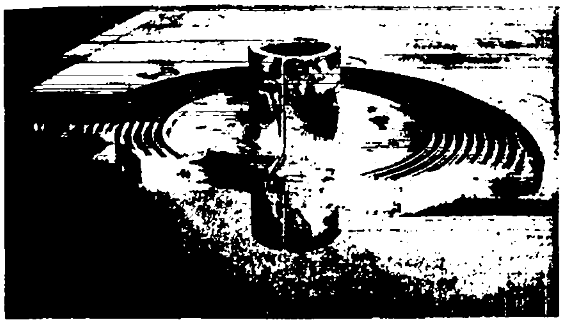

Fig. 83. High-current, high-voltage model of ℓ = 1 bar coil mounted in plane-parallel current feed plates.

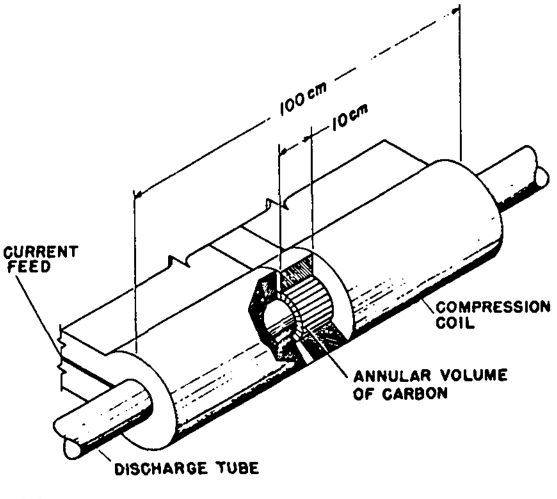

Fig. 84. Experimental arrangement for generating an ℓ = 0 field bump in center of 1-m Scylla IV coil.

Fig. 83, the coil and collector plates are molded into an epoxy-fiberglass structure capable of 60-kV, 200-kA operation. The central, flat portion of the structure will fit into a 1.5-cm slot in the Scylla IV coil, and it is intended to apply an ℓ = 1 bend to the plasma column. The ℓ = 1 coil is shown mounted in a heavy aluminum current collector which will connect through cables to a 50-kV capacitor bank which has been constructed above and in front of the Scylla IV compression coil.

Conclusions

As a result of the foregoing studies of the bar-type ℓ = 1 structure appears preferable and practical, although the ring-type structure is not excluded for $\lambda \leq 15$ cm. It would be inconvenient and costly of capacitor energy to drive ring-type ℓ = 0 structures, and they have restricted axial range. Therefore, serious consideration is being given to the use either of coil sections in series with the main compression coil, as in Fig. 67, or of field-decreasing annular grooves to provide the ℓ = 0 field shaping. As shown in Fig. 84, the annular groove is filled with a segmented carbon annulus to delay the onset of the field bump until after the plasma implosion, due to the time for the field to penetrate the carbon sections. It will be possible to program the ℓ = 1 field electrically to vary its strength relative to that of the ℓ = 0 field to give the optimum M and S-type configuration.

COOPERATIVE SCATTERING MEASUREMENTS ON SCYLLA III

(M. Daehler, F.L. Ribe)

Further Measurements of the Ion Feature

The preliminary data on the scattering experiment reported in LA-3628-MS (p. 34) have been superseded by final shot-by-shot measurements under the following improved conditions: (1) Better beam collimation reduced the stray light by a factor of 30, allowing scanning over the peak of the spectrum. (2) The previous calibration against SF_6 Rayleigh scattering has been replaced by a much improved calibration against dry nitrogen gas. (3) The vacuum system was converted to continuous liquid-N_2 trapping with a base pressure of 1×10^{-7} torr. (4) Operation of the spectrometer with two, rather than three, etalons was found to be adequate and reduced the effort required to maintain matched spacings.

The final results of these measurements have now been published.[1] The data for low-density (15 mtorr) gas and zero-bias field are summarized in Fig. 85. The band indicating the theoretical thermal spectrum was calculated for a plasma with $T_i = 2.0$ keV, $kT_e = 345$ eV, and $n = 2.8 \times 10^{16}$ cm^{-3} from an exact expression for the scattering due to thermal plasma density fluctuations; the range indicates the uncertainty in the Scylla III plasma density. It is apparent that the scattered signal may be considered to be composed of two parts: a broad, low-intensity component which has the spectral width and intensity equal, within experimental error, to those of the theoretical prediction for the ion feature, and a much more intense nonthermal component. The large, nonthermal peak has a maximum intensity larger than the thermal component intensity by a factor of 15 for $B_o = 0$, and by a factor of 45 for $B_o = -750$ G. The large central peak is thought to be a consequence of cooperative charge density fluctuations other than those associated with thermal density fluctuations. These results were reported at the 1967 Princeton Conference on Fluctuations and Diffusion in Plasmas.[2] They imply a density fluctuation level at the center of the plasma $\delta n/n \approx 0.02$. The corresponding anomalous diffusion coefficient on the basis of low-β theory would be about 0.01 of the Bohm value.

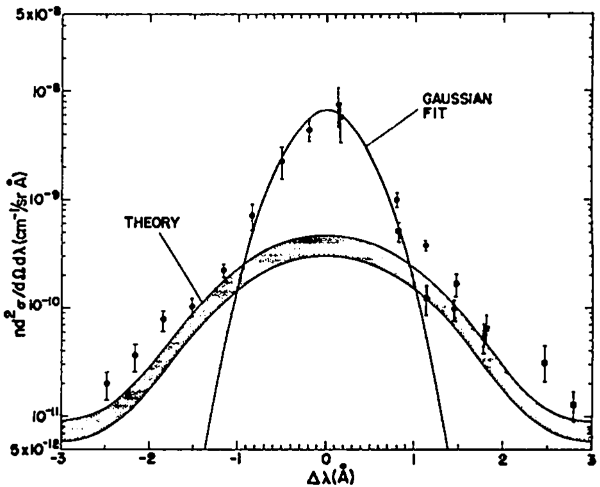

Fig. 85. Shot-by-shot scattering measurements on Scylla III plasma ($p_o = 15$ mtorr, $B_o = 0$).

Multichannel Spectrometer for Measurements of the Ion Feature

The twelve-channel spectrometer offers the opportunity of measuring the complete central component of the scattered light spectrum in one or two plasma discharges. This gain is significant because of both the increased rate of data acquisition and the possibility of measuring shot-to-shot differences in the scattered-light spectrum. The optical plan of the instrument is shown in Fig. 86. Light to be analyzed is focused onto the top aperture A, collimated by lens L1, and then transmitted through the three Fabry-Perot interferometers E1, E2, and E3. The Fabry-Perot fringes, formed at infinity, are focused by lens L2 onto the Fafnir device F (named by its inventor, J. G. Hirschberg, after the monster of Wagnerian opera). The Fafnir device consists of a set of nested cylinders, each of which has a highly-reflecting end surface, with diameters chosen so that their end-surface areas are identical. The Fafnir surface thus consists of a set of annular areas, and each receives light from a corresponding area of the Fabry-Perot fringe pattern. Since each diameter on the fringe pattern corresponds to a different angle of transmission through the Fabry-Perot interferometers, and hence a different wavelength of peak transmission, each of the 12 annular Fafnir

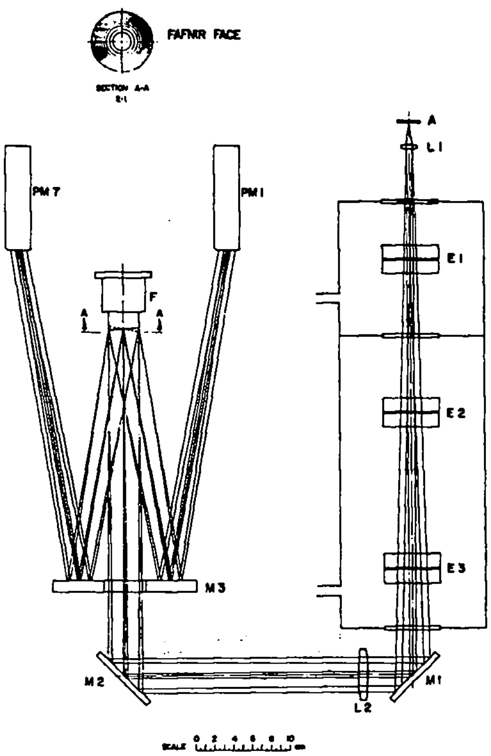

Fig. 86. Optical layout of the multichannel Fabry-Perot spectrometer.

areas is illuminated with light of a different wavelength. The range of wavelength transmitted to a given annulus corresponds to the range of angle through the interferometer.

The end faces of the cylinders are not cut off square, but are cut at an angle of 5° to the optic axis, so that each reflects its light into a different azimuthal direction. There is a ring of 12 photomultipliers (e.g., PM1, PM7) oriented with the same azimuthal symmetry, so that each annular Fafnir area reflects its light into one of these photomultipliers. Thus the light is spectrally resolved into twelve channels. The Fafnir face is ground slightly concave, to keep the reflected beams from spreading beyond the dimensions of the photomultipliers.

Two of the Fabry-Perot interferometers are those presently in use, with spacings of 0.454 mm (free spectral range 11.010 cm^{-1} or 5.303 Å). The third interferometer will have a small spacing, probably 0.1 to 0.2 mm, and a proportionately wider free spectral range. Its essential purpose is to act with an interference filter (which will intercept the light beam before it reaches the spectrometer) to suppress the unwanted orders of the resolving interferometers. There are several advantages of using such an interferometer-filter combination for this purpose instead of just a filter. The interferometer-filter will have a wide passband (15-20 Å), and its transmittance over the spectrometer scanning range will be nearly constant, so that no correction on the spectrum will be required. The wavelength of peak transmittance for the narrow-spaced interferometer depends upon the angle of transmission in the same way as it does for the resolving interferometers, so that each channel sees the filter-interferometer passband centered on the channel's wavelength.

The focal length of lens L2 and the diameters of the Fafnir cylinders are chosen so that each annular channel corresponds to a spectral range of 0.2 Å. Thus the channels are separated by 0.2 Å, the total spectral range is 2.2 Å, and each channel has a spectral width slightly greater than 0.2 Å (because of the finite finesse of the interferometers).

Assembly of the instrument has been completed. Preliminary measurements show that the resolution and spectral spacing of the channels agree with the design values. Considerable attention has been paid to the reduction of scattered light, a problem which can be especially severe in this type of multichannel Fabry-Perot spectrometer. Part of the scattered light comes from scattering at the irregular edges of the Fafnir image-dissecting device, and can be at least largely reduced by a set of lenses and annular apertures imaging each annular area of the Fafnir surface onto an annular aperture placed close to the corresponding photomultiplier. Other scattered light comes from reflections at windows, lenses, and back faces of the Fabry-Perot plates. This light can be reduced by adding a small aperture (1- to 2-mm diam) in each channel following the lens just described and placed approximately at its focal point. In addition, anti-reflection coatings ($R \approx 0.1\%$) have been put on the chamber windows, the lens focusing the Fabry-Perot fringes, and on the back face of the last Fabry-Perot face. The efficacy of the apertures was shown by measurements using makeshift apertures, but now some stable, carefully-made apertures are being fabricated. The annular apertures are being made by CMB Division at LASL by photoetching a copper coating put onto glass disks.

A. Brousseau (LASL) is building a signal-storage device to permit the 12 signals to be presented on only three oscilloscope beams. A 2-μsec sweep will be divided into four equal intervals; the first channel signal will be recorded in the first half μsec in the normal way, and the second, third, and fourth channel signals will follow in the remaining half-μsec periods after being stored in delay lines for 0.5, 1.0, and 1.5 μsec, respectively. Although the scattered laser pulse is only 25-nsec long (broadened to about 60 nsec by the oscilloscope amplifiers), the channels are made 0.5-μsec long to permit the scattered signal to show as a pulse on the bremsstrahlung background. A gating device is being added to ensure that the delayed channels do not include the bremsstrahlung level of the previous channels.

References

1. M. Daehler and F. L. Ribe, Phys. Rev. 161, 117 (1967); Phys. Letters 24A, 745 (1967).

2. Physics Today, 20, 115 (1967).

SCYLLA IA

(V. A. Finlayson, G.A. Sawyer)

A completely new Scylla experiment has been built. Since the new device replaces Scylla I, it has been designated Scylla IA. The choice of a good name is difficult, however, since its electrical parameters more closely approximate those of Scylla III, and it uses capacitors, spark gaps, and collector plate design like those of Scylla IV. The design incorporates the latest engineering improvements mostly developed for Scylla IV and Scyllac.

Scylla IA will accomplish three objectives. (1) It will provide a rather compact, reliable device with which plasma diagnostic techniques appropriate to θ-pinches can be developed. Work on holographic interferometry (p. 85) is a good example of the techniques to be tried out. (2) Scylla IA has been designed for higher electric field, 1.5 kV/cm, as contrasted to about 1.0 kV/cm for all present Scylla devices. This will permit investigation of the effect of electric field on plasma parameters. Both theory and previous experimental experience suggest that high electric field is important to the initial shock dynamics of the θ-pinch. (3) The relatively small new device will make it possible to try out some engineering innovations which will help Scyllac design.

The higher electric field is achieved with a half-turn coil arrangment as shown schematically in Fig. 87; 50-kV capacitors are used as in Scylla IV. Space limitations restrict the number of capacitors to 36, with an energy storage of 90 kJ, and this results in a comparatively high source inductance. Efficiency of voltage-energy transfer to the coil is about 57% with the half-turn connection. The design also permits connection as a conventional one-turn device, in which case the efficiency is 77%. The layout of the coil-collector plate system is shown in Fig. 88. Coaxial cables from the capacitor bank feed the two collector plates of the half-turn coil. A solid-dielectric crowbar gap is shown at the rear of each collector plate.

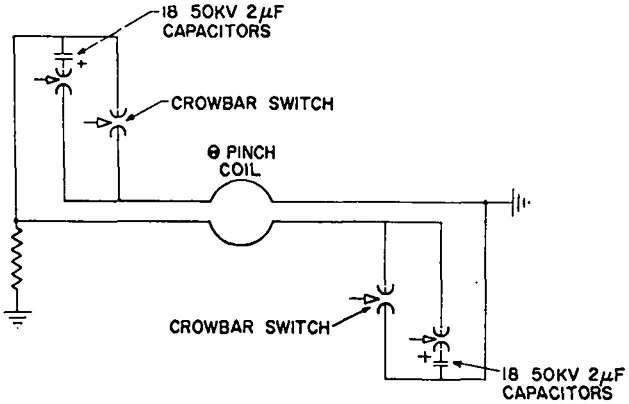

Fig. 87. Schematic of electrical system of Scylla IA.

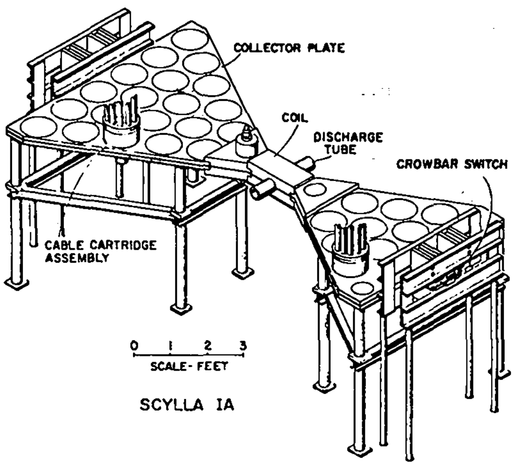

Fig. 88. Mechanical layout of Scylla IA.

Collector plate and coil design draws heavily on present Scylla IV technology and on the design studies for Scyllac.

To date Scylla IA has been fired at a main bank voltage of 45 kV in the half-turn series configuration. Electrical parameters were measured at 45 kV, which when extrapolated to full voltage give: E_θ (at inner tube wall) = 1.5 kV/cm, I_{max} = 1.61 MA, quarter period $\tau/4$ = 1.75 μsec, and B_{max} = 88 kG. These compare within a few percent with the predicted parameters.

There has been practically no operation with plasma so far, and plasma properties are not yet known.

MEASUREMENT OF θ-PINCH END LOSS USING A GAS LASER INTERFEROMETER

(K. S. Thomas)

Introduction

End loss is apparently the dominant loss mechanism in the present generation of large θ-pinches.[1] Measurements of the total amount of plasma present as a function of time have given plasma loss rates.[2,3,4,5] Direct measurements of plasma escaping out the ends of θ-pinches have been made in several ways: direct photography,[1,6] pressure probes,[4] and measurement of the energy spectrum and flux of axially excaping ions.[7] In the present work a measurement of the plasma density outside the end of the θ-pinch coil was made with a gas laser interferometer.

The end loss measurements were performed on Scylla III, a 150-kJ θ pinch which has a coil 20-cm long and 10-cm diam, with a geometric mirror ratio of 1.3. The θ-pinch was operated in the low-pressure regime (no bias field, 20 mtorr filling pressure) at a main bank voltage of 73 kV. Extensive measurements of the Scylla III plasma under these operating conditions have been reported.[8]

Interferometer

The gas laser interferometer consisted of a He-Ne gas laser (Spectra Physics, Model 115) modulated by an external cavity. This type of interferometer was first used by Ashby and Jephcott.[9] The short duration of a θ-pinch plasma requires a fast time response, so the 3.4-μ laser radiation is monitored by means of an InAs detector.[10,11] A gas laser interferometer with a rotating corner reflector feedback system has been used on Scylla III.[8] This system works well when the fringe shifts are large, the limit of sensitivity being about 0.1 fringe, which is equal to an integrated electron density of 3.28×10^{15} cm^{-2}.

A method of measuring smaller amounts of plasma, developed by Hammel and Rode,[12] was used in this experiment. It is similar to the technique of Hooper and Bekefi[13] but has the advantage of being able to be applied to single plasma discharges. For a feedback system, the interferometer uses a mirror mounted on an audio speaker with its acoustic cone removed. This mirror is modulated at a frequency of 1 kHz to give a change of path length in the external cavity of about $0.1\ \lambda$. If the modulation is monitored just prior to the θ-pinch shot, the output signal of the detector may be calibrated in terms of plasma density. The frequency response of the interferometer and detector system was flat from several hundred Hz to at least 5 MHz; hence, the difference in frequencies of the modulation and plasma signals should not introduce any appreciable error.

As would be expected, the interferometer was very sensitive to ambient vibrations. By mounting the interferometer on a frame which was well isolated from the θ-pinch and from the floor, the interferometer modulations caused by ambient vibrations were mostly of several hundred Hz or less, and these were rejected by introducing a low-frequency cutoff of 300 Hz in the detector system. With this arrangement, usable data were obtained on about half the θ-pinch shots.

Measurements

The measurements were made with the laser beam transverse to the discharge tube axis. The path of the beam through the 8-cm diam quartz discharge tube is given by coordinates of a reference system centered on the discharge tube axis at the coil midplane; z is the distance of the laser beam from the coil midplane in the axial direction , x the perpendicular distance of the beam from the discharge tube axis, and y is along the beam path. Measurements were made at $z = 0$ and $z = 11.5$ cm (1.5-cm beyond the coil end). Measurements were also attempted transversely at $z = 15$ cm and axially along the discharge tube outside the main plasma core. In both cases large plasma effects were observed, regardless of the value of x, of the order of 2×10^{16} cm^{-2}. These were probably due to bombardment by hot plasma of the discharge-tube wall outside the coil region. Framing pictures taken by an image-converter camera confirm wall bombardment in this region.

Oscillograms of typical data at $z = 0$, $x = 2.35$ cm, with and without plasma, and at $z = 0$, $x = 1.65$ cm are shown at the left in Fig. 89. In each photograph, the upper trace shows the magnetic field in the coil and the lower the interferometer output. In the case of no plasma, a small amount of magnetic pickup is observed in the detector system. This pickup, unfortunately, is not completely reproducible from shot to shot and constitutes the sensitivity limit of the interferometer. For the cases with plasma, the plasma present before the main bank is fired is due to the preionizer. After the main bank is fired, the plasma level rises slightly due to increased ionization and then drops quickly to below the limits of sensitivity of the interferometer as the plasma is swept toward the center of the discharge tube by the compression field. The drop in plasma signal occurs 0.3 μsec later at $x = 1.65$ cm than at $x = 2.35$ cm.

At the right of Fig. 89 are shown oscillograms taken outside the coil for $z = 11.5$ cm, and $x = 0$, 0.4, and 1.95 cm. The preionized plasma level is lower in these cases. For $\sim 0.5\ \mu$sec after the main bank is fired, an increase in plasma signal occurs for all values of x. This signal varies greatly from shot to shot and is probably due to ionized wall material. The rising magnetic field sweeps away the plasma and also prevents further bombardment of the walls in this region. At later times the end loss plasma is seen.

The results of the measurements outside the coil ($z = 11.5$ cm) are shown in Fig. 90, where the integrated plasma density is plotted vs x for various times after the firing of the main bank. The data for $x = 0.1$ cm were taken with the laser beam passing on the opposite side of the discharge tube axis from the other points in order to insure that the peak was at $x = 0$. Each point is the average of about a half dozen readings and the error bars show the average deviation. A possible source of error lies in the fact that the laser beam diameter is about 3 mm, which is an appreciable fraction of the width of the peak. If the solid curves in Fig. 90 are assumed and the data are Abel-inverted, the results in Fig. 91 are obtained, with density as a function of radius for

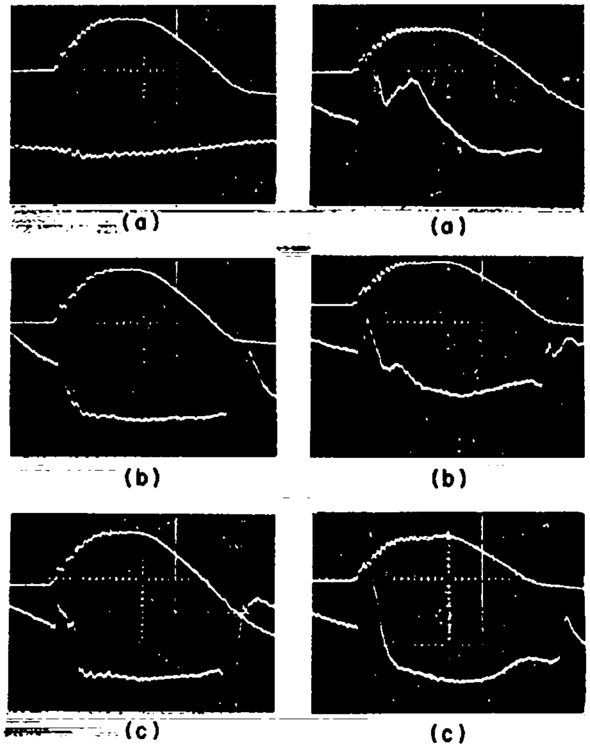

Fig. 89. Left: Oscillograms for z = 0; (a) x = 2.35 cm (no initial gas filling), (b) x = 2.35 cm, (c) x = 1.65 cm. Right: Oscillograms for z = 11.5 cm (1.5 cm outside coil); (a) x = 0, (b) x = 0.4 cm, (c) x = 1.95 cm. In each case, upper trace is magnetic field, lower trace is interferometer output. Sweep speed 1 μsec/cm.

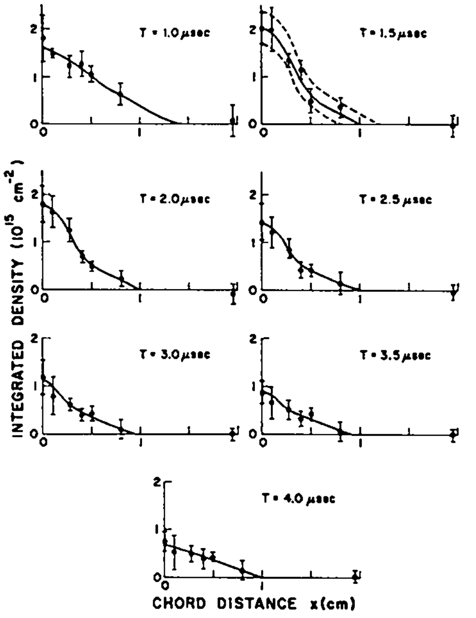

Fig. 90. Integrated plasma density at different times vs chord distance from discharge-tube axis (z = 11.5 cm).

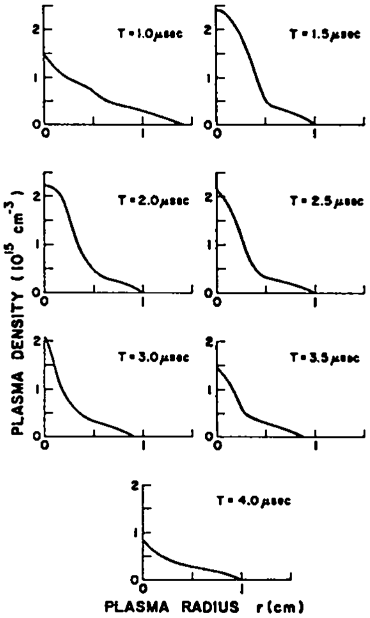

Fig. 91. Plasma density at different times vs radius (z = 11.5 cm).

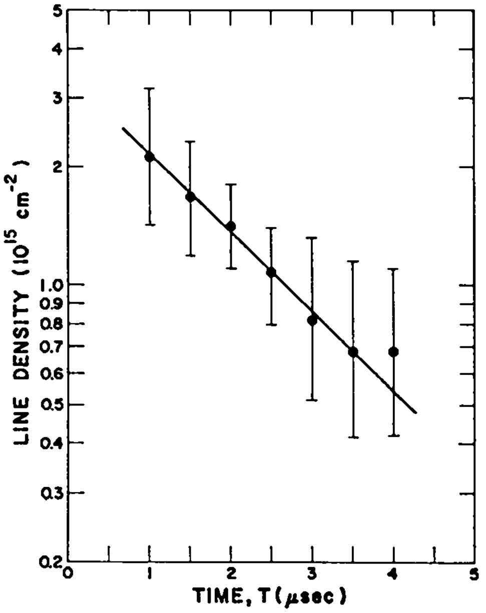

Fig. 92. Line density at z = 11.5 cm vs time.

different times. These values may be used to calculate the line density (particles per cm of tube length) and the results are given in Fig. 92. The error bars indicate the values which would be obtained from curves such as are shown by the dotted lines in Fig. 90 for $T = 1.5\ \mu sec$.

End Loss Rate

The measurements at $z = 0$ show that, after the compression of the plasma by the magnetic field, the plasma density outside the central plasma core is less than the interferometer sensitivity, i.e., < about $0.01\ \lambda$ or $3.3 \times 10^{14}\ cm^{-2}$. Thus the average plasma density along the 7-cm path length inside the discharge tube is less than $5 \times 10^{13}\ cm^{-3}$. The much higher densities ($\sim 10^{15}\ cm^{-3}$) outside the coil ends provide evidence that most of the plasma is lost at the ends. The line density of plasma outside the coil ends, N_o, is related to the decay of plasma inside the coil by

$$N\ell/\tau = 2vN_o \quad , \tag{1}$$

where N = line density inside the coil, ℓ = length of the plasma, τ = e-folding time for plasma loss, and v = average streaming velocity of the escaping ions.

For the operating conditions used in this experiment N has been measured[8] at $T = 1.8\ \mu sec$ to be $4.3 \pm 0.8 \times 10^{16}\ cm^{-1}$. Although the exact length of the Scylla III plasma is not known, neutron yield and an extrapolation from the known plasma lengths in the Scylla I and Scylla IV θ-pinches both indicate that it is 5 cm; τ as measured from the data of Fig. 92 is $2.25\ \mu sec$. Earlier magnetic probe data[8] gave $\tau = 1.8\ \mu sec$.

From Fig. 92, $N_o = 1.5 \times 10^{15}\ cm^{-1}$ at $T = 1.8\ \mu sec$. If this is inserted in Eq. (1), the results for the two values of τ are $v = 4.0 \times 10^7$ cm sec^{-1} ($\tau = 1.8\ \mu sec$), and $v = 3.2 \times 10^7\ cm\ sec^{-1}$ ($\tau = 2.25\ \mu sec$).

The measured ion temperature, T_i, for Scylla III is 1.9 keV,[8] which corresponds to an average ion thermal velocity of $4.3 \times 10^7\ cm\ sec^{-1}$. Thus the measured plasma densities are consistent with streaming velocities in the neighborhood of the ion thermal velocity.

Helpful suggestions concerning the construction of the interferometer were received from J. E. Hammel, and valuable assistance in constructing and performing the experiment was provided by M. H. Thomas.

References

1. H. Griem, et al., USAEC Report TID-23705 (1967) 31.
2. E.M. Little, W.E. Quinn, and G.A. Sawyer, Phys. Fluids 8, 1168 (1965).
3. W.E. Quinn, E.M. Little, F.L. Ribe, and G.A. Sawyer, in "Plasma Physics and Controlled Nuclear Fusion Research," (IAEA, Vienna, 1966) Vol. I, p. 237
4. H.A.B. Bodin, et al., ibid., Vol. I, p. 193.
5. A.C. Kolb, et al., ibid., Vol. I, p. 261.
6. E.A. McLean, Naval Research Laboratory, Private Communication to F.L. Ribe, April 1966.
7. R. L. Bingham, et al., in "Plasma Physics and Controlled Nuclear Fusion Research," (IAEA, Vienna, 1966) Vol. I, p. 301.
8. G. A. Sawyer, V.A. Finlayson, F.C. Jahoda, and K.S. Thomas, Phys. Fluids 10, 1564 (1967).
9. D.E.T.F. Ashby and D.F. Jephcott, Appl. Phys. Letters 3, 13 (1963).
10. D.A. Baker, J.E. Hammel, and F.C. Jahoda, Rev. Sci. Instr., 36, 395 (1965).
11. R. F. Gribble, J. P. Craig, and A.A. Dougal, Appl. Phys. Letters 5, 60 (1964).
12. J.E. Hammel and D.L. Rode, Los Alamos Scientific Laboratory Report LA-3730 (1967).
13. E.B. Hooper, Jr., and G. Bekefi, Appl. Phys. Letters 7, 133 (1965).

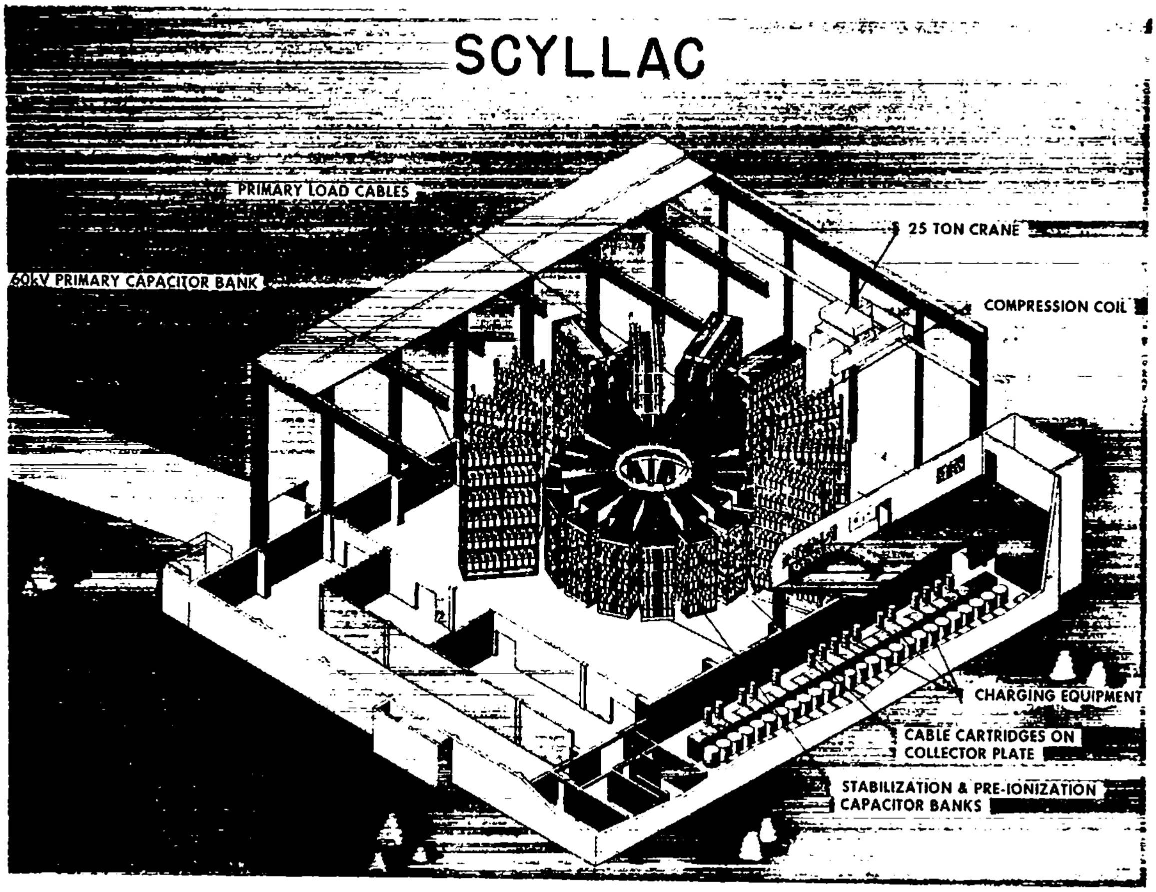

Fig. 93. Proposed layout for Scyllac.

SCYLLAC ENGINEERING

(Scyllac Engineering Team)

The engineering of the toroidal Scyllac (LA-3487-MS) has begun, and the general layout is shown in Fig. 93. The load coil in the center has a major diameter of 5 m, a circumference of ~ 15 m, and a minor diameter of 20 cm. Projecting radially from the coil are 15 plates that collect the current from the capacitor bank to the collector plates. The energy for each collector plate is stored in a 60-kV primary capacitor bank which consists of 216 capacitors rated at 2-μF, 60-kV. The total energy in this system is ~ 9.7 MJ. The system will also include stabilization and pre-ionization capacitor banks. The equipment for charging all capacitor banks is shown. The experimental area will be serviced by a 25-ton crane.

The Scyllac building will be attached to the present Administration Building. The experimental area will be four stories high including the basement, with a floor area of 100 x 100 ft. The north side of the building will contain the charging equipment in the basement and three floors for the control room, a computer room, diagnostic laboratories, and offices.

Although Scyllac will be toroidal, a linear version called "Pre-Scyllac," is being designed; it would be used to answer certain plasma physics questions. A model of Pre-Scyllac was built to identify some of the general system engineering problems. The coil is assembled in a linear geometry with the collector plates and racks alternating to the left and the right for each section. There will be 15 1-m sections of coil. The collector plates, cables, capacitor banks, and charging equipment will be the same for the linear and the toroidal geometries.

The Scyllac building requires the longest time to design and construct. A detailed set of criteria drawings and specifications were completed. Preliminary engineering funds were provided by the AEC to engage an architect-engineering firm. The A-E has completed the Title I drawings and specifications for the building. These drawings are being reviewed.

The engineering of the Scyllac system is proceeding in three steps: component development, system development, and system design. The principal components being developed for Scyllac are: a 60-kV, 1.5- to 2.0-μF capacitor; low-inductance, 60-kV coaxial cable; and crowbar switches. The development of the capacitor and coaxial cable is a cooperative effort between LASL engineers and industry. An appropriate specification for the component is written by LASL engineers and sent to several companies for their proposals to meet the specification. Sample components are purchased from all companies capable of supplying units meeting the requirements. These components are tested at the LASL in the manner in which they will be used. Reports on performance and postmortem examination are then sent back to the company to assist them in building a better component. This procedure is repeated until an adequate component is developed.

The development of the 60-kV capacitor has been under way since early 1965. Six companies are participating and two of them have supplied production lot samples. The test results indicated that the target objective of 2 μF (3.6 kJ) cannot be attained in production, but 1.7 μF (3.0 kJ) appears feasible and will be satisfactory for Scyllac. The capacitor development will continue for this 3.0-kJ goal.

The cable development also began in early 1965. Five companies are participating and three of them have supplied cable that appears satisfactory for Scyllac. The other two companies are very slow in delivering test cable.

Crowbar switches are required to short circuit the load coil at peak current and to trap the magnetic field in the coil so that it will decay exponentially, allowing plasma study for 100 μsec or more. A metal-to-metal contact, exploding-foil switch, invented by J. Marshall (see p. 77) is being developed for short circuiting the load. It may also be necessary to short circuit the individual capacitors simultaneously. Several types of spark gaps are being evaluated for this application. A new laboratory facility was built and has been staffed for the crowbar switch development.

The system development consists in building and evaluating all components, circuits, and hardware being developed or designed for Scyllac. A 4% prototype system is being built for this purpose. It will contain 200 60-kV capacitors and spark gaps, over 10,000 ft of cable, and a significant quantity of cable cartridge terminations and other new mechanical hardware required for the Scyllac system. The initial system for driving one collector plate with 72 capacitors is approximately 90% complete and will be operating by January 1968.

The Scyllac system is being designed by a group of ten engineers plus draftsmen from the LASL centralized engineering department. These engineers design to the requirements specified by the Sherwood physicists and development engineers. The design, construction, and installation of the system has been scheduled using modern evaluation and review techniques. The significant dates in the Scyllac schedule are given below, provided funding is obtained in FY-1968.

Building	
Title I, Preliminary Design Complete	Nov. 1967
Title II, Final Design Complete	March 1968
Construction Begin	May 1968
Construction Complete	July 1969
Energy System	
Final Design Complete	Dec. 1968
Installation Begin	July 1969
Checkout Begin	July 1970
Experiments	
Begin	Jan 1971

PASSIVE CROWBAR CONSIDERATIONS FOR SCYLLAC

(W.E. Quinn)

The time duration of the main compression and stabilization magnetic fields of the Scyllac device depends entirely on the passive crowbar switches and their location in the system. When closed at the maximum of the compression current, these switches clamp the magnetic energy in the coil, allowing the current to decay with a time constant L/R of the crowbar circuit. Not only must this L/R time be of the order of 100 μsec, but the inductance of the crowbar branch must be small compared to that of the main capacitor bank and its feeds to the coil. This latter requirement minimizes the energy returning to the capacitor bank from the coil and improves the magnetic field waveform. The location of the crowbar switches in the Scyllac system is analyzed below in terms of the resulting L/R times and magnetic waveforms.

The system considered is one of the 15 identical Scyllac sections, of the design referred to in the preceding section. This design consists of a collector plate with 24 rows of the cable cartridges (row separations = 6.26 in.) with alternating rows of four and five cartridges. The horizontal portion of the collector plate is 42.5 in. wide and the skirts are 42 in. wide. The compression coil has an i.d. of 11 cm and a length per section of 102.9 cm. The parameters of this design are given in the appended table. The resistances have been calculated by using the period of the primary bank (15.7 μsec) to obtain an electromagnetic skin depth (0.57 mm).

The effect of exploding-foil solid dielectric crowbar switches in the system is considered. It is assumed that two switches are used, each with a resistance of 10 μΩ. In Fig. 94, the schematic circuit diagram of the system with the crowbar switch at the rear of the collector plate system is shown at (a). The indicated parameters were inserted into the two loop circuit computer code of Baker and Mann (LA-3548-MS). The resulting graph of the compression coil current is shown at (b). The oscillations superimposed on the L/R decay are due to currents ringing between the compression coil and the capacitor bank. The modulation arises because the inductance in the crowbar branch (3.39 nH) is not sufficiently small compared with the inductance of the compression coil (11.47 nH). The e-folding time of the crowbarred coil current is 55 μsec. The effect on the coil waveform of increasing the inductance in the crowbar branch, Fig. 94(c), by 60% is shown in Fig. 94(d).

The location of crowbar switches near the front of the collector plate was considered with a switch positioned in each collector plate skirt, 1 m behind the joint between the collector plate proper and the transition section to the coil. The schematic circuit diagram indicating the electrical parameters of this arrangement is shown in Fig. 95(a) and the compression coil current waveform is given in Fig. 95(b). With this geometry the inductance of the crowbar branch is one half that of the primary bank and the oscillations on the current waveform are considerably reduced compared with Fig. 94(b). The e-folding time of the current is 135 μsec. Figure 95(d) displays the coil current waveform that can be achieved if it is possible to place the switches just behind the coil transition section. The corresponding circuit schematic is shown in Fig. 95(c).

Scyllac Sector Parameters

No. of capacitor-spark gap units	216
Capacitor-spark gap inductance, nH	0.35
Capacitor-spark gap resistance, Ω	6.71×10^{-5}
Average cable length, ft	30.5
Cable inductance, nH	0.94
Cable resistance, Ω	2.59×10^{-5}
Cable cartridge inductance, nH	0.18
Collector plate inductance of primary bank feed section, nH	0.986
Collector plate transition section inductance, nH	0.545
Collector plate transition section resistance, Ω	3.04×10^{-5}
Collector plate resistance of primary bank feed section, Ω	5.40×10^{-5}
Coil inductance, nH	11.47
Coil resistance, Ω	2.36×10^{-5}

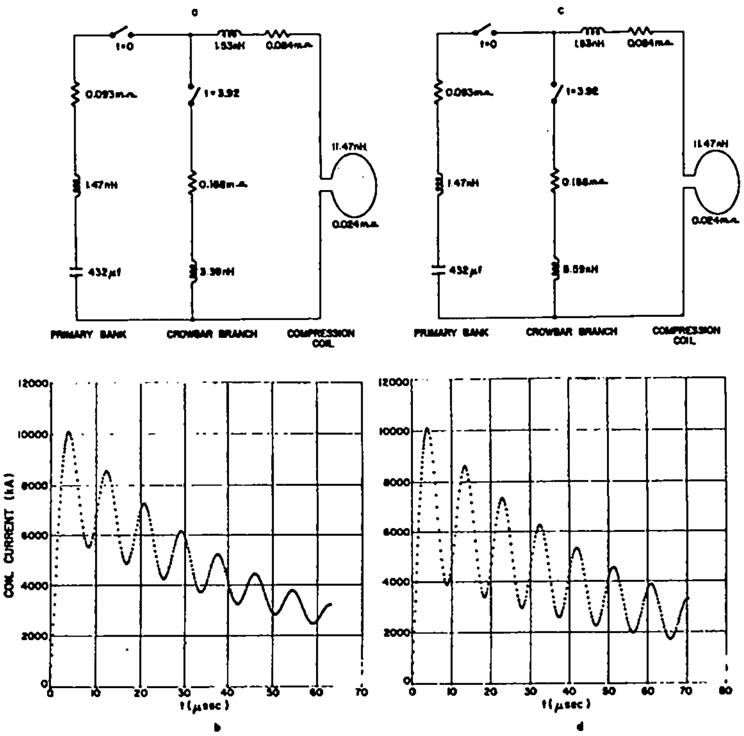

Fig. 94. Circuit diagrams (a) and (c) of one sector of Scyllac collector and coil system with different values of crowbar-switch inductance; (b) and (d) are corresponding coil current vs time.

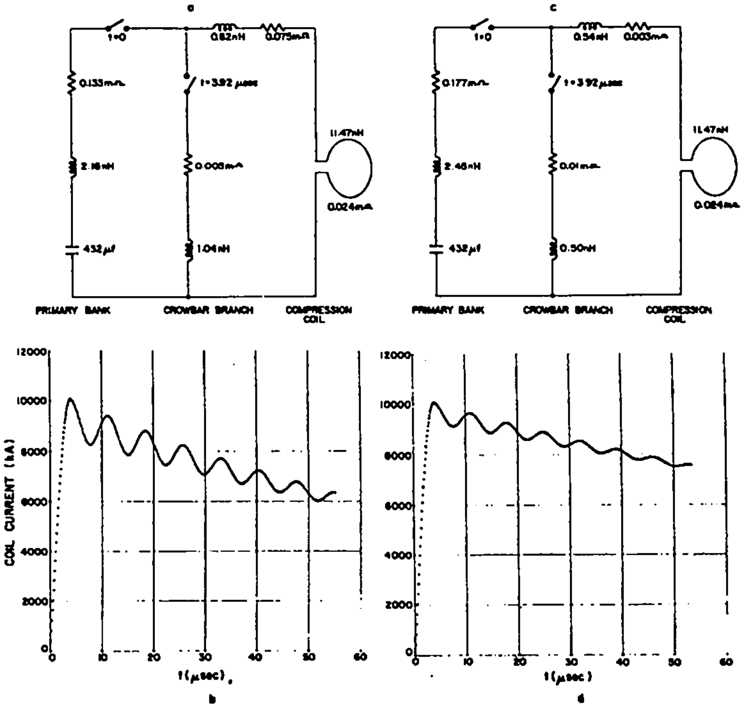

Fig. 95. Same as Fig. 94 except that crowbar switch is more closely coupled to the load coil (11.47 nH).

In order to realize an effective passive crowbar with exploding foil dielectric switches in the Scyllac system, it is essential that the switches be placed near the compression coil. It should be noted that the fractional modulation of the crowbarred load current is equal to the ratio of inductances in the crowbar and load branches of the circuit.

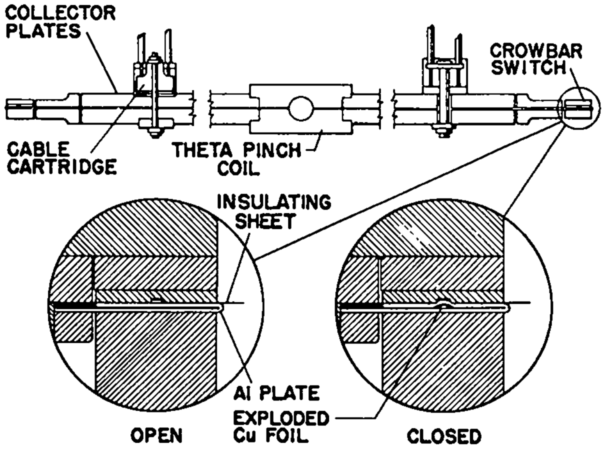

Fig. 96. Exploding-foil, dielectric switch in θ-pinch system.

EXPLODING-FOIL, METALLIC-CONTACT CROWBAR SWITCH

(V.A. Finlayson, G.A. Sawyer)

As was mentioned earlier, it is planned to use J. Marshall's exploding foil switch to crowbar Scyllac passively. This switch has now been developed further on the Scylla IA θ-pinch with promising results.

The experimental arrangement in Fig. 96 shows two-switches for the series capacitor bank arrangement. The oscillograms in Fig. 97 were obtained with the two switches carrying 1.5 MA with an e-folding time of 1.2 msec in the Scylla IA system without plasma. However, there is considerable modulation at early times of the crowbarred-coil current. This arises because of energy stored in the inductance of the crowbar switch (see preceding section). In the Scyllac design ways are being sought to minimize this effect. In further development, these switches will also be used to crowbar Scylla IV.

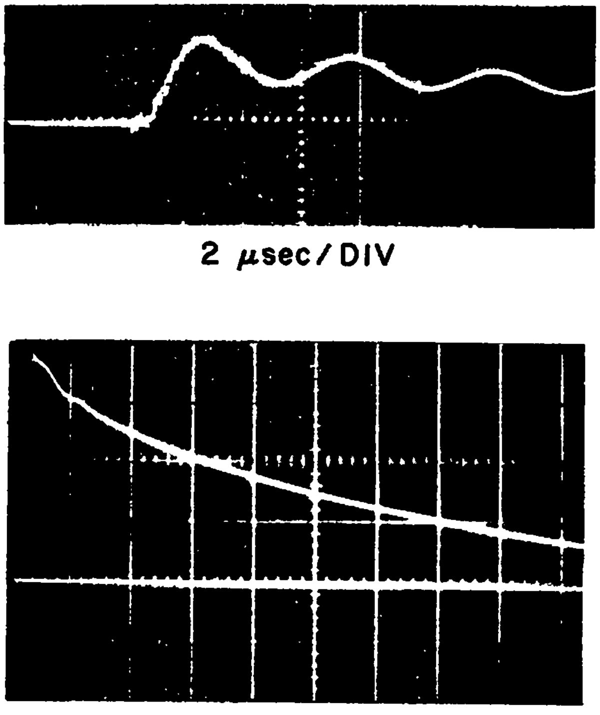

Fig. 97. Oscillograms of Scylla IA current crowbarred by exploding-foil switches.

SCYLLAC COLLECTOR PLATE STUDIES

(G. A. Sawyer, E. L. Zimmermann)

Resistive paper analog models of Scyllac collector plates have been used for studies of collector plate inductance and the curvature of the magnetic flux lines at the coil feed.

The resistivity of the paper used is 1.5 kΩ per square. The resistivity is about 10% anisotropic, but since current flow is largely in one direction this makes little difference. The inductance of the Scyllac collector plate, with a spacing of 0.2 cm is 2.52-nH per square. The ratio of these numbers, $K = 2.52/1.5 = 1.7$ nH/kΩ, relates inductance of the real Scyllac system to resistance in the model. Current feed to the paper model is through 108 thumb tacks representing cable cartridges. The thumb tack "cartridges" are supplied current from a dc power supply through resistors scaled to the proper inductance of the actual cartridges, feed cables, spark gaps, and capacitors. Since currents distribute themselves in the model as in the actual collector plate, measurements of the model resistance give equivalent values of system inductance in the real collector plate; equipotentials in the model represent magnetic flux lines in the real collector plate.

The modeling has one shortcoming for which it has been necessary to compensate. The paper, of fixed resistivity, can only model a collector plate of fixed spacing, but in the real collector plate there is an area around each cable cartridge of increased plate spacing. This feature has been simulated by punching four holes out of the paper around each thumb-tack cartridge. The hole size is calculated to increase the local resistivity to simulate the increased inductance of the real plate as closely as possible. Where the real plate has 3.5 times the inductance in the insulating hat area, holes are cut so that 1/3.5 of the area remains in the equivalent area of the paper. A similar problem occurs at the load coil. The coil may be regarded as a continuation of the collector plates with much larger spacing. This is simulated by extending a tab of paper out from the feed point until its resistance represents the correct coil inductance.

Four collector plates that have been considered are shown in Fig. 98. Scylla IV was used for comparison with three possible Scyllac collector plate designs: the Scyllac model I taper section with skirts, the Scylla model I taper section without skirts, and a wider Scylla model II taper section.

The results have some unexpected features. The first row gives the total source inductance, including collector plate, cartridges, cables, spark gaps, and capacitor bank. The inductance values are larger than have usually been assumed. A possible reason is that the effective inductance is difficult to calculate for a distributed current feed, and previous calculations have underestimated the funneling in of current just behind the coil feed point. The second row of the table gives a weighted value of collector plate inductance alone, obtained by subtracting the contributions of cartridges cables, spark gaps, and capacitors from the total feed inductance. Row 3 gives the calculated energy transfer efficiency of the system assuming a 10-nH load coil.

The fourth row shows the measured radius of curvature for the flux line just at the coil feed point, determined by fitting curved templates to measured flux lines and by trigonometric calculation from measured I_z and I_x components. Scylla IV has a surprisingly small 5-m radius of curvature, considering that plasma drift has never been observed.

The Scyllac Model I taper section with skirts also has a 5-m radius of curvature. This radius is not small enough to match the 2.5-m radius of the toroidal Scyllac nor is it correct for the linear pre-Scyllac where the radius should be infinite. Values for the Model I taper section without skirts are included to show the effect of the skirts. The Model II taper section in the last column fills nearly all the area around the torus and gives nearly the correct radius of curvature for the toroidal case. The radius is 3.2 m instead of the correct 2.5 m, probably because the coil-simulating tab of resistive paper tends to straighten out the field lines unrealistically.

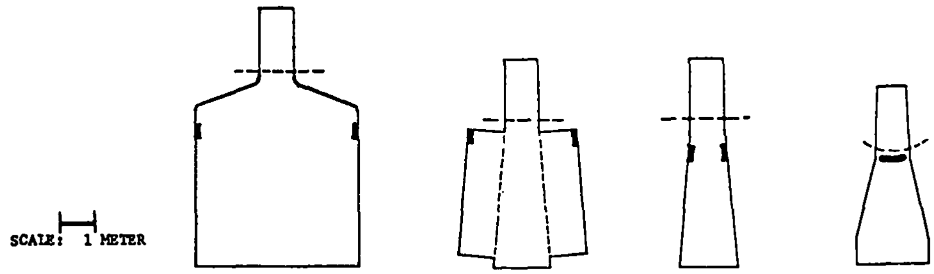

CASE:	SCYLLA IV	SCYLLAC MODEL I TAPER SECTION WITH SKIRTS	SCYLLAC MODEL I TAPER SECTION WITHOUT SKIRTS	SCYLLAC MODEL II MODIFIED TAPER
Source Inductance	3.8 nH	4.6 nH	5.5 nH	4.7 nH
Plate Inductance	2.7 nH	2.7 nH	3.6 nH	3.1 nH
Crowbar Inductance	3.5 nH	4.6 nH	3.5 nH	2.3 nH
Radius of Curvature (Flux line)	4.8 m	4.7 m	14.4 m	3.2 m
Transfer Efficiency	72%	70%	67%	70%
Percent Modulation with Crowbar	13%	32%	--	27%

Fig. 98. Four collector-plate models for which inductance and field-line curvature were determined.

Of course, 3.2 m (or the correct 2.5 m) radius would be bad for the linear pre-Scyllac but it is proposed to insert a 20-cm long straight transition section in the linear case. Measurements show that this will increase the radius of curvature to 9.4 m at a cost of 0.5 nH inductance.

Solid dielectric switch crowbars were simulated on each collector plate, the locations being indicated by heavy lines in Fig. 98. The measured inductance of all these crowbar systems is so large that there will be considerable modulation on the crowbarred waveform. Row 5 of the figure gives computer calculated modulation of the crowbarred load current for each case. The values given are peak-to-peak modulations.

COMPUTER FOR SCYLLAC DATA PROCESSING

(D.M. Weldon, A. S. Rawcliffe, G. A. Sawyer, F. L. Ribe)

It is certain that, in studying the operation of Scyllac, it will be necessary to record and analyze much more data (about 15 times more) than is now done on Scylla IV. With some 16 oscilloscope traces in active use on Scylla IV, the limit has almost been reached for reduction of data from photographs. In addition, there is a trend toward more complex diagnostic measurements which require more and more mathematical analysis of wave forms to reduce the data to usable form. This means that the data reduction process is so slow that results are unavailable for days and cannot be used to guide the operators in the next Scylla operations. In addition it is desirable to acquire and analyze data which indicate the operation of the numerous components of the capacitor bank itself in order to keep Scyllac running.

For Scyllac, computer acquisition and reduction of data will therefore be essential. Considerable effort has been put into determining the Scyllac computer requirements and on discussions of computers with computer manufacturers. A short report, LA-3713-MS, "Proposed Scyllac Computer System for Data Acquisition and Treatment," has been written. This report explains the need for a data processing computer, and outlines the job the computer should do. A second report is being prepared which gives in detail the Scyllac computer requirements in terms of the type and volume of input and output, and of the specific calculations required for each shot. It is hoped to have computer specifications written in the next several months and to procure the computer in FY-1969 in order to gain experience with it on Scylla IV before Scyllac starts operation.

In order to obtain a more reliable estimate of the amount of core and bulk storage needed and to define softwave requirements better for the computer a data acquisition program has been written in Fortran to serve as the foundation of the data acquisition program used with Scyllac.

The initial computer configuration is to be governed solely by Scyllac requirements, but it is desirable that the peripheral equipment needed to implement communications with the Los Alamos Central Computing Facility and multiple programming with other Sherwood groups be available. In general terms, the Scyllac computer should have the following minimum features:

1. Control Processing Unit (CPU) - basic cycle time 2 μsec or less, hardware multiply and divide, memory protection, parity checking, 8 K to 12 K words of magnetic core.

2. Cathode-Ray Tube Data Display (CRT) - 8 in. x 8 in. minimum usable space for raster, 1024 x 1024 addressable points.

3. Bulk Storage - magnetic tape, disk, or drum, or combinations of them to provide (a) storage of each day's data - 1 to 2 million 8-bit words which can be removed from the computer for permanent records storage and (b) storage of operational programs, etc.

4. Typewriter or Teletype - excluding teletype models 33ASR or 33KSR and similar light duty equipment.

5. Card reader or fast paper-tape equipment.

6. Software - time sharing monitor and Fortran compiler capable of compiling the sample data acquisition program.

7. Line printer for log book data or demonstrated ability to display log book data by some combination of CRT and typewriter.

8. Availability of peripheral equipment. If not provided with the initial computer configuration, the following equipment must be available along with interfaces for mating with the computer: (a) card reader 150 cards/min or better, (b) line printer 300 lines/min or better, (c) plotter, (d) IBM compatible magnetic tape, and (e) communications equipment. All equipment must be installable in the field and installation of one piece of equipment must not exclude installation of another.

SCAN CONVERTER DEVELOPMENT

(A.T. Brousseau, R.F. Gribble)

The need for a special computer interface to collect large amounts of data for the Scyllac experiment was discussed in the preceding section. A major part of this interface will be built around the scan-converter tube developed by J Division at LASL. A complete prototype interface using two to four of these tubes is being constructed for evaluation on the Scylla IV experiment. The digital output of this first unit is to be recorded on IBM cards.

The scan-converter tube consists of two independent, electrostatic deflection electron guns each pointing from one end towards a zinc sulfide semiconductor target near the tube midplane. One gun provides a "write" beam, the other, a "read" beam. By collecting write-beam secondary electrons from the target, information is stored on the target in the form of low-mobility holes. The written trace can be read up to about 72 h after writing by observation of secondary electrons created as the read beam scans the target. Writing is accomplished by conventional oscilloscope circuitry with the exception that capacitive coupling is utilized to reduce beam drift problems. A small, fixed-instruction, digital-type, logic circuit connected to the read side provides direct and automatic digital sampling of the written trace with an accuracy of one part in 512. The write-side amplifier bandwidth will be variable to be consistent with the effective sampling rate of each recorded signal.

The Scyllac scan-converter interface will consist of about 96 signal channels controlled by one master controller that will direct the reading of the scan converters following each Scyllac shot. The master controller will be under computer command. Six scan converters will be mounted by plugging into each of 16 relay racks. In each rack the scan converters will have common power supplies and one common read-logic circuit chassis. By changing one printed circuit card in the read-logic chassis and with the addition of a recorder controller and a recorder, it will be possible to convert a rack of scan converters for use in a manner independent of a computer on other experiments.

The read-logic chassis and an IBM card-punch controller circuit have been designed. An accuracy of 0.1% at a setting time of 150 nsec has been achieved on a breadboard version of the special digital-to-analog converter used in the read system. Several printed circuit cards have been constructed for the read chassis. Four scan-converter tubes are on hand, and most of the components for the write system for one tube have been purchased or constructed. During the next several months a single prototype should become operational and the problems associated with operation of the system will be studied.

DYNAMIC STABILIZATION FIELD EFFECTS IN SCYLLAC

(W.B. Riesenfeld)

To inhibit or suppress the high-β ballooning instability in a Scyllac bumpy torus equilibrium, it has been proposed to apply time-dependent magnetic fields polarized in the azimuthal direction, at right angles to the static θ-pinch field lying along the z-direction. The resulting oscillating electric field, which is parallel to the static magnetic field, is able to accelerate electrons in any tenuous plasma layer surrounding the dense plasma column to velocities capable of exciting electrostatic two-beam instabilities. The latter would then cause the buildup of microturbulence in the tenuous layer which could propagate into the central column. On the other hand, unless the highly conducting tenuous plasma is disrupted by microinstabilities, it would tend to shield out the dynamic stabilization field and prevent the latter's interaction with the central column. The spatial distribution of the oscillating fields have been calculated and the magnitude B_c of the critical field amplitude which would induce electrostatic instabilities in the skin layer of the central column has been estimated, taking into account the effects of electron collisions. Plasma density inhomogeneities are also taken into account insofar as they may be treated by a crude WKB method. The field distributions have also been calculated in a turbulent external plasma layer and the absorbed power level estimated.

For simplicity, a Cartesian coordinate system is used in which the z-axis coincides with the θ-pinch axis, the y-coordinate is along the instantaneous azimuthal direction, and the x-coordinate lies along the radial direction. The electron density n is assumed to depend only on x. The oscillating magnetic field has the form

$$B_y(x,t) = B_o \exp[i(kx - \omega t)],$$

where ω is the applied angular frequency and k is the radial wave number, in general complex, of the dynamic field. Since the induced electric field is parallel to the static magnetic field, the only relevant component of the conductivity tensor is the parallel component $\sigma_\parallel$, relating the z-components of current density and electric field. By solving the linearized electron transport equation with a Langevin collision term, and assuming a homogeneous density distribution, it is found that

$$\sigma_\parallel = \sigma_r + i\,\sigma_i,$$

$$\sigma_r = \frac{ne^2\tau}{m} \quad \frac{1}{1+\omega^2\tau^2}$$

$$\sigma_i = \frac{ne^2}{m\omega} \quad \frac{\omega^2\tau^2}{1+\omega^2\tau^2} \quad ,$$

where e and m are the electronic charge and mass, respectively, and τ is the mean time for an electron to undergo a 90° deflection (the momentum transfer collision time). By solving Maxwell's equations with these conductivity parameters the wave number of the dynamic field is found to be of the form

$$k^2 = \frac{\omega^2}{c^2} - \frac{\omega_p^2}{c^2} \quad \frac{\omega\tau}{1+\omega^2\tau^2} \; (\omega\tau - i),$$

where ω_p is the electron plasma frequency. The skin depth s is then given by

$$s = [\mathrm{Im}(k)]^{-1} .$$

For the cases of interest $\omega << \omega_p$, and in this limit

$$s = \frac{c}{\omega_p} \; \{2(1+\omega^2\tau^2)\,[(1+\frac{1}{\omega^2\tau^2})^{\frac{1}{2}} - 1]\}^{\frac{1}{2}}.$$

It is easily verified that this form provides the correct limiting values for both the collisionless ($\omega\tau \to \infty$) and collision-dominated ($\omega\tau \to 0$) cases. It is instructive to evaluate the skin depth s_o in the collisionless limit for the case that the density varies linearly with distance x over a sheath thickness Δ. Then

$$n(x) = \begin{cases} \frac{x}{\Delta}\, n_{max}, & 0 \le x \le \Delta \\ n_{max} & , \; x > \Delta . \end{cases}$$

The average value of n within the skin depth s_o (for $s_o < \Delta$) is given by

$$n_{av} \cong \frac{s_o}{2\Delta} n_{max},$$

so that in the limit $\omega\tau \to \infty$,

$$s_o \cong c \left[\frac{m\Delta}{2\pi e^2 n_{max} s_o} \right]^{\frac{1}{2}} .$$

Solving for s_o the result is that obtained by Furth,[1] namely,

$$s_o \cong \left[\frac{\Delta}{2\pi r_c n_{max}} \right]^{\frac{1}{3}} ,$$

where $r_c = e^2/mc^2$ is the classical electron radius.

For the electron temperature and densities applicable to the Scylla IV column, however, the average value of $\omega\tau$ in the sheath is of order 0.2, so that in fact the collision dominated case is of greater interest. The collision-dominated skin depth s_1 is obtainable directly from the general form of s by taking the limit $\omega\tau << 1$ because the result is a function only of the product $n\omega\tau$ which is independent of x except for a small logarithmic contribution which may be neglected. Thus,

$$s_1 \cong [2\pi r_c n\omega\tau]^{-\frac{1}{2}} .$$

To estimate the critical field strength amplitude B_c above which the electrons are able to excite electrostatic instabilities, the velocity v_z parallel to the static field acquired by the electrons is calculated and a simple Penrose criterion is applied for the upper permissible bound of $|v_z|$. The result is

$$v_z(x,t) = -\frac{eB_o}{mc} \frac{\omega\tau}{k(1-i\omega\tau)} \exp[i(kx - \omega t)],$$

and, after some algebra,

$$|v_z| = \frac{eB_o s}{mc} F(\omega\tau) \exp\left(- \frac{x}{s}\right),$$

where

$$F(\omega\tau) = \frac{\omega\tau}{(1+\omega^2\tau^2)^{\frac{3}{4}} \{2[(1+\omega^2\tau^2)^{\frac{1}{2}} - \omega\tau]\}^{\frac{1}{2}}} .$$

The collisionless and collision-dominated limits are obtained by taking the corresponding forms for s and using the formulas

$$\lim_{\omega\tau\to\infty} F(\omega\tau) = 1,$$

$$\lim_{\omega\tau\to 0} F(\omega\tau) = \frac{\omega\tau}{\sqrt{2}} .$$

The condition that no microturbulence be generated locally is

$$|v_z| \le \alpha v_e,$$

i.e., the induced directed velocity amplitude must be less than some fraction α of the electron thermal speed v_e. It is clear from the spatial dependences of the oscillating magnetic field and the electron density that the closer the approach to the low density edge of the sheath the more likely it becomes that this criterion is violated. It is therefore reasonable to define a critical field amplitude B_c such that the criterion just holds with the equality sign at the edge x = 0. It follows that

$$B_c = \frac{\alpha v_e mc}{es(\omega\tau)F(\omega\tau)} ,$$

where the product $\omega\tau$ must be interpreted as a suitably averaged quantity. In the collisionless limit Furth's critical field formula is obtained;[1] in the collision-dominated limit, which turns out to be a reasonable approximation for the Scylla IV parameters almost to the very sheath edge, the result is

$$B_c \cong \frac{\alpha c \sqrt{6m T_e}}{es_1 \omega\tau} ,$$

where T_e is the electron temperature in energy units. Scylla IV parameters and a dynamic field frequency of 1 MHz yield a critical field value of

$$B_c \cong 24\alpha \text{ kG}.$$

From the form of the collisionless expression for B_c it might be concluded that any increase in s would lead to a decrease of the critical field value. However, if collisions are responsible for broadening the skin depth this conclusion is erroneous, as may be seen from the expansion of the product $s(\omega\tau)F(\omega\tau)$ in the almost collisionless limit to lowest order in $1/\omega\tau$:

$$s(\omega\tau)F(\omega\tau) = s_0 \left[1 - \frac{1}{4\omega^2\tau^2} + \dots \right] .$$

Thus, the direct effect of electron collisions is to increase the critical field even in the collisionless limit.

If the collisionless formulas are applied to the tenuous external plasma layer, it is found that, for reasonable field values $B < B_c$, this layer will be turbulent, even though the main column is stable. In this case the effective collision time τ', which enters into the conductivity tensor, will be the mean time for the electrons to lose their directed momentum in interacting with the turbulent spectrum of plasma fluctuations. This time is of order $(\omega_{pi}\omega^2_{pe})^{-\frac{1}{3}}$, where ω_{pi} and ω_{pe} are the ion and electron plasma frequencies, and the plasma conductivity becomes very small compared to that of the central column. It is of interest to determine the energy deposition rate in the external plasma layer for this case. Let the distance between the outer wall and the surface of the dense plasma column be L, and assume that $\Delta/L \ll 1$; for simplicity, perfectly conducting boundary conditions at the surface are assumed. If the radial coordinate x is redefined so that the outer wall and dense plasma surface are located at $x = 0$ and $x = L$, respectively, then the field distributions turn out to have the form

$$B_y(x,t) = \gamma\{\exp(-\varkappa x)\cos(\varkappa x-\omega t)+ \exp[\varkappa(x-2L)]\cos[\varkappa(x-2L)+\omega t]\}$$

$$E_z(x,t) = \gamma \frac{\omega}{c\varkappa\sqrt{2}} \{ \exp(-\varkappa x) \cos(\varkappa x-\omega t + \frac{3\pi}{4})$$

$$- \exp[\varkappa(x-2L)] \cos[\varkappa(x-2L) + \omega t - \frac{3\pi}{4}]\},$$

where

$$\varkappa = \frac{\omega_{pe}}{c} \left(\frac{\omega\tau'}{2}\right)^{\frac{1}{2}}$$

and it has been assumed that $\omega\tau' \ll 1$, $\omega/c \ll \varkappa$. The constant γ gives the magnetic field amplitude B_0 at the outer wall through the relationship

$$B_0 = \gamma[1 + \exp(-4\varkappa L) + 2 \exp(-2\varkappa L) \cos(2\varkappa L)]^{\frac{1}{2}} .$$

The power per unit volume absorbed by the plasma is given by

$$\frac{dU}{dt} = j_z(x,t)\, E_z(x,t),$$

and the energy absorbed per unit volume per cycle is

$$\Delta U = \int_0^{2\pi/\omega} dt \frac{dU}{dt} .$$

Using the appropriate form of the conductivity tensor, and performing a somewhat tedious but straightforward calculation, the result is

$$\Delta U = \frac{1}{2}\gamma^2 \exp(-2\varkappa L) [\cosh 2\varkappa(L-x) - \cos 2\varkappa(L-x)].$$

The contemplated parameters of Scyllac lead to a numerical value for $(\varkappa L)^2$ of order 0.01, and the expressions may therefore be simplified by taking the limit $\varkappa L \ll 1$, when

$$\Delta U \cong 2\gamma^2\varkappa^2(L-x)^2$$

is obtained. By integrating this quantity, and also the energy density stored in the field, over the plasma volume the Q (proportional to the ratio of stored field energy to energy absorbed per cycle) of the equivalent damped circuit may be constructed in the usual fashion. The result is of the form

$$Q \cong \frac{3}{2(\varkappa L)^2}, \quad \varkappa L \ll 1.$$

Numerically, Q is of the order 150 for nominal Scyalla parameters.

The limit $\varkappa L \ll 1$, describing the case in which the oscillating field has very small penetration depth compared to L in the external tenuous plasma, is also of theoretical interest. It can be shown that in this limit Q approaches the constant value 0.5, the $\varkappa L$ dependence disappearing entirely from the expression. This is the limit in which the energy dissipated per cycle in the turbulent medium is of the same order as the stored field energy, and is clearly not applicable to the Scyllac regime.

Reference

1. H. P. Furth, "Dynamic Stabilization with Oscillating Electric Fields Parallel to a Static Magnetic Field." Personal communication, Aug. 3, 1966.

HOLOGRAPHY

(F. C. Jahoda)

Interferograms

Double-exposure holograms resulting in the analogue of Mach-Zehnder interferograms with the test and comparison beams separated in time rather than space, were described in LA-3628-MS (p. 42), at which time the method had been demonstrated on an exploding wire. Shortly afterwards the technique was successfully demonstrated on Scylla I and a full account published.[1] Apart from applying recently established holographic techniques to a plasma, the main innovation was the use of a hollow wedge with an exchange of gas filling between the two exposures of plasma and no plasma in order to introduce a straight fringe background. As a consequence, (a) plasma density generating only a phase shift less than π radians can be detected and measured and (b) spurious phase changes between exposures due to vibration alter only the spacing and inclination of the background and cannot be falsely attributed to plasma.

A schematic of the experimental arrangement is shown in Fig. 99. The 1/64-in. aperture pinhole is essential to give sufficient spatial coherence so that the reference beam path need only be equal to the scene beam path to within a few centimeters. An alternative arrangement is to place the diffuser after the plasma and eliminate the imaging lenses. The ability to view the plasma interferometrically from several directions with the same double

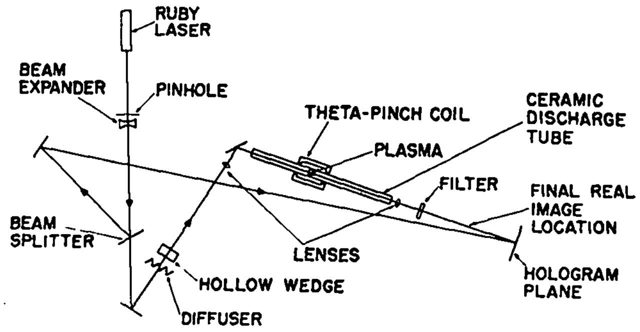

Fig. 99. Schematic of experimental arrangement for holographic interferograms.

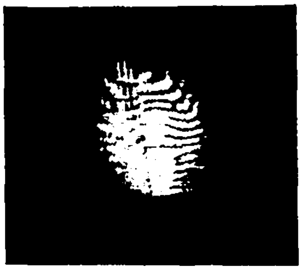

Fig. 100. Holographic interferogram.

exposure hologram is thereby lost, but further simplicity is gained in alignment and in the ability to use a narrow-band interference filter in the collimated laser beam to discriminate against the plasma luminosity.

A typical interferogram is given in Fig. 100. Over half the field of view a half cylinder of a quartz discharge tube has been inserted to simulate side-on observation. The cylindrical lens distortion and striations due to the quartz are apparent, but the plasma fringe structure is unimpaired.

The ability to use any type of window, including those of low optical quality, is the chief advantage of double-exposure holography over conventional Mach-Zehnder interferometry. Other advantages are (a) the unfolding of depth information from various views of one hologram, (b) ease of alignment, and (c) elimination of need for an interferometer capable of spanning the discharge.

Faraday Rotation

Holography can be utilized to give two-dimensional space resolution combined with photoelectric detection for a given instant of time on Faraday rotation measurements of plasma. Using two reference beams with polarizations at $+45^{\circ}$ and -45°, respectively, to the scene beam polarization, two simultaneous holograms are produced containing the desired information as intensity differences. Reconstructing them alternately in the same spatial location by suitable mechanical chopping of two reconstruction beams permits use of a fiber-optics photomultiplier combination to extract the intensity differences by quasi-dc means. The need for quantitative intensity measurements, rather than the qualitative pictorial nature required of holography in the interferometry work makes this application more difficult. It was demonstrated that the method was able to sense controlled 1° rotations but the scatter in intensity ratios shot-to-shot was too large to be applied to the Scylla plasmas of interest. Primary limitations are uncontrolled differences in the coherence lengths of consecutive ruby laser discharges needed for a plasma-rotation and no plasma - no rotation hologram pair and noise contribution from the hologram emulsion. This project was put aside in order to pursue other applications, but the real limits have not yet been thoroughly explored.

Moiré-Schlieren

Current work is concentrated on a refractive index gradient measurement, with which it is intended to study the early shock heating phase of Scylla IA. The method divides naturally into two distinct parts; first, a hologram is made with a giant pulse ruby laser during the plasma discharge, and then, in the reconstruction with CW gas-laser light at any later time, some schlieren-type optics are installed. This has the advantage that the sensitivity can be chosen, perhaps different sensitivities for different parts of the field, density gradients can be viewed along any transverse direction and, in general, the detection system can be optimized for the particular distortion already recorded. Separate discussions of these two parts, and demonstration on a test object are given below.

The holographic recording is somewhat different in significant ways from that described previously for holographic interferometry. An advantage is that only a single exposure is required, so that there is no problem in this instance of slight movements between exposures (as before, the 30-nsec duration of the giant pulse makes any movement during exposure negligible). A considerable disadvantage, however, is the inability in the present technique to use a diffuser in the scene beam, since it is desired to reconstruct the primarily collimated laser beam with only the slight angular deviations imposed by the refractive gradients. This implies also schlieren quality windows (no side-on viewing through cylindrical discharge tubes) and one-to-one correspondence between object and hologram plane, rather than spreading the information from each object point over the entire hologram. This means, further, that the hologram itself can be a source of schlieren during the reconstruction, and it has been found that photographic plates are much superior to photographic film in being free of such distortions.

Since the available high-resolution plates (649F) are about three orders of magnitude slower than the film (S0243) used for holographic interferometry, some important changes were necessary to get sufficient exposure with one giant pulse. These are: (a) use of a TRG-302 amplifier-oscillator G.P. laser instead of the TRG-104 oscillator G.P. laser, (b) doubling the pinhole size used for mode selection, but thus requiring more care in equal path length between scene and reference beams for sufficient coherence, (c) presensitizing the plates with triethanolamine, and (d) post-exposure to bring out the latent image. This procedure results in sufficient photographic density, which, finally, is bleached to remove the silver, leaving the information coded in a "phase" hologram by virtue of thickness variations between developed and undeveloped portions of the emulsion.

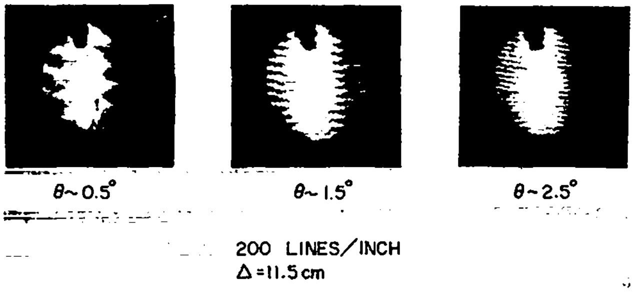

Fig. 101. Reconstructions from one hologram ; moiré plates installed with different relative angle (θ) between rulings.

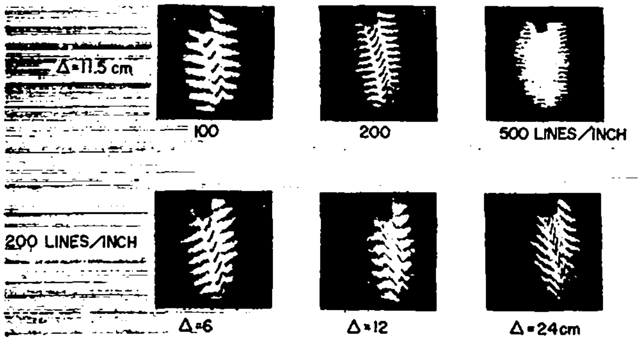

Fig. 102. Reconstructions of same hologram as in Fig. 101. (Upper: moiré plates with different ruling spacings; lower: different separations in one set of plates.)

The schlieren content of the reconstructed wavefront can be displayed in principle by any standard means. The decision was made to concentrate initially on moiré plates, which seem not to have been exploited very much before, although they make for extremely simple alignment and offer quantitative measurement of angular deflection with easily variable sensitivity. Two such plates having equispaced parallel rulings are inserted in the reconstructed wavefront some distance apart and the moiré fringe spacing adjusted for convenient viewing by the relative rotation of the plates. An angular deviation in any part of the field sufficient to displace the projection of a particular ruling of the first plate onto the ruling on the second plate that neighbors the ruling that would have been intersected by the absence of angular deviation results in a local shift of the moiré pattern by one fringe. There is consequently a considerable magnification effect which can be displayed on a diffuser past the second plate or recorded on film. Since the rulings of the two plates are nearly parallel for convenient fringe spacing and the moiré fringes run perpendicular to the rulings the fringe deviation is proportional to the density gradient along the direction of the undisplaced fringe. The important parameters to adjust the sensitivity are the separation distance between the plates and the spacing of the rulings themselves. It is desirable to limit displacements to about one fringe to avoid the appearance of higher order moiré fringes.

The technique is illustrated in Figs. 101 and 102. All the frames are reconstructions of a single hologram made with a giant pulse laser and differ only in moiré plate adjustment. The test object to simulate a plasma is a stream of SF_6 from a nozzle. In Fig. 101 the relative rotation

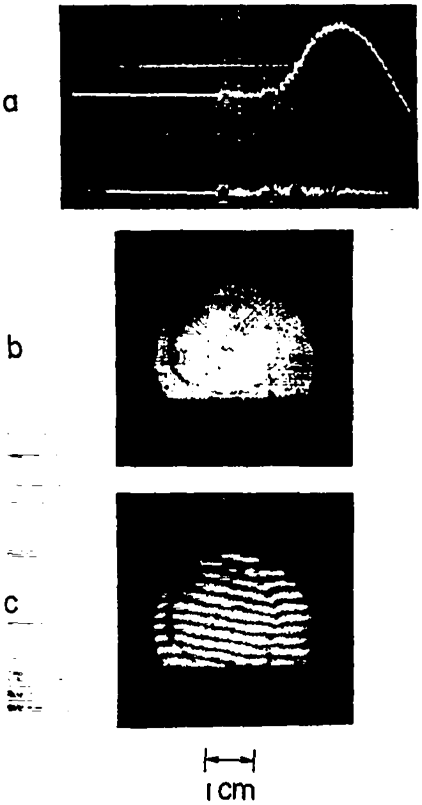

Fig. 103. (a) Laser giant pulse timing (bottom) relative to magnetic field (top). (b) Reconstruction of hologram; cross-hairs mark center of discharge tube. (c) Reconstruction of hologram seen through moiré plates (100 lines/in. at 12-in. separation).

of the moiré plates is varied, changing the fringe spacing but leaving the deviation as measured in fringes constant. In Fig. 102 top, the finesse of the rulings is varied whereas in Fig. 102 bottom, the spacing between the plates is varied. In both cases the fringe deviation is proportional to the changing parameter.

The combination of the maxima of the parameters shown here, 500 lines/in. at 24-cm separation, gives a displacement of one fringe for an angular deviation of 2×10^{-4} radian. The hologram was recorded on film rather than on plate and a general waviness of the fringes caused by the film substrate limits the fractional fringe deviation that could be detected. The evidence indicates that for holograms on plates the ultimate sensitivity is currently limited by the quality of the rulings themselves, which are derived from printing screens. Other sources for rulings will be tried and it seems probable that another order of magnitude at least can be gained to increase the sensitivity to 10^{-5} radian. The angular deviation ϵ (radians) for a density gradient dn/dx ($\mathrm{cm}^{-3}/\mathrm{cm}$) over a path length Δx(cm) is given by

$$\epsilon = 2.1 \times 10^{-22} \frac{dn}{dx} \Delta x.$$

It remains to be seen how well this technique competes in practice with the well-known schlieren methods that rely on intensity variations produced by knife edges.

The initial attempt on Scylla IA is shown in Fig. 103. The bank, driving two half-turn coils in series, was charged to 35 kV, with 1 kG reverse bias field, preionization, and 100-μ filling pressure. The lower oscilloscope trace in Fig. 103(a) shows the timing of the ruby laser giant pulse relative to the magnetic field signal on the upper trace. Figure 103(b) is a photograph of the reconstructed hologram in gas laser light without any additional optical components. It is, therefore, a shadowgraph, as it could have been recorded directly on film in the collimated ruby laser beam, with the dark circle outlining the maximum of the second derivative of the density. The diffraction pattern of the cross-wires marks the center of the discharge tube. (The hologram itself was not well centered.) Figure 103(c) is a reconstruction viewed through moiré plates (100 lines/in.) at 12 in. separation, giving 8×10^{-4} radian for one fringe displacement.

Reference

1. "Fractional-Fringe Holographic Plasma Interferometry," by F. C. Jahoda, R.A. Jeffries, and G. A. Sawyer, Appl. Optics 6, 1407 (1967).

CALCULATIONS OF MAGNETIC ENERGY STORAGE OF THE PLASMA FOCUS

(D. A. Baker)

Introduction

Further exploitation of the plasma focus experiments involves the optimization of the energy deposited in the pinch. The idea of maximizing the energy stored inside the machine in close proximity to the plasma to be heated has had a number of advocates for some time. With the stored energy inside the vacuum vessel the high voltages associated with a rapidly changing plasma inductance are kept in the plasma regions instead of at outside terminals where insulation problems appear. Close proximity minimizes the communication time between the pinch and the region of stored energy. The results reported here are concerned with maximizing the fraction of the initial capacitor energy which is stored in the internal magnetic field at the time the moving current sheet reaches the end of the electrode (i.e., at the time of onset of the pinch).

Problem

It has been observed experimentally at LASL that, after a small acceleration period, the inductance rises almost linearly with time up to the onset of the pinch. This effect corresponds to a constant velocity current sheet moving along the electrodes, and leads to a consideration of the energy stored in an RLC circuit having a linearly varying inductance.

In the circuit shown in the inset of Fig. 105, the capacitor bank C, initially charged to a voltage V, is discharged through a constant external inductance L_e in series with the linearly varying inductance L which represents internal inductance associated with the moving current sheet. The calculation also allows a constant series resistance R. The time rate of change of L is related to the sheet velocity by

$$\dot{L} = 0.002\, v \ln(r_2/r_1) \quad \mu\Omega,$$

where v is the constant sheet velocity in cm/sec and r_1 and r_2 are the radii of the inner and outer electrodes. The problem is to determine the current and the maximum stored field energy as functions of the circuit parameters.

Solution and Results

The circuit equation is

$$(L_e + \dot{L}t)\frac{dI}{dt} + I(R + \dot{L}) + \int_0^t \frac{I}{C}\, dt = V \qquad (1)$$

with the initial condition

$$I(0) = 0. \qquad (2)$$

It is possible to obtain a solution to Eq. (1) in terms of Bessel functions of the first kind J_k; thus,

$$\frac{I(t)}{I_m} = \left(\frac{\alpha}{\omega}\right)^k \frac{[J_k(\alpha)\ J_{-k}(\omega) - J_{-k}(\alpha)\ J_k(\omega)]}{[J_{k+1}(\alpha)\ J_{-k}(\alpha) + J_{-k-1}(\alpha)\ J_k(\alpha)]}, \qquad (3)$$

where

$$k = 1 + (R/\dot{L})$$

$$\alpha = R_c/\dot{L}, \ R_c = 2\sqrt{L_e/C}$$

$$\omega = \sqrt{\alpha(\alpha + 4\pi t/\tau)} \qquad \tau = 2\pi\sqrt{L_e C}$$

$$I_m = V\sqrt{C/L_e}.$$

In the event k is an integer, the Bessel functions with negative indices become Bessel functions of the second kind. The current (in units of $I_m \equiv V\sqrt{C/L_e}$) as a function of time (in units of $\tau \equiv 2\pi\sqrt{L_e/C}$) is plotted for various values of the dimensionless parameter $\dot{L}/R_c$ $(= \frac{1}{2}\dot{L}\sqrt{C/L_e})$ in Fig. 104 for the case R = 0. Both the damping and the increasing period due to the changing inductance are apparent.

The peak fractional magnetic energy stored internal to the machine, i.e., $\frac{1}{2} L I^2/(\frac{1}{2}CV^2)$, and the corresponding quantity for the total magnetic energy are plotted vs the parameter $\dot{L}/R_c$ in Fig. 105. The peak internal fractional magnetic energy rises rapidly with $\dot{L}/R_c \simeq 0.7$ and then decreases very slowly for higher values of the parameter. The times these maxima occur are plotted in Fig. 106. Thus if the assumptions of constant sheet velocity and negligible R are valid, the maximum in the stored internal magnetic

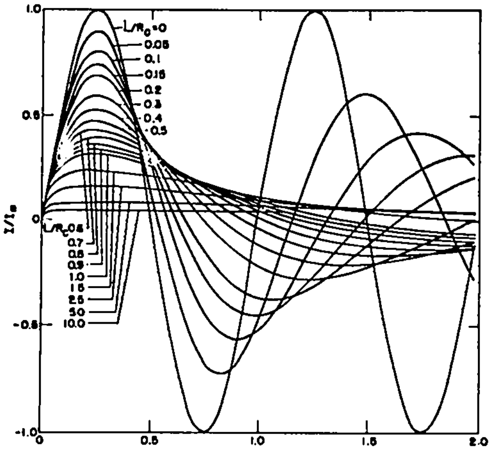

Fig. 104. Current vs time (for units see text) for series RLC circuit containing a linearly varying conductor for R = 0.

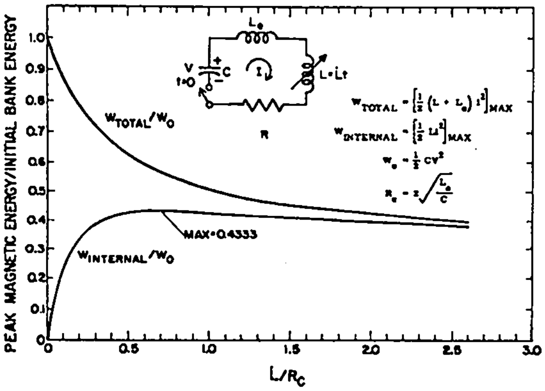

Fig. 105. Peak magnetic energy storage vs $\dot{L}/R_c$ for R = 0.

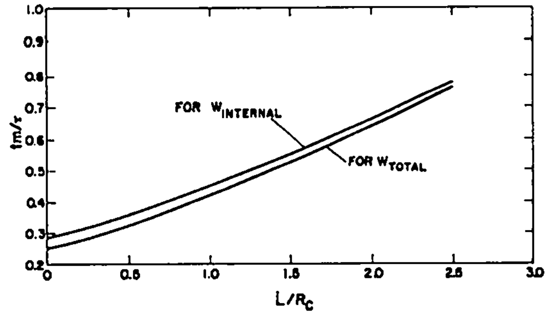

Fig. 106. Time for peak energy (internal and total) vs $\dot{L}/R_c$ for R = 0.

energy occurs when the parameters of the experiment are adjusted so that the sheet velocity yields an $\dot{L}$ which is ~ 0.7 of the critical damping resistance of the external circuit. Under these conditions the maximum internal stored field energy is obtained when the constant sheet velocity is given by

$$v = \frac{700}{\ln(r_2/r_1)} \sqrt{L_c/C} \text{ cm}/\mu\text{sec}. \qquad (4)$$

It is of interest to apply these theoretical results to the Los Alamos Dense Plasma Focus Device (DPF-1) whose parameters are L_e = 16 nH, C = 90 μF, r_1 = 2.5 cm, r_2 = 5 cm, and an observed $\dot{L} \simeq$ 15 mΩ. For these quantities R_c = 27 mΩ and $\dot{L}/R_c$ = 0.56. Figure 105 shows that about 43% of the stored capacitor energy appears in internal magnetic field energy. Since this is near the peak of the curve, not much is to be gained by juggling $\dot{L}$ or R_c as far as internal stored energy is concerned. The distance the current sheet has traveled at the time t_m, where LI^2 is maximum, can be calculated. From Fig. 106, this maximum occurs at $t/\tau \sim 0.37$; and since τ = 7.5 μsec, t_m = 2.8 μsec; the velocity from Eq. (1) is 11 cm/μsec. Hence, the current sheet has traveled 11 x 2.8 = 31 cm at the time the internal stored energy is maximum. The actual DPF-1 device has an electrode length of 17 cm. If the internal stored energy at the time of focus is of prime importance, this calculation would indicate that the electrode length should be nearly doubled.

On the other hand, if very little plasma is left in the annulus between the electrodes behind the current sheet, so that signal transit times are short, and if insulation is good enough, the additional magnetic energy stored externally can be called upon during the pinch and the situation is different. Figure 105 shows that $\dot{L}/R_c$ should be minimized in order to enhance the total stored magnetic energy. This increase in stored magnetic energy can be accomplished by decreasing C, v, and r_2/r_1 and increasing V and L_e. Since the pinch formation would be enhanced by larger currents, it appears advisable to keep L_e low and to decrease $\dot{L}/R_c$ by varying the remaining parameters. If the total magnetic storage is to be optimized at the time of pinch, Fig. 106 shows that for a given sheet velocity the total energy peaks earlier in time than that stored internally and a correspondingly shorter optimum electrode length is implied.

Magnetic energy storage is, of course, not the only factor when it comes to maximizing the energy actually dumped into the pinch. In particular, the pinch dynamics, which were not considered here, are involved.

LAGRANGIAN PARTICLE APPROACH TO THE THETA PINCH IMPLOSION

(T. Oliphant)

For almost a decade (see K. Hain[1] for a bibliography) the plasma dynamics involved in the θ-pinch implosion have been treated numerically by using collision dominated, i.e., quasiequilibrium magnetohydrodynamics (MHD). Many reasonable comparisons with experiment have been made, but a disturbing fact is that, as the plasma is made to approach thermonuclear conditions, the ion-ion collision time becomes longer so that the collision-dominated MHD should be less reliable. Therefore, it seems reasonable to investigate methods of solving plasma transport theory to get a better representation of the nonequilibrium behavior of the plasma.

During the past year a model θ-pinch problem has been set up that does not assume ion-ion collisional equilibrium. The ions are made to simulate an ion Vlasov equation by applying to the ions the Lorentz force resulting from the applied electromagnetic field. The electrons are assumed to behave like a fluid which follows the average motion of the ions in such a way as to maintain charge neutrality. The electron current is assumed to dominate the ion current and the field penetration and shielding currents are obtained by solving Maxwell's equation using Spitzer's resistivity inside the plasma. The $\vec{j} \times \vec{B}$ force and the electron pressure are transmitted to the ions by means of the electric fields which are assumed to maintain charge neutrality.

The first program set up was a two-dimensional (r, z) θ-pinch with a mirror coil. This program proved the feasibility of calculating the effect of a mirror coil on end losses.

The second program set up was a one-dimensional (r) θ-pinch. The purpose was to check the behavior of the model against experimental results. The general nature of the dynamics was found to agree with experiment and with previous MHD calculations. However, one point was noted that has perhaps not been looked for very extensively in experiments. In the case of zero bias, enough magnetic field leaks through the current sheath so that a large magnetic field spike is produced in the center of the plasma at peak compression. It is not clear at present just how real this spike is.

Reference

1. K. Hain, Proc. APS Topical Conference on Pulsed High-Density Plasmas, 1967, LA-3370, F1.

THE QUANTUM THEORY OF EXPLICITLY TIME-DEPENDENT INVARIANTS AND ITS APPLICATION TO THE TIME-DEPENDENT HARMONIC OSCILLATOR

(H. R. Lewis and W. B. Riesenfeld)

A theory of explicitly time-dependent, Hermitian invariants for one-dimensional quantum systems has been devised in which the eigenstates of such an invariant are used to construct explicitly a complete set of solutions of the time-dependent Schrödinger equation. Each eigenstate of the invariant is related to a particular solution of the Schrödinger equation by a time-dependent gauge transformation; the gauge functions are found by solving simple first-order differential equations. The theory has been applied to the class of exact invariants for quantum time-dependent harmonic oscillators that has been discussed recently.[1,2]

In particular, the situation has been considered in which the frequency function of the oscillator is constant in the remote past and future, and exact formulas for the transition amplitudes between energy eigenstates in the remote past and future have been calculated. The usual results of the adiabatic and sudden theories of quantum mechanics have been exhibited as special cases of the exact formulas. Also, the existence of a large class of time dependences have been demonstrated for which the adiabatic result obtains after the transition, even though the adiabatic condition does not hold during the transition. An article describing this work is in preparation.

References

1. H. R. Lewis, Jr., Phys. Rev. Letters 18, 510 (1967); erratum in ibid., 18, 636 (1967).

2. H. R. Lewis, Jr., "A Class of Exact Invariants for Classical and Quantum Time-Dependent Harmonic Oscillators," To be published.

HYDROMAGNETIC EQUILIBRIUM OF A THIN-SKIN, BUMPY, TOROIDAL PLASMA COLUMN OF ARBITRARY BETA

(W. B. Riesenfeld, J. L. Johnson*, R. L. Morse)

An analytic formulation of the toroidal equilibrium of a thin-boundary, hydromagnetic, bumpy plasma column of arbitrary β has been developed for the purpose of augmenting numerical studies and to provide engineering estimates for the magnitudes of the external confining multipole currents required in a toroidal Scyllac device. In the $\beta = 1$ limit the results correspond to a Meyer and Schmidt type of equilibrium with no net toroidal currents. The analysis involves perturbation theory in the reciprocal of the toroidal aspect ratio; the equilibrium conditions impose an ordering in which the reciprocal aspect ratio is of second order with respect to the deviations from a toroidal cylinder of the equilibrium interface. The rippling of the field lines, achieved by superpositions of external multipole fields, is an essential feature of this equilibrium, which thus differs qualitatively from a Stellarator equilibrium in which the rotational transform plays a dominant role. In the limit of $\beta = 1$ and for an unperturbed toroidal plasma column of circular cross section, the equilibrium conditions require the rotational transform to vanish.

The equilibrium is macrounstable, no matter what model is used to investigate the stability. Growing modes appear which develop preferentially in the outward bulging ripples of the field lines. On the other hand, the hydromagnetic estimates of the growth rates are pessimistic in comparison with those of the $\beta = 1$ bounce model theory; if the latter estimates are valid the system can in principle be stabilized dynamically, although the full implications of such arrangement have to be studied experimentally and theoretically. In addition, the present equilibrium may suffer from the requirement of field line closure; in the low-β limit, at least, small field errors within a certain range lead to enhanced particle loss much like Bohm diffusion, independent of the magnitude of the errors. The effect of rotational transform on the nature of an intermediate-β equilibrium is being considered.

Almost nothing is known about the microinstabilities which may occur. Knowledge of detailed particle distributions in phase space for ions and electrons would be needed to replace the hydrogmanetic averages before such problems can be attacked.

---

*Princeton University Plasma Physics Laboratory, on leave from Westinghouse Research Laboratories.

MAGNETIC MOMENT SERIES

(H. R. Lewis)

In an attempt to understand better the nature of adiabatic invariants of charged-particle motion, extensive work was done on the application of Kruskal's asymptotic theory of nearly-periodic Hamiltonian systems[1] to study the magnetic moment series for a charged particle in a general electromagnetic field. The objective was to examine in detail a few terms of the asymptotic series which represent the transformation functions of the theory, with a view to finding general features that could be exploited analytically. This was indeed possible in a special case that can be reduced to the problem of a time-dependent harmonic oscillator.[2,3] In that case, the result was a generalization in closed form of the adiabatic invariant series whose lowest-order term is energy divided by frequency. This series, written in terms of the charged-particle variables, is related to, but not the same as, the magnetic moment series. It has not been possible to obtain similar general results with the magnetic moment series for a charged particle moving in a more general electromagnetic field. If results of this sort are possible, then it is probably more appropriate to seek them by attempting to generalize the time-dependent harmonic oscillator results.

In order to facilitate performing the very tedious manipulations that are involved in applying Kruskal's theory to the motion of a charged particle in a general electromagnetic field, the problem was formulated in a way that allows use of some novel techniques with the IBM FORMAC computing system to do much of the algebra. The formulation of the problem and the techniques used will be described in coming publications.

References

1. M. Kruskal, J. Math. Phys. 3, 806 (1962).
2. H. R. Lewis, Jr., Phys. Rev. Letters 18, 510 (1967); erratum in ibid., 18, 636 (1967).
3. H.R. Lewis, Jr., "A Class of Exact Invariants for Classical and Quantum Time-Dependent Harmonic Oscillators," To be published.

PLASMA SIMULATION

(R. L. Morse)

During this last year some encouraging results have been obtained for numerical simulation of plasma. Two very different sets of computations have helped in an understanding of experiments.

The first is a two-dimensional cylindrical simulation of the plasma in a coaxial discharge, with static initial filling. Corresponding experiments are described in this report by I. Henins and J. Marshall (p. 37). The plasma is treated as a classical compressible fluid, for the reason that ion-ion mean free paths in the plasmas of interest are short compared to other characteristic lengths. The related collision processes include ion-neutral elastic and charge exchange collisions in addition to ion-ion Coulomb collisions. The magnetic field, which is azimuthal as in a z-pinch, is assumed not to penetrate the plasma. The field serves only as a piston of zero inertia. The theoretical arguments for this assumption are uncertain, and the justification comes from the over-all success of the model and direct measurement of the degree of field penetration. Two theoretical treatments have proceeded from this model. One, which is not simulation, is an analytic equilibrium treatment describing a solution of the various mass, momentum, and energy equations in an infinitely long device (no end to the center electrode) in which a constant current flows. This solution is stationary in a frame moving axially with the plasma sheath or shock. It is helpful in understanding the problem but is really only preparation for the much more effective simulation work.

Time-dependent solutions have been obtained for this model, including a center electrode with the same shape as in the experiment. The computing method used is the Particle In Cell (P.I.C.) method developed by T Division at LASL. (The actual computing work on this part of the problem has been done by D. Butler and T. Amsden of T Division). The computations agree with the experimental data to within about 10%. Deviations

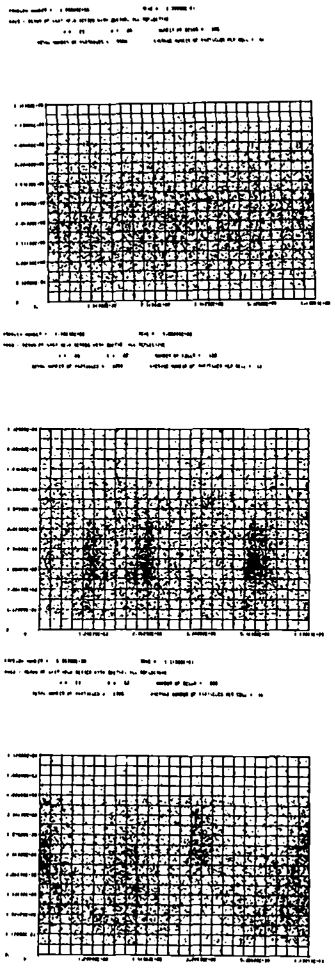

Fig. 107. Particle plots (radius vs axial dimension) from mirror instability calculations, after 0, 1, and 2 gyro-periods, respectively.

at this point are thought to result from incomplete specification of both the external circuit and the equation of state of deuterium. These shortcomings are being corrected. The agreement mentioned above extends to the structure of the shocked layer, which runs ahead of the magnetic piston, as well as to the gross shape of the layer. The experimental simulation agreement holds through the time when the discharge reaches the end of the center electrode, implodes on to the axis, and forms the Marshall gun bubble. A short, preliminary description of this work appears in the proceedings of the LASL Conference on Pulsed High Density-Plasma (LA-3770) and a more complete paper is in preparation.

The second simulation effort is just getting started. It treats plasma which approximately obeys the Vlasov equations. The code which has operated successfully simulates a plasma and field system that is cylindrically symmetric. Including the three dimensional particle velocity distribution, the system has a total of five dimensions plus time. The computing method is a version of P.I.C. in which fields, which determine the particle motion, are computed self-consistently starting from the instantaneous particle distribution. The most definitive results from this code to date have come from studying mirror instabilities in a diffuse θ-pinch-like plasma. The initial equilibrium has a much greater plasma pressure perpendicular to the magnetic field than parallel, such as would result from conventional θ-pinch compression. This velocity space anisotropy causes a high-β plasma to be unstable to m = 0 (rotationally symmetric) mirror instabilities. The computations show that as these modes grow to a large amplitude they tend to equalize perpendicular and parallel plasma pressures, on a time scale of a few ion gyro-periods. This is a very short time and appears to explain an old experimental observation--that rapid end loss from θ-pinches begins long before collisional equipartition could cause sufficiently large axial thermal motions of ions. Figure 107 shows a set of three particle plots taken from such a mirror instability run. Radius is plotted vertically and the axial dimension horizontally with the center axis at the bottom.

The initial conditions are a diffuse, high-β equilibrium in which B is entirely axial and all particle velocities are radial. The spatial particle plot of the initial distribution is the first frame; it should be noted that the apparent density must be divided by radius to give the real density. The second and third frames show the plasma at ~ 1 and 2 gyro-periods after the initial time. The bunching of particles reflects the unstable growth of the mirror modes. At the time of the third frame the axial pressure has reached a significant fraction of the radial pressure and the plasma has begun to relax to a fine, stable z-independent state in which the spatial distribution resembles the initial state. Other similar codes are now being written to treat other geometries and variations on the model.

PUBLICATIONS

J. W. Mather and A. H. Williams, "Image Converter Observations of the Development of the Dense Plasma Focus Discharge," Phys. Fluids, 9, 2081 (1966).

R. L. Morse, "End Losses from a Linear θ-Pinch," ibid., 9, 2536 (1966).

R. L. Morse, "Bounce Model Pinch Instability," ibid., 10, 1017 (1967).

M. Daehler and F. L. Ribe, "Cooperative Light Scattering from Theta-Pinch Plasmas," Phys. Letters, 24A, 745 (1967).

M. Daehler, G. A. Sawyer, E. L. Zimmerman, "Mode Controls in a Ruby Laser," J. Appl. Phys., 38, 1980 (1967).

F. C. Jahoda, R. A. Jeffries, G. A. Sawyer, "Fractional-Fringe Holographic Plasma Interferometry," Appl. Opt., 6, 1407 (1967).

G. P. Boicourt, M. J. Hollen, E. L. Kemp, "Comparative Evaluation of Size-A Metal Anode Ignitrons," Proc. Symp. on Engineering Problems of Controlled Thermonuclear Research, Gatlinburg, Tenn., Oct. 1966. Oak Ridge Nat. Lab., 1967, p. 8.

G. P. Boicourt, "Evaluation of Coaxial Cable Performance at High Voltages: An Interim Report," ibid., ORNL, 1967, p. 13.

E. L. Kemp, "Engineering Aspects of the Scyllac Proposal," ibid., ORNL 1967, p. 179.

H. Dreicer, "Line Shape Measurements on Electron Cyclotron Harmonics Emitted by a Laboratory Plasma," Proc.7th Intern. Conf. on Phenomena in Ionized Gases, Belgrade, Aug. 1965. Prosveta, 1966, Vol. 2, p. 491.

N. J. Peacock, R. D. Cowan, G. A. Sawyer, "Theta-Pinch Sources of Vacuum Ultraviolet Radiation," ibid., Prosveta, 1966, Vol. 2, p. 599.

H. Dreicer, W. B. Riesenfeld ,"On the Theory of Velocity Distributions Associated with Bounded Quiescent Plasmas," Proc. Conf. on the Physics of Quiescent Plasmas, Frascati, Italy, Jan. 1967. Laboratori Gas Ionizatti, 1967, Pt. 1, p. 89.

M. Daehler, F. L. Ribe, "Cooperative Light Scattering from Theta-Pinch Plasmas," Bull. Am. Phys. Soc., Ser. 2, 12, 680 (1967)(Abstract).

M. Daehler, F. L. Ribe, "High-Resolution, Coherent, Light-Scattering Experiment," ibid., Ser. 2, 12, 743 (1967)(Abstract).

W. Grossmann, Jr., R. L. Morse, "Computation of Particle Losses from Cusped and θ-Pinch Devices," ibid., Ser. 2, 12, 758 (1967)(Abstract).

H. J. Karr, L. C. Burkhardt, J. N. DiMarco, "Plasma Confinement in a Caulked Stuffed Cusp Device," ibid., Ser. 2, 12, 758 (1967)(Abstract).

H. Dreicer, "Radiative Recombination Induced by Intense Laser Light," ibid., Ser. 2, 12, 761 (1967)(Abstract).

J.A. Phillips, A. E. Schofield, "Reflection of a Hydromagnetic Shock in Coaxial Geometry," ibid., Ser. 2, 12, 775 (1967)(Abstract).

R. L. Morse, "Adiabatic Time Development of Linear θ-Pinch Plasma Profiles," ibid., Ser. 2, 12, 787 (1967)(Abstract).

G. A. Sawyer, V. A. Finlayson, F. C. Jahoda, K. S. Thomas, "Comparison of β n, T_i in High and Low Pressure θ-Pinch Operation," ibid., Ser. 2, 12, 787 (1967)(Abstract).

D. B. Thomson, R. S. Caird, F.A. Finlayson, M. Fowler, W. B. Garn, R. W. Kewish, Jr., J. L. Tuck, "Characteristics of the Scyllacita θ-Pinch," ibid., Ser. 2, 12, 788 (1967)(Abstract).

D. J. Rode, J. E. Hammel, "Laser Interferometry on Large, Low-Density Plasma Experiments, " ibid., Ser. 2, 12, 793 (1967) (Abstract).

F. C. Jahoda, R. A. Jeffries, "Holographic Plasma Interferometry," ibid., Ser . 2, 12, 793 (1967) (Abstract).

J. E. Hammel, R. M. Henson, "Studies of a Linear Magnetic Dipole Shield Immersed in a Fast Plasma Stream," ibid., Ser. 2, 12, 799 (1967)(Abstract).

J. L. Shohet, J. Marshall, Jr., "Model of Inverse Pinch Gun," ibid., Ser. 2 , 12, 801 (1967) (Abstract).

J. Marshall, Jr., I. Henins, J. M. Lohr, "Inverse Pinch Pulsed Plasma Gun," ibid., Ser. 2, 12, 801 (1967)(Abstract).

D. A. Baker, J.E. Hammel, L. W. Mann, "Design Study of a Quadrupole Device Whose Inner Current Conductors are Fed Through Magnetically Shielded Supports," ibid., Ser. 2, 12, 909 (1967)(Abstract).

A.S. Rawcliffe, F.L. Ribe, G. A. Sawyer, "Proposed Scyllac Computer System for Data Acquisition and Treatment," LA-3713.

F. L. Ribe, Compiler, "Proceedings of APS Topical Conference on Pulsed High-Density Plasmas, Los Alamos, Sep. 1967," LA-3770.

J. A. Phillips, A. E. Schofield, "High Q Power Capacitor," U.S. Patent 3,275,916 (1966).

R. S. Dike, E.L. Kemp, "Low Inductance Capacitor and Switching Assembly," U.S. Patent 3,293,488 (1966).

I. Henins, J. Marshall, Jr., "Thermal Expansion Impulse Actuator in Plasma Jet Apparatus," U.S. Patent 3,281,324 (1966).

J. A. Phillips, J.W. Mather, "Plasma Accelerator Having Rapidly Pulsed Coil for Expelling Plasma," U.S. Patent 3,321,664 (1967).

Addendum to LA-3831-MS

(Status Report of the LASL Controlled Thermonuclear Research Program
for 12-month Period Ending Oct. 31, 1967.)

March 1968

HAMILTON'S PRINCIPLE AND NUMERICAL SOLUTION OF THE VLASOV EQUATIONS

(H. R. Lewis)

The Vlasov system of integro-partial differential equations, expressed in terms of Lagrangian variables for the particles and Eulerian variables for the electromagnetic field, can be derived from Hamilton's principle by using the Lagrangian that was given by Low[1] and by Sturrock.[2] That Lagrangian can be generalized to include systems in which there are present any of a large class of material media that exhibit nonlinear polarizability and magnetizability, and also to include forces of nonelectromagnetic character. These possibilities allow convenient imposition of certain kinds of particle and field boundary conditions for finite systems. Not only can the exact equations of motion for these systems be derived from Hamilton's principle, it can also be used to derive approximations to the exact equations of motion. The approximate system of equations to be emphasized here is a system of ordinary differential equations in time, although the basic method can be used to derive other approximate systems of equations--i.e., a system of difference equations. The method can be applied to any Lagrangian system.

The first step in solving equations approximately by any method is to choose the form in which the desired functions are to be represented. A common way of representing a function of continuous variables approximately is to specify the function on a mesh, i.e., to specify the function at each of a set of discrete values of the arguments. Another method of representation frequently used is to approximate the function by a linear combination of a finite number of linearly independent basis functions. The type of representation chosen is really a combination of these two, because the differential equations in time that are derived must generally be solved numerically, whereas the dependences of the unknown functions on other variables will be represented by linear combinations of linearly independent basis functions. Let $g(x,t)$ be one of the functions to be represented, where t is time and x denotes the remaining arguments of g. For each particular value of t, $g(x,t)$ may be approximated by a linear combination of a finite number of linearly independent basis functions, say $\psi_i(x)$. The coefficients in the expansion are functions of t only, so that the representation of $g(x,t)$ is

$$g(x,t) = \sum_{i=1}^{N} a_i(t)\psi_i(x). \tag{1}$$

Suppose that all the unknown functions are approximated in this fashion; the problem then is to derive equations that determine the time evolution of the time-dependent coefficients and to solve those equations. The differential euqations that are chosen to determine the time evolution of the coefficients will clearly be ordinary differential equations, and, from the standpoint of numerical analysis, that in itself may be a distinct advantage over having to work with a system of integro-partial differential equations. By choosing the basis functions appropriately, the system of ordinary differential equations can be put into a form for which there are standard finite-difference methods of numerical solution whose properties are relatively well understood. At least one such method is formulated in a way that guarantees numerical stability.[3,4]

The mere fact of requiring that the unknown functions be approximated in the way illustrated by Eq. (1) does not specify the differential equations that determine the time evolution of the coefficients. In fact, there are infinitely many systems of equations for the coefficients that can be derived from the exact integro-differential equations. The solutions of these different systems of equations will differ in the fidelity with which they represent the time evolution of the unknown functions, and it is desirable to have a criterion for choosing one of the infinitely many systems. The method proposed for choosing a system is to substitute the approximate representations of the unknown functions into the Lagrangian density and then to determine the system of differential equations for the time-dependent coefficients by applying Hamilton's principle. The only difference between this procedure and using Hamilton's principle to derive the exact equations is that the functional variations are restricted to be within the class of functions chosen for approximating the unknown functions. In some useful sense, the system of equations so derived should approximate the exact equations as well as is possible.

It may be hoped that this procedure based on Hamilton's principle will prove particularly advantageous for nonlinear systems, such as the Vlasov system, and that some useful properties of the approximate system of equations can be derived. Details of the method are described in a LASL Report.[5]

References

1. F. E. Low, "A Lagrangian Formulation of the Boltzmann-Vlasov Equations for Plasmas," Proc. Roy. Soc. (London) A248, 282 (1958).
2. P. A. Sturrock, "A Variational Principle and an Energy Theorem for Small-Amplitude Disturbances of Electron Beams and of Electron-Ion Plasmas," Ann. Phys. (N.Y.) 4, 306 (1958).
3. H. R. Lewis, Jr. and E. J. Stovall, Jr., "Comments on a Floating-Point Version of Nordsieck's Scheme for the Numerical Integration of Differential Equations," Math. Comp. 21, 157 (1967).
4. H. R. Lewis, Jr. and E. J. Stovall, Jr., "A FORTRAN Version of Nordsieck's Scheme for the Numerical Integration of Differential Equations," LA-3292 (March 1965).
5. H. R. Lewis, Jr., "Hamilton's Principle and Numerical Solution of the Vlasov Equations," LA-3803

THE MOTION OF A TIME-DEPENDENT HARMONIC OSCILLATOR, AND THE MOTION OF A CHARGED PARTICLE IN A CLASS OF TIME-DEPENDENT, AXIALLY SYMMETRIC ELECTROMAGNETIC FIELDS

(H. R. Lewis)

The exact invariant described for a time-dependent harmonic oscillator[1,2] can be used to derive an elegant representation of the general solution of the equations of motion for the oscillator. This solution can be used to obtain the general solution of the equations of motion for a charged particle in certain electromagnetic fields.

The equations of motion for a time-dependent harmonic oscillator are equivalent to those for a particle moving in a certain type of electromagnetic field which is a superposition of two components. One component is a time-dependent, axially symmetric, uniform magnetic field and the associated induced electric field that corresponds to zero charge density. The other component is the radial electric field produced by a time-dependent, axially symmetric, uniform charge distribution. Because of the equivalence of the equations of motion, the representation of the general solution of the oscillator problem can be transcribed into a corresponding representation of the general solution of the particle problem.

Time-Dependent Harmonic Oscillator

A time-dependent harmonic oscillator is defined as a system described by the equation

$$\epsilon^2\ddot{q} + \Omega^2(t)q = 0, \qquad (1)$$

where time differentiation is denoted by a dot, and where $\Omega(t)$ is an arbitrary piecewise continuous function of time. It has been shown[1,2] that the function

$$I = \frac{1}{2}\left[\rho^{-2}q^2 + \epsilon^2(\rho\dot{q} - q\dot{\rho})^2\right] \qquad (2)$$

is an exact invariant of Eq. (1) as long as $\rho(t)$ is any particular solution of

$$\epsilon^2\ddot{\rho} + \Omega^2(t)\rho - \rho^{-3} = 0. \qquad (3)$$

The quantities q and Ω may be complex.

Equations (1) and (2) can be simplified significantly by replacing the variables q and t by variables Q and τ defined by

$$Q = \frac{q}{\rho},\ \tau = \frac{1}{\epsilon} \int^{t} \rho^{-2} (t')dt'. \qquad (4)$$

It is easily verified that the expression for I in terms of Q and τ is

$$I = \frac{1}{2} [Q^2 + (\frac{dQ}{d\tau})^2]. \qquad (2')$$

The differential equation for Q as a function of τ corresponding to Eq. (1) is

$$\frac{d^2Q}{d\tau^2} + Q = 0. \qquad (5)$$

The general solution of Eq. (5) is

$$Q = Ae^{i\tau} + Be^{-i\tau}, \qquad (6)$$

where A and B are arbitrary complex constants, and I, A, and B are related by

$$I = 2AB.$$

Therefore, the general solution of Eq. (5) can be written as

$$Q = \sqrt{\frac{1}{2} I}\ [\sigma e^{i(\tau-\tau_o)} + \frac{1}{\sigma} e^{-i(\tau-\tau_o)}], \qquad (7)$$

where $\sigma e^{i\tau_o} = \sqrt{A/B}$, and σ and τ_o are arbitrary real constants. Equation (7) is an elegant representation of the general solution of Eq. (1). There is one representation for each ρ that satisfies Eq. (3).

Charged Particle

Consider a particle of mass m and charge e moving in an electromagnetic field defined by the potentials

$$\left.\begin{aligned} \varphi &= \frac{1}{2} \frac{e}{mc^2} \eta(t) r^2 = \frac{1}{2} \frac{e}{mc^2} \eta(t)\ (x^2 + y^2) \\ &\text{and} \\ \underline{A} &= \frac{1}{2} B(t)\ \hat{k} \times \underline{r}, \end{aligned}\right\} \qquad (8)$$

where $\underline{r}$ is the position vector, $\hat{k}$ is a unit vector along the symmetry axis, $\underline{r}$ is distance from the symmetry axis, x and y are cartesian coordinates perpendicular to the symmetry axis, and η(t) and B(t) are arbitrary piecewise continuous functions. The electric and magnetic fields are

$$\underline{E} = - \nabla\varphi - \frac{1}{c} \dot{\underline{A}}$$

$$= - \frac{e}{mc^2} \eta(t)\ (x\hat{i} + y\hat{j}) - \frac{1}{2c} \dot{B}(t)\ \hat{k} \times \underline{r}$$

$$\underline{B} = \nabla \times \underline{A}$$

$$= B(t)\hat{k},$$

where $\hat{i}$ and $\hat{j}$ are unit vectors along the positive x and y directions, respectively. The equations of motion for the particle are

$$\left.\begin{aligned} \epsilon\ddot{x} &= - \frac{1}{\epsilon} \eta(t)x + \frac{1}{2} \dot{B}(t)y + B(t)\dot{y} \\ e\ddot{y} &= - \frac{1}{\epsilon} \eta(t)y - \frac{1}{2} \dot{B}(t)x - B(t)\dot{x}, \end{aligned}\right\} \qquad (9)$$

where

$$\epsilon = \frac{mc}{e} .$$

The equations of motion can be written simply in terms of a complex variable, q, defined by

$$re^{i\theta} = x + iy = q\ e^{- \frac{i}{2\epsilon} \int^{t} B(t')dt'} . \qquad (10)$$

The quantities r and θ are the usual cylindrical coordinates of the particle. The equation satisfied by q is

$$\left.\begin{aligned} &\epsilon^2\ddot{q} + \Omega^2 (t)q = 0, \\ &\text{where} \\ &\Omega^2 (t) = \frac{1}{4} B^2 (t) + \eta(t) \end{aligned}\right\} . \qquad (11)$$

The function $\Omega^2(t)$ may be negative.

Since Eq. (11) is that of a time-dependent harmonic oscillator, we can now combine Eqs. (7) and (10) to obtain expressions for r and θ as functions of t. The result is

$$\left.\begin{aligned} &R = \frac{r}{\rho} = |Q| \\ &\text{and} \\ &\theta = \arg Q - \frac{1}{2\epsilon} \int^{t} B(t')dt', \end{aligned}\right\} \qquad (12)$$

where ρ is <u>any</u> solution of Eq. (3), τ is defined by Eq. (4), and where

$$
\begin{aligned}
Q &= \sqrt{\tfrac{1}{2} I}\left[\sigma e^{\,i(\tau-\tau_o)} + \frac{1}{\sigma} e^{-\,i(\tau-\tau_o)}\right] \\
|Q|^2 &= \frac{1}{2}\,|I|\,\frac{(\sigma^2+1)^2}{\sigma^2}\left[\cos^2(\tau-\tau_o) + \left(\frac{\sigma^2-1}{\sigma^2+1}\right)^2 \sin^2(\tau-\tau_o)\right] \\
\arg Q &= \tan^{-1}\left[\left(\frac{\sigma^2-1}{\sigma^2+1}\right)\tan(\tau-\tau_o)\right] - \frac{1}{2}\arg I \\
I &= \frac{1}{2} e^{2i\left[\theta + \frac{1}{2\epsilon}\int^t B(t')dt'\right]}\left\{\left[R^2 + \left(\frac{dR}{d\tau}\right)^2 - \left(\epsilon\frac{p_\theta}{m}\right)^2\frac{1}{R^2}\right]\right. \\
&\qquad \left. + 2i\epsilon\,\frac{p_\theta}{m}\,\frac{1}{R}\,\frac{dR}{d\tau}\right\} \\
|2I|^2 &= \left[R^2 + \left(\frac{dR}{d\tau}\right)^2 - \left(\epsilon\frac{p_\theta}{m}\right)^2\frac{1}{R^2}\right]^2 + 4\epsilon^2\left(\frac{p_\theta}{m}\right)^2\frac{1}{R^2}\left(\frac{dR}{d\tau}\right)^2 \qquad (13) \\
\arg I &= 2\left[\theta + \frac{1}{2\epsilon}\int^t B(t')dt'\right] \\
&\qquad + \tan^{-1}\left\{\frac{2\epsilon\,\frac{p_\theta}{m}\,\frac{1}{R}\,\frac{dR}{d\tau}}{R^2 + \left(\frac{dR}{d\tau}\right)^2 - \left(\epsilon\frac{p_\theta}{m}\right)^2\frac{1}{R^2}}\right\} \\
\frac{1}{m}p_\theta &= r^2\left[\dot{\theta} + \frac{1}{2\epsilon}B(t)\right] \\
\sigma &= 2^{-\frac{1}{2}}\left\{\frac{2\epsilon}{m}\,\frac{p_\theta}{|I|} + \sqrt{\left(\frac{2\epsilon}{m}\,\frac{p_\theta}{|I|}\right)^2 + 4}\right\}^{\frac{1}{2}} .
\end{aligned}
$$

References

1. H. R. Lewis, Jr., Phys. Rev. Letters 18, 510 (1967); erratum: ibid., 18, 636 (1967).

2. H. R. Lewis, Jr., "A Class of Exact Invariants for Classical and Quantum Time-Dependent Harmonic Oscillators," Preprint No. LA-DC-9020, to be published.

PUBLICATIONS

H. R. Lewis, Jr., "An Invariant for the Oscillator with a Time-Dependent Frequency," Bull. Am. Phys. Soc. 12, 778 (1967) (Abstract).

H. R. Lewis, Jr., "Classical and Quantum Systems with Time-Dependent Harmonic-Oscillator-Type Hamiltonians," Phys. Rev. Letters 18, 510 (1967), erratum: ibid., 18 636 (1967).

H. R. Lewis, Jr., and E. J. Stovall, Jr., "Comments on a Floating-Point Version of Nordsieck's Scheme for the Numerical Integration of Differential Equations," Math. Comp. 21, 157 (1967).

R. L. Morse, "Ballooning of $\beta = 1$ Plasmas with Sharp Boundaries," Physics of Fluids, 10, 236 (1967).

Butler, Thomas Daniel, Henins, Ivars, Marshall, John, Jr., Morse, Richard L., "Coaxial Snowplow Discharge," Proc. APS Topical Conf. on Pulsed High-Density Plasmas, Los Alamos Sci. Lab., N.M., Sept. 1967. LA-3770, Paper C7.

Freidberg, Jeffrey L., Morse, Richard L., "Z-Dependent Marginal Stability of the Rigid Rotor Model of a High-Theta Pinch," ibid., LA-3770, Paper B7.

Gribble, Robert F., Little, Edward M., Quinn, Warren E., "Faraday Rotation Measurements on the Scylla IV Theta Pinch," ibid., LA-3770, Paper A3.

Henins, Ivars, Henry, Paul S., Lohr, John M., Marshall, John, Jr., "Coaxial Gun Development," ibid., LA-3770, Paper E2.

Johnson, John L., Morse, Richard L., Riesenfeld, Werner B., "Hydromagnetic Equilibrium of a Finite Beta Toroidal Plasma Column," ibid., LA-3770, Paper B2.

Kemp, Edwin L., Jr., Quinn, Warren E., Ribe, Fred L., Sawyer, George A., "15-Meter Scyllac Theta Pinch," ibid., LA-3770, Paper G1.

Mather, Joseph W., Bottoms, Paul J., Williams, Arthur H., "Some Characteristics of the Dense Plasma Focus," ibid., LA-3770, Paper C-1.

Morse, Richard L., "Sheath Stability," ibid., LA-3770, Paper F3.

Oliphant, Thomas A., Jr., "Computer Simulation of the Theta Pinch," ibid., LA-3770, Paper F2.

Phillips, James A., Schofield, Aldred E., Tuck, James L., "Columba - A High Temperature Z-Pinch Experiment," ibid., LA-3770, Paper G3.

Thomas, Keith S., "Measurement of Theta-Pinch End Loss Using a Gas Laser Interferometer," ibid., LA-3770, Paper D3.

Thomson, David B., Caird, Robert S., Jr., Ewing, Kenneth J., Fowler, Clarence M., Garn, Wray B., Crawford, John Clark, Damerow, Richard Aasen, "Explosive Generator-Powered Theta-Pinch," ibid., LA-3770, Paper H3.

Abstracts of the papers in the Proceedings of the APS Topical Conference on Pulsed High-Density Plasmas, published in LA-3770, will be found in the Bull. Amer. Phys. Soc., Series 2, 12, p. 1153 et. seq. (1967).